

Faculdade de Engenharia da Universidade do Porto



Biomechanical Simulation of Chromosomes

Vítor Daniel Pereira Sá

Dissertation submitted to Faculty of Engineering of the University of Porto to
obtain the degree of Master in Bioengineering

Supervisor: Professor Jorge Américo Oliveira Pinto Belinha, PhD
Co-Supervisor: Professor Renato Manuel Natal Jorge, PhD

July 2017

© Vítor Daniel Pereira Sá, 2017

Abstract

Several statistical studies [1] demonstrate the increasing number of new cases of cancer worldwide and despite recent advances in diagnostic and therapeutic methods the mortality rate has no tendency to decrease. Regardless of the enormous investments made in the area of oncology, the obtained results do not correspond to current expectations and needs. In this way, it is imperative to break with the traditional approach to the problem and seek alternative solutions.

The appearance of tumor masses is associated with the occurrence of gene mutations in the DNA that is contained in the chromosomes. These alterations in the genetic sequence can induce modifications in chromosomes structure and consequently on their mechanical properties. We can find these microstructures within the nucleus of all the cells that form the body of the living organism. Nowadays, it is quite easy to observe and study chromosomes with light, fluorescence or even electron microscopy and their shape and geometry can be obtained without difficulty.

The objective of this work is to analyze in *silico* the biomechanical behavior of human chromosomes at the microscale level and to understand how they react to static and dynamic requests. Thus, the development of new mechanical techniques capable of stimulating the decay of these microscopic structures is proposed, which may be very useful for the development of diagnostic and/or even treatment methods.

In order to simulate the biomechanical behavior of the chromosomes, the Finite Element Method (FEM) was used as well as meshless methods. Chromosomes were treated as a linear isotropic elastic material in all performed simulations and their mechanical properties were obtained from the literature.

In this work, an elasto-static and free vibration study is carried out, which aims to validate the applicability of this type of methodology to microscopic structures using two-dimensional (2D) and three-dimensional (3D) artificial models of a chromosome. Later, a study of free vibrations of 2D and 3D models of three different human chromosomes was carried out.

The results show that it is possible to identify chromosomes through their natural vibration modes and, on the other hand, that the meshless methods, when compared to the Finite Element Method (FEM), allow the production of more precise and smooth variable fields.

Resumo

Vários estudos estatísticos [1] demonstram o crescente número de novos casos de cancro em todo o mundo e, apesar dos recentes avanços dos métodos de diagnóstico e terapêutica, a taxa de mortalidade não tem tendência para diminuir. Apesar dos enormes investimentos que têm sido realizados na área da oncologia, os resultados obtidos não correspondem às expectativas e às necessidades atuais. Desta forma é imperativo romper com a abordagem tradicional ao problema e procurar soluções alternativas.

O aparecimento de massas tumorais está associado à ocorrência de mutações génicas no ADN que está contido nos cromossomas. Estas alterações na sequência genética podem induzir alterações estruturais dos cromossomas e consequentemente também das suas propriedades mecânicas. Estas microestruturas podem ser encontradas dentro do núcleo de todas as células que formam o corpo do organismo vivo. Hoje, é possível observar e estudar facilmente os cromossomas com microscopia de luz, fluorescência ou mesmo através de microscopia eletrónica e a sua forma e geometria pode ser obtida sem dificuldade.

Este trabalho tem como objetivo analisar *in silico* o comportamento biomecânico de cromossomos humanos ao nível da sua microescala, permitindo compreender como estes reagem a solicitações estáticas e dinâmicas. Assim, propõem-se o desenvolvimento de novas técnicas mecânicas capazes de estimular o decaimento dessas estruturas microscópicas, o que poderá ser muito útil para o desenvolvimento de métodos de diagnóstico e/ou mesmo de tratamento.

Para simular o comportamento biomecânico dos cromossomas, utilizou-se o Método dos Elementos Finitos (FEM), bem como métodos sem malha. Os cromossomas foram tratados como um material elástico linear isotrópico em todas as simulações realizadas e as suas propriedades mecânicas foram baseadas na literatura.

Neste trabalho, é realizado um estudo elasto-estático e também de vibrações livres, com o objetivo de validar a aplicabilidade deste tipo de metodologia a estruturas microscópicas utilizando modelos artificiais bidimensionais (2D) e tridimensionais (3D) de um cromossoma. Posteriormente, foi realizado um estudo das vibrações livres dos modelos 2D e 3D de três cromossomas humanos diferentes.

Os resultados mostram que é possível identificar cromossomas através dos seus modos de vibração natural e, por outro lado, que os métodos sem malha, quando comparados com o Método de Elementos Finitos (FEM), permitem a produção de campos de variáveis mais precisos e mais suaves.

Agradecimentos

Estes 5 anos de percurso académico foram férteis em desafios, que teriam sido impossíveis de transformar em conquistas e sonhos realizados sem a ajuda de todos os meus colegas de curso, ex-alunos e orientação de professores e técnicos.

Agradeço ao meu orientador, o Professor Jorge Belinha, por todo o acompanhamento, orientação e dedicação constante a este projeto, ajuda indispensável para que cada passo do trabalho fosse dado rumo à meta e para que fossem alcançados todos objetivos. Gostava também de agradecer ao meu coorientador, o Professor Renato Natal, pela sua disponibilidade e acompanhamento.

Um muito obrigado ao Grupo de Jovens de Santiago de Carapeços - *Kyrios*, por todos os momentos de descontração que me proporcionaram, pela irreverência e espírito de aventura e de luta que caracterizam este grupo. Obrigado por me transmitirem uma cultura de resiliência, de não desistir perante as dificuldades e sobretudo pelos sorrisos rasgados que contagiam qualquer um.

Agradeço também a todos os meus colegas e amigos voluntários da Cruz Vermelha Portuguesa da Delegação de Campo, por manterem vivos os 7 princípios fundamentais do movimento internacional da Cruz Vermelha e do Crescente Vermelho, por manterem acesa em mim a vontade do serviço à comunidade.

Por último faço um agradecimento especial à minha família, mãe, pai e irmã, pelo suporte financeiro, mas sobretudo pelo suporte emocional e por todos os conselhos que de deram ao longo destes anos. Obrigado à minha madrinha e aos meus avós maternos pelo exemplo de humildade, trabalho, dedicação e lealdade, simplesmente um obrigado pelo exemplo de vida e humanidade.

Vítor Daniel Pereira Sá

Institutional Acknowledgments

The author truly acknowledges the work conditions provided by the Applied Mechanics Division (SMAp) of the department of mechanical engineering (DEMec) of FEUP and by the inter-institutional project “BoneSys - Bone biochemical and biomechanic integrated modeling: addressing remodeling, disease and therapy dynamics” funded by the “Laboratório Associado de Energia Transportes e Aeronáutica” (UID/EMS/50022/2013) and by the project NORTE-01-0145-FEDER-000022 - SciTech - Science and Technology for Competitive and Sustainable Industries, co-financed by Programa Operacional Regional do Norte (NORTE2020), through Fundo Europeu de Desenvolvimento Regional (FEDER).

“The time to take counsel of your fears is before you make an important battle decision.

That’s the time to listen to every fear you can imagine!

When you have collected all the facts and fears and made your decision,

turn off all your fears and go ahead!”

*George S. Patton
WWII Soldier
(1885-1945)*

Contents

| | |
|--|-------------|
| List of Figures | xv |
| List of Tables | xvii |
| Abbreviations | xxi |
| Chapter 1 | 1 |
| Introduction | 1 |
| 1.1 - Motivation | 2 |
| 1.2 - Objectives | 2 |
| 1.3 - Document Structure | 3 |
| Chapter 2 | 5 |
| Chromosomes | 5 |
| 2.1 - Anatomical Overview | 7 |
| 2.1.1 - The Structure of DNA | 7 |
| 2.1.2 - Human Karyotype | 10 |
| 2.2 - Mechanical Properties | 12 |
| Chapter 3 | 15 |
| Numerical Methods | 15 |
| 3.1 - FEM | 15 |
| 3.2 - Meshless Methods | 16 |
| 3.2.1 - Meshless Generic Procedure | 17 |
| 3.2.2 - Nodal Connectivity | 18 |
| 3.2.2.1 - RPIM | 18 |
| 3.2.2.2 - NNRPIM | 19 |
| 3.2.3 - Numerical Integration | 20 |
| 3.2.3.1 - RPIM | 20 |
| 3.2.3.2 - NNRPIM | 23 |
| 3.2.4 - Interpolation Functions | 23 |
| Chapter 4 | 27 |
| Solid mechanics | 27 |
| 4.1 - Fundamentals | 27 |
| 4.2 - Weak Form | 29 |
| 4.2.1 - Galerkin Weak Form | 29 |
| 4.3 - Discrete Equation System | 31 |
| 4.3.1 - Dynamic Equations | 33 |
| 4.3.2 - Results Parameterization | 35 |
| Chapter 5 | 37 |

| | |
|---|------------|
| The Modelling Process | 37 |
| 5.1 - Geometry..... | 37 |
| 5.2 - Mesh Definition..... | 40 |
| 5.3 - Finite Element Meshless Method Analysis Software - FEMAS..... | 40 |
| Chapter 6..... | 43 |
| Preliminary Studies..... | 43 |
| 6.1 - Model | 43 |
| 6.2 - Nodal Discretization Convergence Study | 44 |
| 6.2.1 - Stress-strain experiment simulation..... | 45 |
| 6.2.2 - Free-Vibrations | 51 |
| 6.2.3 - Bending Test..... | 62 |
| 6.3 - 2D Shell-Like Convergence Study | 63 |
| 6.3.1 - Stress-strain experiment simulation..... | 65 |
| 6.3.2 - Free-Vibrations | 69 |
| 6.3.3 - Bending Test..... | 80 |
| 6.4 - 3D Model..... | 82 |
| 6.4.1 - Stress-strain..... | 82 |
| 6.4.2 - Free-Vibrations | 85 |
| 6.4.3 - Bending Test..... | 95 |
| Chapter 7..... | 97 |
| Human Chromosomes | 97 |
| Chapter 8..... | 119 |
| Conclusions and Future Work | 119 |
| Bibliography | 121 |

List of Figures

| | |
|--|----|
| Figure 2.1 - Model for the packing of chromatin and the chromosome scaffold in metaphase chromosomes [22]. | 6 |
| Figure 2.2 - DNA chemical structure. [23]. | 8 |
| Figure 2.3 - Schematic representation of the DNA double helix. [23]. | 9 |
| Figure 2.4 - Human karyotype drawn from chromosomes' average measurement values. [39]. | 10 |
| Figure 2.5 - Types of chromosome-attachments and their results during the somatic mitoses. The spindle-fiber attachments indicated by fine lines [40]. | 11 |
| Figure 2.6 - Human chromosome stretching experiment and Young modulus calculation. [42]. | 12 |
| Figure 3.1 - Example of a mesh discretized for the FEM: (a) original, and (b) obtained mesh after discretization. | 16 |
| Figure 3.2 - Nodal discretization of the problem domain: (a) Solid domain; (b) Regular nodal discretization; (c) Irregular nodal discretization. [74]. | 18 |
| Figure 3.3 - Examples of different types of influence-domains: (a) fixed rectangular shaped influence-domain, (b) fixed circular shaped influence-domain and (c) flexible circular shaped influence-domain. [74]. | 19 |
| Figure 3.4 - (a) First degree influence-cell. (b) Second degree influence-cell. (c) Representation of the sub-cells forming the Voronoï cell and schematic representation of 4×4 integration points inside a sub-cell. [87]. | 20 |
| Figure 3.5 - a) Triangular "cell" background mesh with 1 integration point. b) Quadrilateral grid background mesh with 4 integration points. [84]. | 21 |
| Figure 3.6 - a) Transformation of the initial quadrilateral cell into an isoparametric square shape and application of the 2×2 quadrature point rule followed by the return to the initial quadrilateral shape. b) Transformation of the initial triangular cell into an isoparametric triangular shape and application of the 3-point quadrature point rule followed by the return to the initial triangular shape. | 21 |
| Figure 5.1 - Microscopic images of human metaphase chromosomes: (a) chromosome number 2 from normal lymphocytes observed by transmission electron microscopy (TEM) [101]; (b) G-banded human chromosome 10 by scanning electron microscopy (SEM), Bar = $0,5 \mu m$ [102]; (c) Uncoated, G-banded human chromosome 12, viewed at 45° tilt in Cambridge S4-10 electron microscope, Bar = $0,5 \mu m$ [102]. | 38 |

| | |
|---|----|
| Figure 5.2 - 2D models development process. | 39 |
| Figure 5.3 - 3D models development process. | 40 |
| Figure 5.4 - FEMAS Graphical User Interface..... | 41 |
| Figure 6.1 - Artificial chromosome 2D model dimentions. | 43 |
| Figure 6.2 - Models for 2D preliminary studies: (a) stress-strain curve, (b) free vibrations and (c) bending simulations. | 44 |
| Figure 6.3 - Models with increasing number of nodes for discretization convergence study. | 45 |
| Figure 6.4 - Total displacement variation with increasing number of nodes and per numerical method. | 46 |
| Figure 6.5 - Displacement in the neck region variation with increasing number of nodes and per numerical method..... | 46 |
| Figure 6.6 - Equivalent Young modulus in the neck region variation with increasing number of nodes and per numerical method. | 47 |
| Figure 6.7 - 1 st natural vibrational frequency evaluation with increasing number of nodes and per numerical method. | 51 |
| Figure 6.8 - 2 nd natural vibrational frequency evaluation with increasing number of nodes and per numerical method. | 51 |
| Figure 6.9 - 3 rd natural vibrational frequency evaluation with increasing number of nodes and per numerical method. | 52 |
| Figure 6.10 - Total displacement variation with increasing number of layers and per numerical method. | 65 |
| Figure 6.11 - Equivalent Young modulus variation with increasing number of layers and per numerical method. | 65 |
| Figure 6.12 - 1 st natural vibrational frequency evaluation with increasing number of layers and per numerical method. | 69 |
| Figure 6.13 - 2 nd natural vibrational frequency evaluation with increasing number of layers and per numerical method. | 69 |
| Figure 6.14 - 3 rd natural vibrational frequency evaluation with increasing number of layers and per numerical method. | 70 |
| Figure 7.1 - Comparative study of the first 3 natural frequencies of chromosomes 3D models | 99 |

List of Tables

| | |
|---|----|
| Table 2.1 - Conspectus of human mitotic chromosome. [26], [39] | 11 |
| Table 3.1 - Integration points coordinates and weights for quadrilateral "cells". | 22 |
| Table 3.2 - Integration points coordinates and weights for triangular "cells". | 22 |
| Table 5.1 - RPIM Parameters | 42 |
| Table 5.2 - NNRPIM Parameters | 42 |
| Table 6.1 - Displacement (u) field for elasto-static nodal discretization study. | 48 |
| Table 6.2 - von Mises effective stress (σ_{eq}) field for elasto-static nodal discretization study. | 49 |
| Table 6.3 - Equivalent effective strain (ε_{eq}) field for elasto-static nodal discretization study..... | 50 |
| Table 6.4 - Parameterized displacement field of natural vibrational modes 1-3 usig FEM. .. | 53 |
| Table 6.5 - Parameterized von Mises effective stress field of natural vibrational modes 1- 3 usig FEM. | 54 |
| Table 6.6 - Parameterized equivalent effective strain of natural vibrational modes 1-3 usig FEM. | 55 |
| Table 6.7 - Parameterized displacement field of natural vibrational modes 1-3 usig RPIM. .. | 56 |
| Table 6.8 - Parameterized von Mises effective stress field of natural vibrational modes 1-3 usig RPIM. | 57 |
| Table 6.9 - Parameterized equivalent effective strain of natural vibrational modes 1-3 usig RPIM. | 58 |
| Table 6.10 - Parameterized displacement field of natural vibrational modes 1-3 usig NNRPIM. | 59 |
| Table 6.11 - Parameterized von Mises effective stress field of natural vibrational modes 1- 3 usig NNRPIM. | 60 |
| Table 6.12 - Parameterized equivalent effective strain of natural vibrational modes 1-3 usig NNRPIM. | 61 |
| Table 6.13 - Bending test with 1761 nodes model | 62 |

| | |
|--|----|
| Table 6.14 - Schematization of the cross-sectional area at two different points and definition of the thickness of each layer that compose each model. | 63 |
| Table 6.15 - Displacement (u) field for elasto-static 2D shell-like convergence study. | 66 |
| Table 6.16 - von Mises effective stress (σ_{eq}) field for elasto-static 2D shell-like convergence study..... | 67 |
| Table 6.17 - Equivalent effective strain (ε_{eq}) field for elasto-static 2D shell-like convergence study. | 68 |
| Table 6.18 - Parameterized displacement field of natural vibrational modes 1-3 usig FEM: 2D shell-like convergence study. | 71 |
| Table 6.19 - Parameterized von Mises effective stress field of natural vibrational modes 1-3 usig FEM: 2D shell-like convergence study. | 72 |
| Table 6.20 - Parameterized equivalent effective strain field of natural vibrational modes 1-3 usig FEM: 2D shell-like convergence study..... | 73 |
| Table 6.21 - Parameterized displacement field of natural vibrational modes 1-3 usig RPIM: 2D shell-like convergence study. | 74 |
| Table 6.22 - Parameterized von Mises effective stress field of natural vibrational modes 1-3 usig RPIM: 2D shell-like convergence study. | 75 |
| Table 6.23 - Parameterized equivalent effective strain field of natural vibrational modes 1-3 usig RPIM: 2D shell-like convergence study..... | 76 |
| Table 6.24 - Parameterized displacement field of natural vibrational modes 1-3 usig NNRPIM: 2D shell-like convergence study..... | 77 |
| Table 6.25 - Parameterized von Mises effective stress field of natural vibrational modes 1-3 usig NNRPIM: 2D shell-like convergence study..... | 78 |
| Table 6.26 - Parameterized equivalent effective strain field of natural vibrational modes 1-3 usig NNRPIM: 2D shell-like convergence study. | 79 |
| Table 6.27 - Bending test with one layer model | 81 |
| Table 6.28 - Displacement in neck region in 3D model | 82 |
| Table 6.29 - Comparative study of displacement in neck region between 3D model and 2D model with 1741 nodes model from Sec. 6.2.1 - | 82 |
| Table 6.30 - Comparative study of displacement in neck region between 3D model and 2D models from Sec. 6.2.1 - | 83 |
| Table 6.31 - Stress-strain curve simulation using 3D "artificial" chromosome | 84 |
| Table 6.32 - 3D "artificial" chromosome natural vibration frequencies for modes 1-3 | 85 |
| Table 6.33 - Parameterized displacement field of natural vibrational modes 1-3 usig FEM: 3D model..... | 86 |
| Table 6.34 - Parameterized von Mises effective stress field of natural vibrational modes 1-3 usig FEM: 3D model..... | 87 |

| | |
|--|-----|
| Table 6.35 - Parameterized equivalent effective strain field of natural vibrational modes 1-3 usig FEM: 3D model | 88 |
| Table 6.36 - Parameterized displacement field of natural vibrational modes 1-3 usig RPIM: 3D model..... | 89 |
| Table 6.37 - Parameterized von Mises effective stress field of natural vibrational modes 1-3 usig RPIM: 3D model | 90 |
| Table 6.38 - Parameterized equivalent effective strain field of natural vibrational modes 1-3 usig RPIM: 3D model | 91 |
| Table 6.39 - Parameterized displacement field of natural vibrational modes 1-3 usig NNRPIM: 3D model | 92 |
| Table 6.40 - Parameterized von Mises effective stress field of natural vibrational modes 1-3 usig NNRPIM: 3D model | 93 |
| Table 6.41 - Parameterized equivalent effective strain field of natural vibrational modes 1-3 usig NNRPIM: 3D model | 94 |
| Table 6.42 - 3D “artificial” chromosome bending test..... | 95 |
| Table 7.1 - 2D and 3D human chromosomes number 2, 10 and 12 models with nodal distribution. | 98 |
| Table 7.2 - Natural frequencies of modes 1-3 for chromosomes number 2, 10 and 12..... | 98 |
| Table 7.3 - Parameterized displacement field of natural vibrational modes 1-3 using FEM for 3 different 2D human chromosome models. | 100 |
| Table 7.4 - Parameterized von Mises effective stress field of natural vibrational modes 1-3 using FEM for 3 different 2D human chromosome models. | 101 |
| Table 7.5 - Parameterized equivalent effective strain field of natural vibrational modes 1-3 using FEM for 3 different 2D human chromosome models. | 102 |
| Table 7.6 - Parameterized displacement field of natural vibrational modes 1-3 using RPIM for 3 different 2D human chromosome models. | 103 |
| Table 7.7 - Parameterized von Mises effective stress field of natural vibrational modes 1-3 using RPIM for 3 different 2D human chromosome models. | 104 |
| Table 7.8 - Parameterized equivalent effective strain field of natural vibrational modes 1-3 using RPIM for 3 different 2D human chromosome models. | 105 |
| Table 7.9 - Parameterized displacement field of natural vibrational modes 1-3 using NNRPIM for 3 different 2D human chromosome models. | 106 |
| Table 7.10 - Parameterized von Mises effective stress field of natural vibrational modes 1-3 using NNRPIM for 3 different 2D human chromosome models. | 107 |
| Table 7.11 - Parameterized equivalent effective strain field of natural vibrational modes 1-3 using NNRPIM for 3 different 2D human chromosome models. | 108 |
| Table 7.12 - Parameterized displacement field of natural vibrational modes 1-3 using FEM for 3 different 3D human chromosome models. | 109 |

| | |
|--|-----|
| Table 7.13 - Parameterized von Mises effective stress field of natural vibrational modes 1-3 using FEM for 3 different 3D human chromosome models. | 110 |
| Table 7.14 - Parameterized equivalent effective strain field of natural vibrational modes 1-3 using FEM for 3 different 3D human chromosome models. | 111 |
| Table 7.15 - Parameterized displacement field of natural vibrational modes 1-3 using RPIM for 3 different 3D human chromosome models. | 112 |
| Table 7.16 - Parameterized von Mises effective stress field of natural vibrational modes 1-3 using RPIM for 3 different 3D human chromosome models. | 113 |
| Table 7.17 - Parameterized equivalent effective strain field of natural vibrational modes 1-3 using RPIM for 3 different 3D human chromosome models. | 114 |
| Table 7.18 - Parameterized displacement field of natural vibrational modes 1-3 using NNRPIM for 3 different 3D human chromosome models. | 115 |
| Table 7.19 - Parameterized von Mises effective stress field of natural vibrational modes 1-3 using NNRPIM for 3 different 3D human chromosome models. | 116 |
| Table 7.20 - Parameterized equivalent effective strain field of natural vibrational modes 1-3 using NNRPIM for 3 different 3D human chromosome models. | 117 |

Abbreviations

| | |
|--------|--|
| 2D | Bi-dimensional |
| 3D | Tridimensional |
| CT | Computed Tomography |
| DEM | Diffuse Element Method |
| DNA | Deoxyribonucleic Acid |
| EFGM | Element Free Galerkin Method |
| FEA | Finite Element Analysis |
| FEM | Finite Element Method |
| FEMAS | Finite Element and Meshless Method Analysis Software |
| GUI | Graphical User Interface |
| MRI | Magnetic Resonance Imaging |
| NEM | Natural Element Method |
| NNFEM | Natural Neighbor Finite Element Method |
| NNRPIM | Natural Neighbor Radial Point Interpolation Method |
| PIM | Point Interpolation Method |
| RBF | Radial Basis Function |
| RNA | Ribonucleic Acid |
| RPI | Radial Point Interpolators |
| RPIM | Radial Point Interpolation Method |
| SPH | Smooth Particle Hydrodynamics Method |
| STL | Stereo Lithography |

Chapter 1

Introduction

Results from GLOBOCAN [1] show that in 2012 there were more than 14 million new cases of cancer diagnosed worldwide (excluding non-melanoma skin cancer) and over 8 million deaths from cancer. These estimates correspond to age-standardized incidence and mortality rates of 182 and 102 per 100 000, respectively [1], [2].

The progression of normal cells to malignancy and the primary events in the transformation process that leads to cancer emergence are generally thought to be genetic and irreversible. The main causes are attributed to mutations in cellular oncogenes associated with phenotypic changes and specific properties acquisition [3]. These include immortalization (i.e. the acquisition of an infinite lifespan), which makes them achieve a proliferative advantage over the surrounding cells. The arising tumor overtakes the host tissue and, in some cases, becomes invasive and metastatic.

However there is also evidence for the involvement of epigenetic events in cancer development [3]. For example, when cells are subjected to X-irradiation [4], [5] or to carcinogenic chemicals [6], cells become heritably altered such that their progeny have an increased probability of transformation compared to non-affected cells [3].

The current treatment lines for most cancer cases reside in chemotherapy, radiotherapy and surgery [7]. Despite the efforts in the search for new drugs, therapeutic and diagnosing procedures [8], the survival rate of cancer patients has not significantly changed in the last three decades [9]. This is a disease with a high degree of mortality and that can leave survivors with many sequels and requiring constant follow-up.

Singh and collaborators presented evidences [10] indicating that such modifications in normal DNA sequences can induce inappropriate regulation of chromatin structure. A large number of sequence-specific transcription factors regulate gene expression through their ability to remodel chromatin structure, other DNA sequences are directly used for structural proteins binding and others mediate remodeling indirectly [10]. The consequent chromosomal rearrangements may sterically interfere with binding of transcription factors [10], stepping in all cellular metabolism. Most of the implications of gene mutation on chromosome structure and stability were discovered upon closer investigation of some diseases [11], [12] and syndromes [13].

From the knowledge of dynamics and quantum mechanics, all bodies, even in rest, vibrate in a specific and unique way. The mode and frequency of natural vibration of bodies is closely dependent on their shape and mechanical properties. Although two objects appear to be identical, there are distinct microstructural defects that determine distinct vibrational signatures. In this way, and like all bodies, it is also possible to characterize and perform an analysis of chromosomes free vibrations (free vibrations occur when a system vibrates in the absence of any externally applied forces [14]).

Recognizing the global scenario of cancer disease evolution, with the well-known consequences above described, it is imperative to find alternative approaches to these problems. Thus, it is proposed the hypothesis that based on an analysis of free vibrations it is possible to distinguish normal chromosomes from chromosomes that have experienced some degree of mutation. If the hypothesis is proved, it will allow to develop new methods of diagnosis and/or even treatment based on this assumption.

1.1 - Motivation

Experimental studies are surrounded by many limitations that we must keep in mind, for example, the whole process from the discovery of a new therapeutic chemical formula to its clinical use is very time consuming, expensive, difficult and often with results beyond expectations [15], [16]. In contrast, mathematical models seems to be a promising link between conceptual models and experimental testing. Indeed mathematical modelling has proven to be a powerful tool to formalize the conceptual model and simulate proposed experiments *in silico*.

By weighing the advantages and limitations of these models and simulations, the numerous possibilities they can offer prevail. Moreover, in fact, it is the promising results, and in many cases already proven, that allied to its plasticity of applicability and to the already identified needs that fuels the motivation for this work.

1.2 - Objectives

The main objective of this project is to simulate the static and dynamic behavior of human chromosomes at the microscale level.

Therefore, to accomplish this goal, several secondary objectives were stipulated, such as:

- Understand the influence of DNA packing and DNA mutations in chromosome mechanical properties;
- Construction of a simplified 2D and 3D models to simulate human chromosomes;
- Validate the mechanical model through a static analysis, using different numerical methods;
- Perform dynamic (free vibrations) analysis and perform a convergence test;
- Construct 2D and 3D models of different human chromosomes and execute a dynamic analysis using different numerical methods;
- Compare analysis of different chromosomes' results;
- Draw comparisons between FEM and the meshless methods used.

1.3 - Document Structure

The dissertation was organized in several chapters, starting with Chapter 1, in which the theme in study and the main objectives of the work are presented. Chapter 2 starts with a brief historical perspective description followed by an explanation of chromosomes organizational structure and its main mechanical properties experimentally obtained by some authors. Chapter 3 focus on the different numerical methods that can be used to perform computational mechanical simulations, describing briefly their formulation, followed by, in Chapter 4, an introduction of basic notions of solid mechanics. Then, in Chapter 5 the techniques to obtain the biomechanical models are discussed. In Chapter 6 is presented the performed preliminary convergence studies: it was studied the influence of the number of nodes discretizing the problem and it was also tested if defining the 2D models with layers with different thicknesses would approximate to 3D model results. In Chapter 7, is presented the free vibrations study of three different human chromosomes. It was performed a bi-dimensional and tridimensional analysis. At the end, in Chapter 8 the main achievements of the work are presented along with the planning of future work.

Chapter 2

Chromosomes

The beginning of cell biology can be dated back to 1665 and attributed to Robert Hooke who named the observed multiple tiny pores in very thin slices of bottle cork as “cells” [17]. Since then its real structure and function has been studied being the whole course of science full of advances and retreats to the present day. It is important to note that all achievements in science are closely dependent and related to the evolution of technology and both occur simultaneously and are interdependent. The discovery of the cell was only possible because in the end of XVI century a Dutch spectacle maker Zacharias Jansen began to test lenses and with his father help they built the first compound microscope [18]. The three principles of cellular theory [19] were only completed in the XIX century by Rudolf Virchow and it took about 100 years more for James Watson and Francis Crick to suggest what is now accepted as the first correct model of the double-helix structure [20] of DNA, they are also responsible for the central dogma of molecular biology [21].

DNA is a macromolecule that contains the genetic information needed to the growth, development, function and reproduction of all known living organisms and many viruses [22], [23]. The information stored in DNA is arranged in hereditary units, now known as genes. They control identifiable traits of an organism. In the last few decades the scientific community has invested heavily to study, to understand and even to manipulate genes (for example bacterial gene modifications to create vaccines [24]), hoping to solve many of the humanity problems (diseases, food, aesthetics, etc.). The genome of an organism comprises its entire complement of DNA.

As the microscopes evolved (light based microscopes were improving and electron and fluorescent microscopes appear) and became widely available accompanied by the appearance of other techniques [25], biologists were able to examine the internal structure of a wide variety of cells. It became apparent from these studies that there were two basic classes of cells: prokaryotic and eukaryotic; distinguished by their size and the types of internal structures, or organelles, they contain [23]. Within eukaryotic cells, the kind of cell that composes the human body, DNA is organized into long structures called chromosomes. With the exception of eggs and sperm, every normal human cell has 46 chromosomes [26]. Half of these, and thus half of the genes, can be traced back to the mother and the other half, to the father. The DNA in a single human cell, which measures about 2 meters in total length, must be contained within cells with diameters of less than 10 μm , what can be translated in a

compaction ratio higher than 10^5 [22], fact that leads to the conclusion that the packing of DNA is crucial to cell architecture.

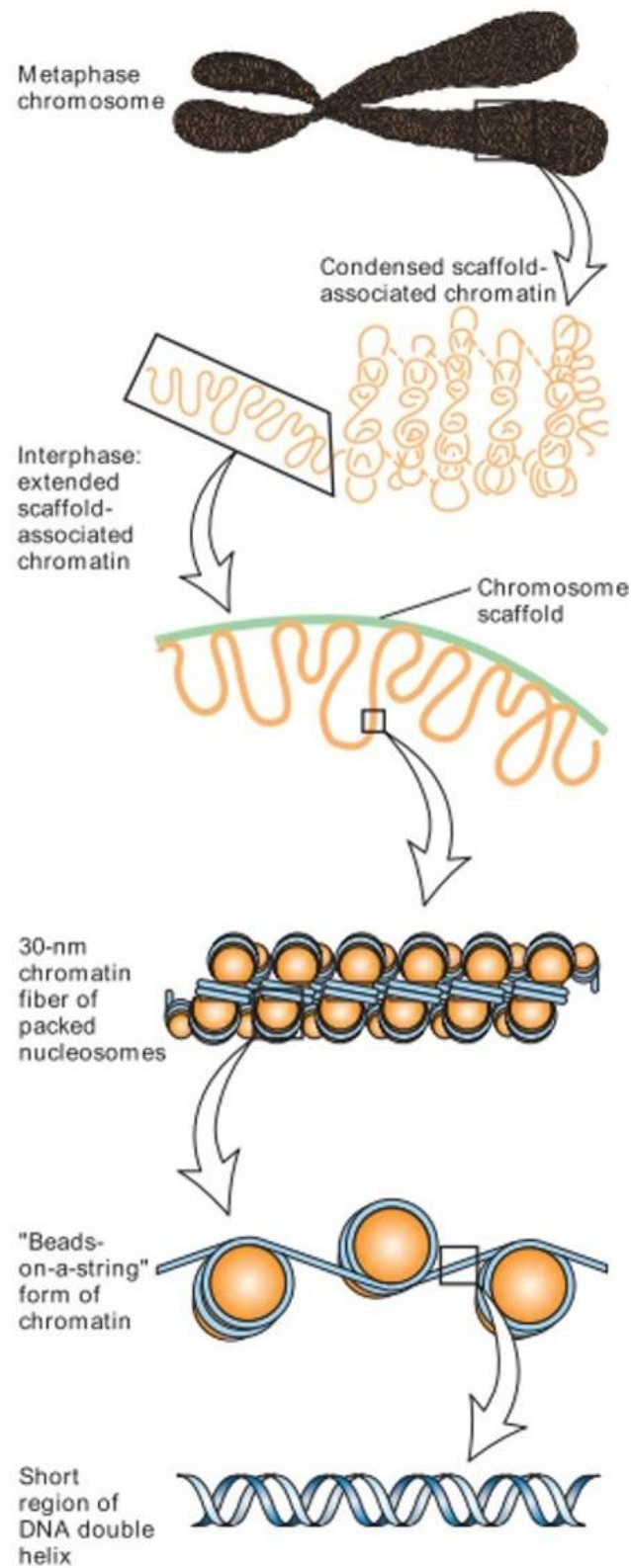


Figure 2.1 - Model for the packing of chromatin and the chromosome scaffold in metaphase chromosomes [22].

During interphase, when cells are not dividing, the genetic material exists as a nucleoprotein complex called chromatin, which is dispersed in the nucleus. Its general structure has been found to be remarkably similar in the cells of all eukaryotes, including fungi, plants, and animals.

2.1 - Anatomical Overview

The DNA molecule is disposed like a wire around a coil being the core constituted by two copies of four different types of proteins called histones forming a nucleosome. X-ray crystallography has shown that the octameric histone core is a roughly disk-shaped molecule made of interlocking histone subunits [22]. This association of DNA with proteins can be considered as the first level of compaction. In its turn, nucleosomes are thought to be packed into an irregular spiral or solenoid arrangement, with approximately six nucleosomes per turn. Condensed chromatin may be quite dynamic, with regions occasionally partially unfolding and then refolding into a solenoid structure.

The chromatin in chromosomal regions that are not being transcribed (special info transfer from DNA into RNA mentioned in the central dogma of molecular biology [21]) exists predominantly in the condensed, 30 nm fiber form and in higher-order folded structures whose detailed conformation is not currently totally understood. Despite the need to accommodate all the DNA inside the cell, the primary functions of mitotic chromosome condensation in eukaryotic cells are to reduce chromosome arm lengths so that they avoid truncation during cell division and to facilitate proper separation and segregation of sister chromatids [27].

Several authors have tried different methods [28]-[31] to prove this model for the organization/compactness of chromatin, illustrated in Figure 2.1, that culminates in the characteristic “X” shape, the chromosome. This “X” shape is maintained by a highly complex multi-protein structure called centromere that binds the two chromosome arms (also known as sister chromatids). For example, Houchmandzadeh and Dimitrov took a mechanical analysis point of view [32] to perform elasticity measurements. They were able to make several conclusions on inner structure of chromosomes and on its mechanical properties.

2.1.1 - The Structure of DNA

The basic building block of DNA is the nucleotide (Figure 2.2 a), a five-carbon sugar *deoxyribose* to which one phosphate is esterified at the 5' position of the sugar ring and one nitrogenous base is attached at the 1' site [23]. The nitrogenous bases present in a nucleic acid can be of two different types: pyrimidines - *thymine* (T) and *cytosine* (C) - which contain a single ring, and purines - *guanine* (G) and *adenine* (A) - which contain two rings (Figure 2.2 b). The nucleotides are covalently linked to one another to form a linear polymer with a backbone composed of alternating sugar and phosphate groups joined by 3'-5'-*phosphodiester bonds* (Figure 2.2 b).

A base composition analysis of a DNA sample (described in [33]) allowed to refute the tetranucleotide theory [34] that argued that each of the four bases would be present as 25% of the total number. Chargaff found that the ratios of the four component bases were quite variable from one type of organism to another, often being very different from the 1:1:1:1 ratio. The number of purines always equaled the number of pyrimidines, more specifically, the number of *adenines* always equaled the number of *thymines*, and the number of *guanines* always

equaled the number of *cytosines*. The DNA base composition can be transcribed in the following rules:

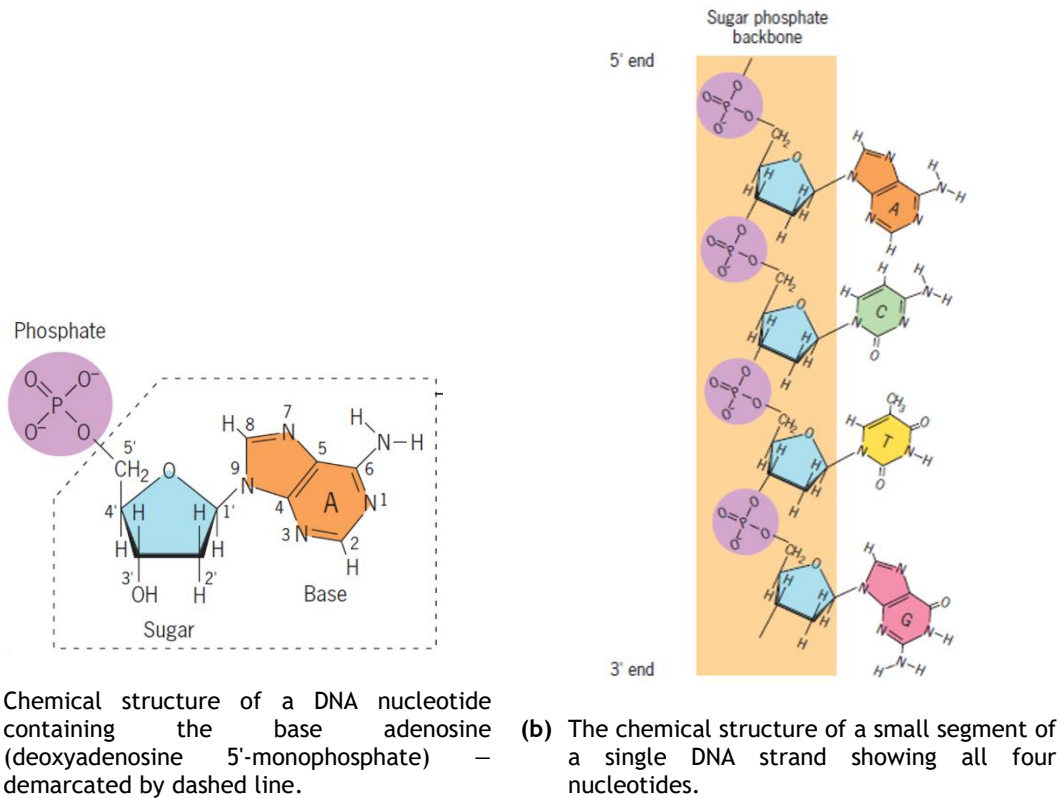


Figure 2.2 - DNA chemical structure. [23]

$$[A] = [T], [G] = [C], [A] + [T] = [G] + [C]. \quad (2.1)$$

Using X-ray diffraction data (obtained by Rosalind Franklin [35], [36] and Maurice Wilkins [37] at King's College London) and models of the four types of nucleotides, Watson and Crick proposed a structure of DNA [20] that included the following aspects, mentioned in [23] (Figure 2.3):

1. The molecule is composed of two chains of nucleotides.
2. The two chains spiral around each other to form a pair of right-handed helices and each strand follows a clockwise path.
3. The two chains comprising one double helix are antiparallel. Thus, if one chain is aligned in the $5' \rightarrow 3'$ direction, its partner must be aligned in the $3' \rightarrow 5'$ direction.
4. The *-sugar-phosphate-sugar-phosphate-* backbone of each strand is located on the outside of the molecule with the two sets of bases projecting toward the center.
5. The bases occupy planes that are approximately perpendicular to the long axis of the molecule and are, therefore, stacked one on top of another like a pile of plates. Hydrophobic interactions and van der Waals forces between the stacked planar bases

provide stability for the entire DNA molecule. Together, the helical turns and planar base pairs cause the molecule to resemble a spiral staircase.

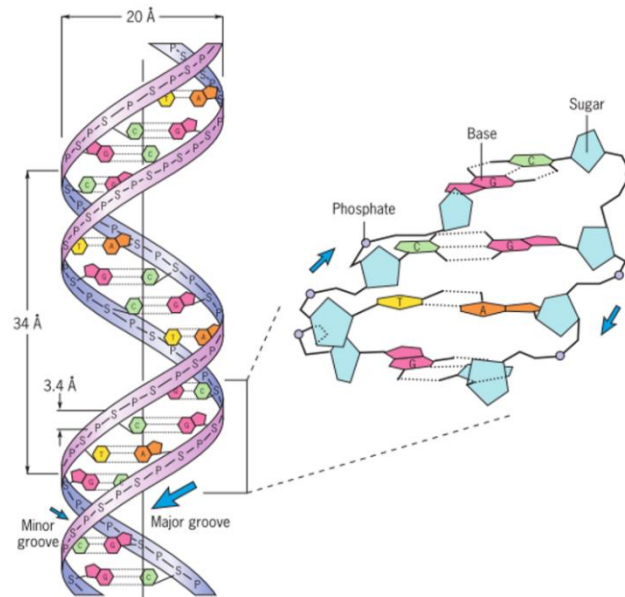


Figure 2.3 - Schematic representation of the DNA double helix. [23]

6. The two strands are held together by hydrogen bonds between each associated pair of bases. Individual hydrogen bonds are weak and easily broken so the DNA strands can become separated during various activities, but the strengths of hydrogen bonds are additive, and the large numbers of hydrogen bonds holding the strands together make the double helix a stable structure.
7. A pyrimidine in one chain is always paired with a purine in the other chain. This arrangement produces a molecule that is 2 nm wide along its entire length.
8. Structural restrictions on the configurations of the bases suggested that adenine was the only purine structurally capable of bonding to thymine and that guanine was the only purine capable of bonding to cytosine. Therefore, the only possible pairs were $A - T$ and $G - C$. Because an $A - T$ and $G - C$ base pair had the same geometry, there were no restrictions on the sequence of bases; a DNA molecule could have any one of an unlimited variety of nucleotide sequences.
9. The spaces between adjacent turns of the helix form two grooves of different width – a wider *major groove* and a more narrow *minor groove* – that spiral around the outer surface of the double helix. Proteins that bind to DNA often contain domains that fit into these grooves. In many cases, a protein bound in a groove is able to read the sequence of nucleotides along the DNA without having to separate the strands.
10. The double helix makes one complete turn every 10 residues (3.4 nm).
11. Because an A on one strand is always bonded to a T on the other strand, and a G is always bonded to a C , the nucleotide sequences of the two strands are always fixed

relative to one another. Because of this relationship, the two chains of the double helix are said to be complementary to one another. For example, *A* is complementary to *T*, $5' - AGC - 3'$ is complementary to $3' - TCG - 5'$, and one entire chain is complementary to the other. Complementarity is of overriding importance in nearly all the activities and mechanisms in which nucleic acids are involved.

2.1.2 - Human Karyotype

The rapid growth of knowledge of human chromosomes in several laboratories, following advances in technical methods, has given rise to several systems by which the chromosomes were named. This has led to confusion in the literature and so to the need for resolving the differences. Consequently, a small study group was convened to attempt the formulation of a common system of nomenclature. Dr. Theodore T. Puck [38] arranged the meeting to be held at Denver in 1960 and it was agreed that the principles to be observed by the system should be simplicity and freedom [39].

The cytologists present in the conference agreed that the autosomes should be serially numbered, 1 to 22, as nearly as possible in descending order of length [39]. The sex chromosomes should continue to be referred to as X and Y, rather than by a number.

It was generally agreed that the 22 autosomes can be classified into seven groups [39], distinction between which can readily be made. Within these groups further identification of individual chromosomes can in many cases be made relatively easily. Within some groups, especially the group of chromosomes numbered 6-12, including also the X-chromosome, the distinctions between the chromosomes were more difficult to make by the available criteria at the time. However, lesser difficulties were encountered in separating chromosomes 6 and the X from the remainder of this group.

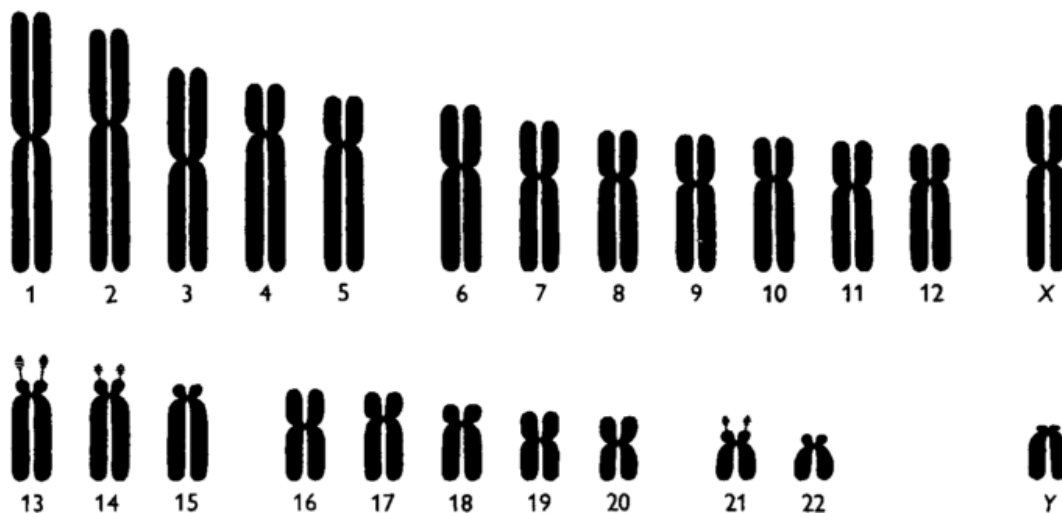


Figure 2.4 - Human karyotype drawn from chromosomes' average measurement values. [39]

Figure 2.4 presents a diagram of a set of chromosomes drawn from average measurement values performed by T. Puck during his experiments and in Table 2.1 are described some of the chromosomes' characteristics belonging to each one of the seven groups.

Table 2.1 - Conspectus of human mitotic chromosome. [26], [39]

| Groups | Description |
|-----------|--|
| 1-3 | Large chromosomes with approximately median centromeres. The three chromosomes are readily distinguished from each other by size and centromere position. |
| 4-5 | Large chromosomes with sub-median centromeres. The two chromosomes are difficult to distinguish, but chromosome 4 is slightly longer. |
| 6-12 + X | Medium-sized chromosomes with sub-median centromeres. The X-chromosome resembles the longer chromosomes in this group, especially chromosome 6, from which it is difficult to distinguish. This large group is the one which presents major difficulty in identification of individual chromosomes |
| 13-15 | Medium-sized chromosomes with nearly terminal centromeres (acrocentric chromosomes). Chromosome 13 has a prominent satellite on the short arm. Chromosome 14 has a small satellite on the short arm. No satellite has been detected on chromosome 15. |
| 16-18 | Rather short chromosomes with approximately median (in chromosome 16) or sub-median centromeres |
| 19-20 | Short chromosomes with approximately median centromeres. |
| 21-22 + Y | Very short, acrocentric chromosomes. Chromosome 21 has a Satellite on its short arm. The Y-chromosome is similar to these chromosomes. |

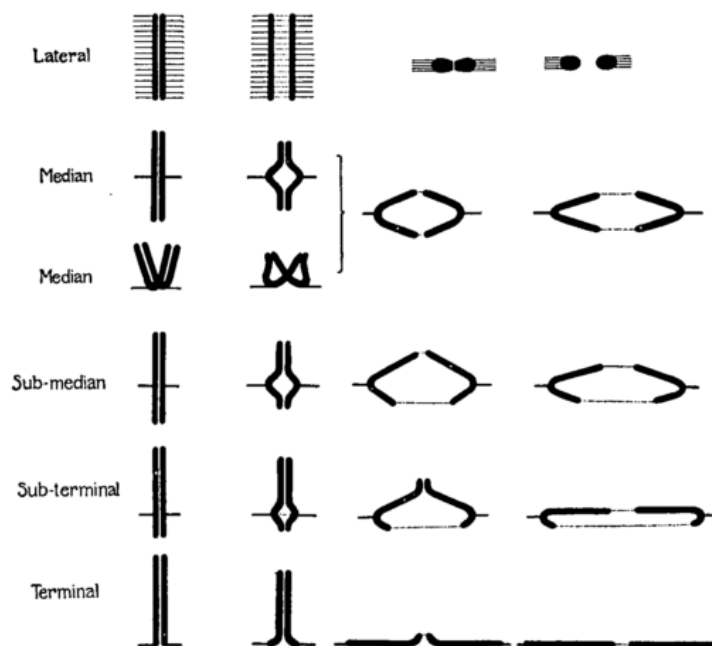


Figure 2.5 - Types of chromosome-attachments and their results during the somatic mitoses. The spindle-fiber attachments indicated by fine lines [40].

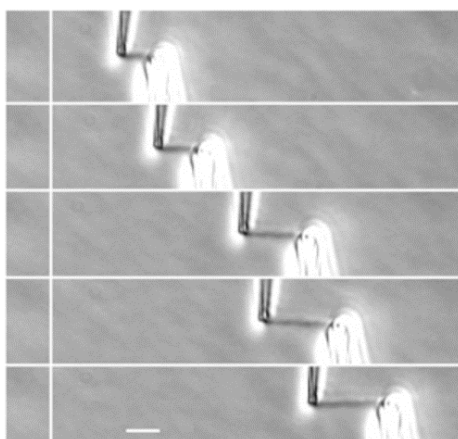
In the morphologic identification of chromosomes, the location of the centromere is the most useful landmark, and one which is characterized by great constancy [41]. In Figure 2.5, the four locations of median, sub-median, sub-terminal and terminal are represented, and, in addition, “lateral”, which corresponds to the modern term “diffuse centromere”.

The location of the centromere is important since it characterizes in part the manner in which the achromatic spindle binds to the chromosome [40] and how both somatic mitosis and meiosis will evolve. In addition, to partially describe how these biological processes will take place, the fact that the centromere may have different locations (along with the different sizes of the arms) leads to a specific characterization of each chromosome.

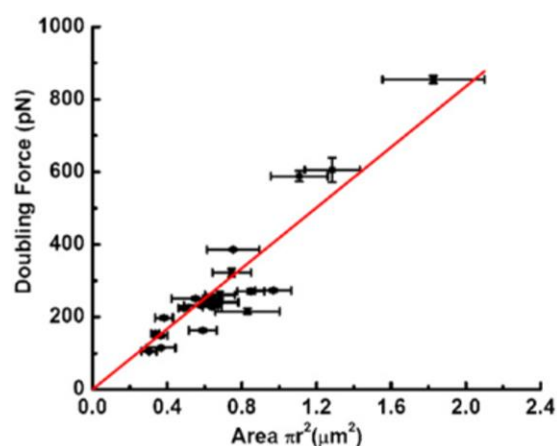
2.2 - Mechanical Properties

Sun and her collaborators performed biophysical experiments [42] on single mitotic chromosomes from human cells, where they combined micromanipulation [43], nano-Newton-scale force measurements and biochemical treatments to study chromosome connectivity and topology. The obtained results were in accordance with previous experiments on amphibian chromosomes [31], [32], [44]-[47] and support the chromatin network model of mitotic chromosome structure. A typical newt chromosome is roughly $2 \mu\text{m}$ thick and $20 \mu\text{m}$ long [42]; the largest human chromosome is about $10 \mu\text{m}$ long and only a little more than $1 \mu\text{m}$ thick [42]. Despite being much smaller, it is possible to do micromanipulation of individual human chromosomes using micron-size glass pipettes.

These investigators found that the force required to double the length of a human chromosome is broadly distributed, with an average of $290 \pm 40 \text{ pN}$ [42]. After taking into account the variation in the thickness of the chromosomes, they found the Young modulus to be more narrowly distributed around an average of $400 \pm 20 \text{ Pa}$ [42]. Figure 2.6 a) shows images collected during the stretching experiment and Figure 2.6 b) shows that indeed the measured doubling forces rise approximately linearly with the square of measured cross-sectional radius of each chromosome.



(a) Images of a human chromosome during a stretching experiment. Bar is $5 \mu\text{m}$.



(b) Plot of force constant versus cross-sectional area from a series of 22 human chromosome-stretching experiments.

Figure 2.6 - Human chromosome stretching experiment and Young modulus calculation. [42]

Measurements of the force produced by the mitotic spindle in anaphase [48] allowed to estimate that $7 \times 10^{-10} N$ is the maximum force produced by the spindle per chromosome.

The Poisson coefficient of human metaphase chromosomes seems not to be described in literature, however it was experimentally obtained for newt lung cells. Since the chemical and structural constitution of the chromosomes is universal to all living eukaryotes, we can assume the proximity of this mechanical property and consider $\nu = 0.069 \pm 0.005$ [46], [49].

The cellular interior can be described as a homogeneous linear viscoelastic medium [50]-[52] and the cytoplasm of practically all living cells, from bacteria to mammals, is a highly crowded and structured fluid in which up to 40% of the total mass is contributed by dissolved macromolecules [52], [53]. The total macromolecular concentration (proteins, lipids, nucleic acids, and sugars) can be as high as $400 mg/cm^3$ [52] and cytoplasm has a density of $1.03 g/cm^3$ [22]. In the nucleus, crowding is further enhanced by the hierarchically organized chromatin and chromosomes have in average a density of $1.7 g/cm^3$ [23].

Chapter 3

Numerical Methods

Many phenomena in nature such as fluid flow, heat conduction, electromagnetic fields or either stress in mechanical structures can be described by mathematical laws and modulated using partial differential equations. Nevertheless, in general, none of these equations can be solved symbolically or analytically due to its complexity: this events may involve domains of one, two or more dimensions, nonlinear effects and complex geometries. Moreover, it is also required to take into account the loading systems and boundary conditions. In this context, numerical methods [54] appear as the possible tool used to obtain approximate solutions for these problems [55].

Thanks to the advancement of high-speed digital computers, the cost-effectiveness of numerical procedures has been greatly enhanced, and these methods have become very accurate and reliable [56], versatile and a powerful tool to be used to solve almost all the complex problems in engineering practice [57]. Indeed, a large number of practical engineering problems would not be solved today without the use of these methods that have been widely used, not only for providing new solutions to the problems of academic interest by researchers and scientists, but also for making designs of specific engineering problems.

This chapter begins with a very brief introduction about the FEM, followed by a more detailed analysis of two meshless methods, namely the RPIM and the NNRPIM, reporting some of the most important concepts of these two numerical methods.

3.1 - FEM

The Finite Element Method is a well-known and widely used numerical method [58], [59]. FEM approach consists of dividing the domain of the problem into a finite number of pieces called *elements* and for each one of them the field function is interpolated by simple functions, the shape functions [54], [60], [61]. FEM is then characterized by the discretization of the domain into several subdomains, called finite elements [56], forming a computational mesh as illustrated in Figure 3.1. These elements can be irregular and possess different properties enabling the discretization of structures with mixed properties [56]. The solution for the global system is obtained assembling the results for each element.

Its various applications include the analysis of structures for industry purposes [62] but also for biomechanical studies [63], supporting and providing new advances with applicability in

health field. The FEM was already used to evaluate the influence of the implant design and material on the stress distribution in the surrounding bone tissue [64]-[66] but also in the biomechanical study of childbirth and its consequences for the parturient soft tissues [67].

The major advantage of the FEM is the discretization procedure. However, this method is not free of limitations. The main one is related with the mesh based-interpolation [68], [69]. In fact, in various studies, such as the simulation of crack propagation, the creation of an appropriate mesh is very difficult because the mesh should adapt itself during the simulation process [70].

Special attention has to be given to the quality of the mesh (number, type and shape of elements), because low quality meshes lead to high values of error. Additionally, in order to impose accurately the natural and essential boundary conditions, it is necessary to identify the nodal location of distributed loads, as well as, the nodal position and nature of support/boundary conditions by fixing certain nodal degrees-of-freedom [57]. Being a classical mesh-based method, FEM is not suitable to treat problems with discontinuities that do not align with element edges [69].

It is clear that the finite element solution will solve only the selected mathematical model and that all assumptions in this model will be reflected in the predicted response [59]. We cannot expect any more information in the prediction of physical phenomena than the information contained in the mathematical model. Hence, the choice of an appropriate mathematical model is crucial and completely determines the insight into the actual physical problem that we can obtain by the analysis.

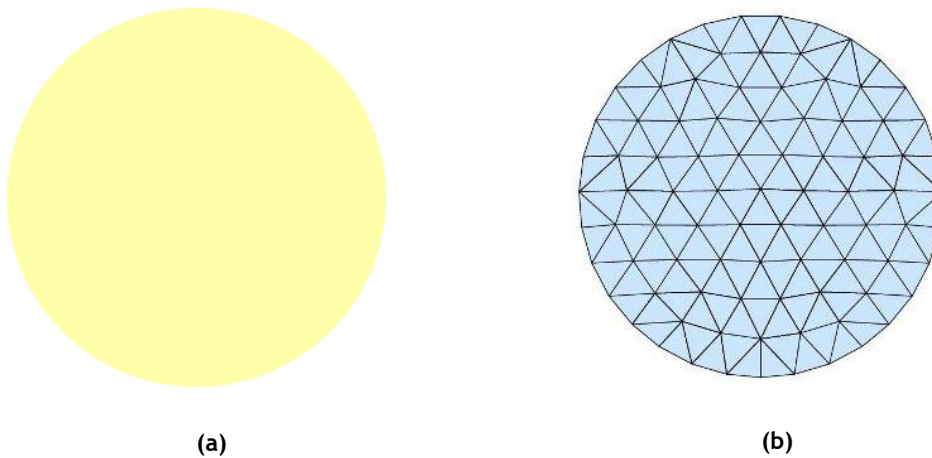


Figure 3.1 - Example of a mesh discretized for the FEM: (a) original, and (b) obtained mesh after discretization.

3.2 - Meshless Methods

Intending to overcome some drawbacks and limitations of the FEM, other numerical methods were created and offered as solid options. Meshless methods [69], [71], [72] arose as a possible alternative and have been under improvement [68]. In this case, the nodes can be arbitrary distributed, once the field functions are approximated within an influence-domain rather than an element [71], [73], [74]. In opposition to the no-overlap rule between elements in the FEM, in meshless methods the influence-domains may and must overlap each other. A meshless

method comprehends three different phases: the shape function construction, the formulation and the integration [74].

These methods present several advantages. The most relevant are the ability to provide more accurate approximations than FEM for structures with complex geometries, such as the case of biological studies, and the capacity to deal with large deformation problems [68].

These kind of methods can be classified in two categories regarding its formulation. The first one is the strong formulation in which the partial differential equations describing the phenomenon are used directly to obtain the solution [74]. One of the first methods created in this category was the SPH, it was initially used for modeling astrophysical phenomena but after several improvements its applications extended to various engineering studies, such as fluid flow analysis [75]. A parallel path on the development of meshless methods was initiated in the nineteen's decade using this time a weak form solution. In weak formulation, each differential equation has a residual weight to be minimized. The residual is not given by the exact solution of the differential but by an approximated function affected by a test function [74]. The first method using this formulation was the DEM [76]. This method was extended by Belytschko originating one of the most well-known methods, the EFGM [77].

The Meshless Methods described above are similar to FEM in the fact that they only allow approximate solutions, and in spite of the successful applications of these type of meshless methods in computational mechanics, some problems remained unsolved. One of the main problems is that the essential boundary conditions cannot be imposed directly, a consequence of the lack of the Kronecker delta property on the shape functions [68], [74]. Due to this fact, several interpolant meshless methods were developed, such as PIM [70], the RPIM [78], [79], NNFEM [80] and the NEM [81], [82]. Later, the combination between the NEM and the RPIM originated the NNRPIM [74], [83].

3.2.1 - Meshless Generic Procedure

The only information required to start the process is the spatial location of each node discretizing the problem domain. It should be noted that this nodal distribution do not form a mesh, since it is not required any kind of previous information about the relation between each node in order to construct the approximation or interpolation functions of the unknown variable field function [74]. In Figure 3.2, it is possible to observe an illustration of this process using either a regular or irregular nodal set.

The use of different kinds of nodal distributions will have a direct effect on the outcome of the numerical analysis. An irregular mesh can often present a lower accuracy on its general results, but it can also enhance results on locations with predictable stress concentrations [84] by having a higher nodal density on those locations. In order to enhance results on these locations, without compromising the accuracy throughout the problem's domain, the best approach is usually to use a regular mesh and to insert extra nodes on those spots.

After the discretization, nodal connectivity can be imposed using either influence-domains or Voronoï diagrams. Then, the construction of a background integration mesh is needed. As in FEM, it is common to use Gaussian integration meshes fitted to the problem domain. However there are other techniques, such as the use of the nodal integration, by means of the Voronoï diagrams in order to obtain the integration weight on each node [74]. The following step is the establishment of the equation system, which can be formulated using approximation or interpolation functions. The interpolation functions possess an important property - the

Kronecker delta property - meaning that the obtained function passes through all scattered points in an influence domain. This property is an important advantage, since it allows the use of the same simple techniques used in FEM to impose the essential boundary conditions.

Thus, after a brief analysis of the generic procedure of meshless methods, it is possible to conclude that a meshless method requires the presence and combination of three basic parts: nodal connectivity, numerical integration scheme and shape functions. These three concepts will be analyzed and, since RPIM and NNRPIM differ in respect to both nodal connectivity and numerical integration scheme, the following sections will explain with detail these differences.

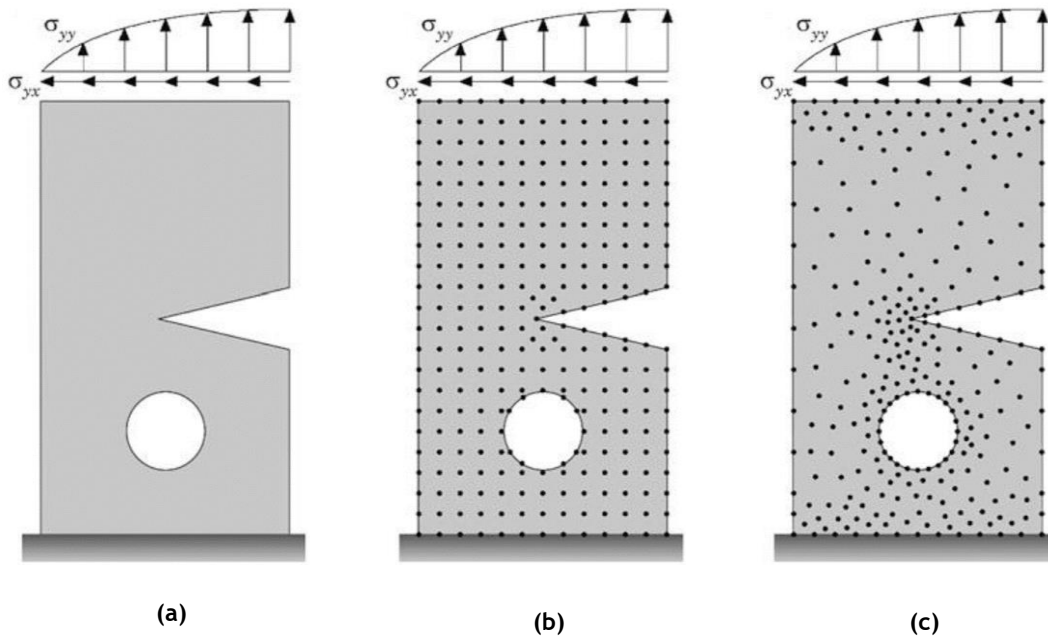


Figure 3.2 - Nodal discretization of the problem domain: (a) Solid domain; (b) Regular nodal discretization; (c) Irregular nodal discretization. [74]

3.2.2 - Nodal Connectivity

3.2.2.1 - RPIM

The RPIM uses the Galerkin weak form formulation to obtain the discrete equation system. The shape functions are constructed using a polynomial basis and a RBF. In RPIM, the nodal connectivity is obtained by the overlap of the influence domain of each node. Influence-domains are found by searching enough nodes inside a certain area or volume, and can have a fixed or a variable size. Many meshless methods [70], [85], [86] use fixed size influence-domains, but RPIM uses a fixed number of neighbor nodes instead.

Regarding fixed size influence-domains, in Figure 3.3, it is presented an example of two types of fixed size domains, a rectangular (Figure 3.3 a) and a circular (Figure 3.3 b). By analyzing these figures, it is possible to note that influence-domains with different shapes and sizes originate a different nodal connectivity. Also, depending on the initial nodal spatial distribution, the obtained influence-domains can be unbalanced, not containing an approximately constant number of nodes. All of these factors can affect the final solution of the problem and cause loss of accuracy in the numerical analysis.

Therefore, to overcome these limitations, RPIM uses variable size influence-domains, with constant number of nodes inside the domain. Thus, performing a radial search and using the interest point x_i as center, the n closest nodes are found. In Figure 3.3 c), this process is illustrated, culminating in a constant nodal connectivity that avoids the numerical problems previously identified.

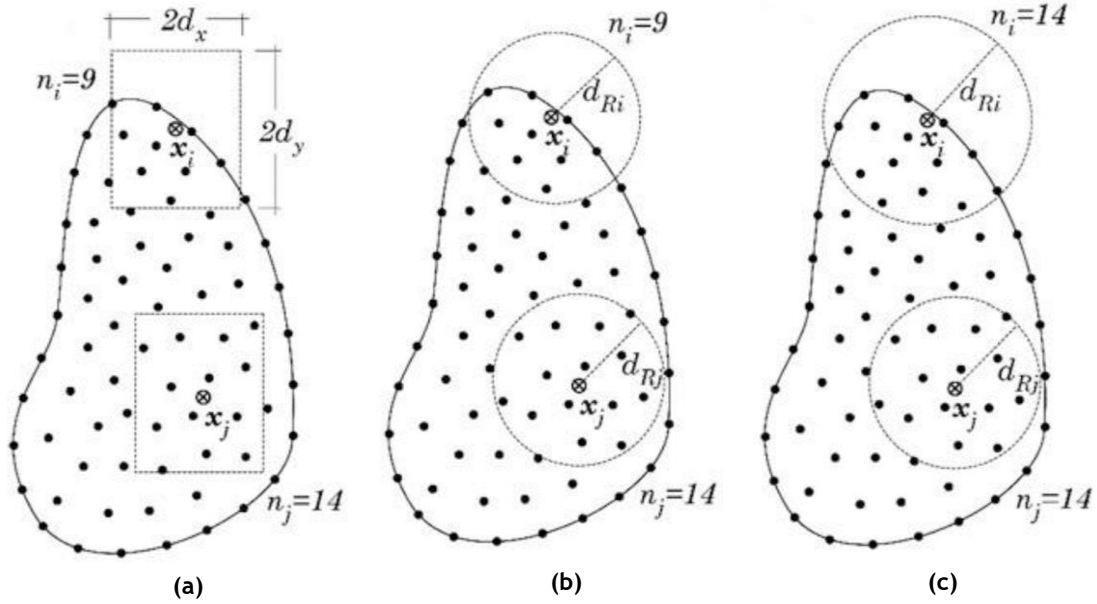


Figure 3.3 - Examples of different types of influence-domains: (a) fixed rectangular shaped influence-domain, (b) fixed circular shaped influence-domain and (c) flexible circular shaped influence-domain. [74]

3.2.2.2 - NNRPIM

The NNRPIM is an advanced discretization meshless technique combining the natural neighbor geometric concept with the RPI [87].

Nodal connectivity is obtained using the natural neighbor concept with the partition of the discretized domain into a set of Voronoï cells [88]. To each one of these cells is associated one and only one node [87]. Considering a problem domain $\Omega \subset \mathbb{R}^d$, bounded by a physical boundary $\Gamma \in \Omega$, discretized in several randomly distributed nodes $N = \{n_0, n_1, \dots, n_N\} \in \mathbb{R}^2$ with the following coordinates: $X = \{x_0, x_1, \dots, x_N\} \in \Omega$, the Veronoï cell is defined by

$$V_i := \{x_l \in \Omega \subset \mathbb{R}^d : \|x_l - x_i\| < \|x_l - x_j\|, \forall i \neq j\} \quad (3.1)$$

being x_l an interest point of the domain and $\|\cdot\|$ the Euclidian metric norm [74]. Thus, the Voronoï cell V_i is the geometric place where all points in the interior V_i are closer to the node n_i than to any other node [74]. The assemblage of the Voronoï cells define the Voronoï diagram. Thus, the Voronoï diagram of N is the partition of the domain defined by Ω into sub regions V_i , closed and convex, as can be seen in Figure 3.4 a).

To respond to the disadvantages of the approach shown in Sect. 3.2.2.1 - and described in Figure 3.3 a), the influence-cell concept was developed [83] and is used by NNRPIM. We can distinguish two types of influence-cells: the "first degree influence-cell", Figure 3.4 a), and the

"second degree influence-cell", Figure 3.4 b). To establish them, a point of interest, x_I , starts by searching for its neighbor nodes following the Natural Neighbor Voronoï construction, considering only its first natural neighbors the first degree influence-cell is obtained. Then, based again on the Voronoï diagram, the natural neighbors of the first natural neighbors of x_I are added to the influence-cell constituting the second degree influence-cell.

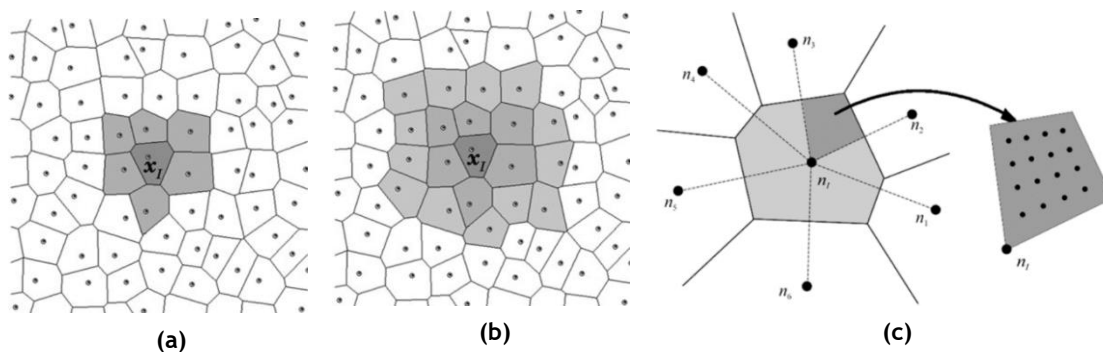


Figure 3.4 - (a) First degree influence-cell. (b) Second degree influence-cell. (c) Representation of the sub-cells forming the Voronoï cell and schematic representation of 4×4 integration points inside a sub-cell. [87]

3.2.3 - Numerical Integration

3.2.3.1 - RPIM

Following the definition of nodal connectivity, the next step would be the numerical integration. For the integration of the differential equations the RPIM uses the Gauss-Legendre integration scheme being need, as it was stated above, a background integration mesh. For this integration mesh it can be used either the cells created to connect the nodes that discretized the problem's domain (resulting in either quadrilateral or triangular cells), or a regular mesh larger than the domain and whose integration points located outside the domain must be eliminated from the computation. On Figure 3.5 it is possible to see the use of triangular cells in a) and the use of the larger regular mesh in b).

Inside of each cell of the background integration mesh, being it triangular or quadrilateral, it is possible to distribute integration points as seen in Figure 3.5 a) and b). On Table 3.1 and Table 3.2 are displayed the locations and weights of the isoparametric integration points for quadrilateral and triangular cells respectively.

After the integration points have been distributed in the isoparametric shape, the Cartesian coordinates of the integration points are obtained using the following isoparametric interpolation functions:

$$x = \sum_{i=1}^m N_i(\xi, \eta) \cdot x_i \quad (3.2)$$

$$y = \sum_{i=1}^m N_i(\xi, \eta) \cdot y_i \quad (3.3)$$

where m is the number of nodes that define the element and x_i and y_i are the cartesian coordinates of the cells nodes. In Figure 3.6 can be seen a representation of this transformation.

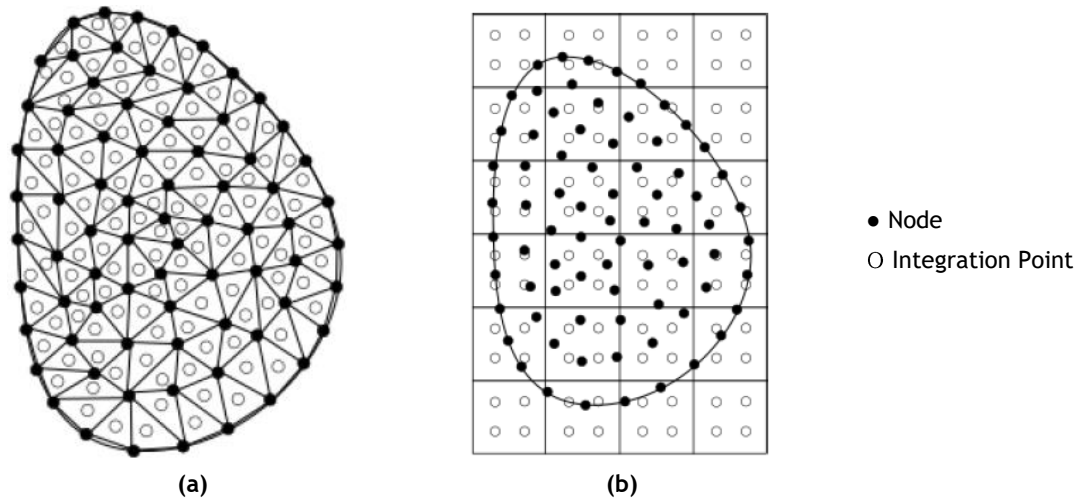


Figure 3.5 - a) Triangular "cell" background mesh with 1 integration point. b) Quadrilateral grid background mesh with 4 integration points. [84]

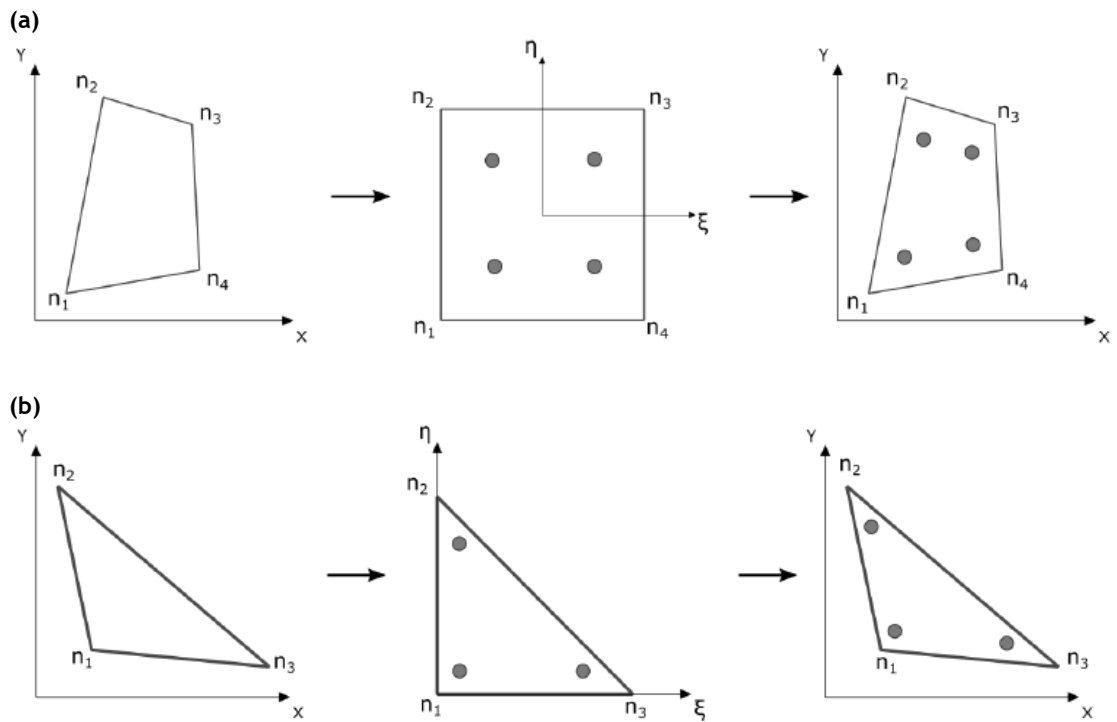


Figure 3.6 - a) Transformation of the initial quadrilateral cell into an isoparametric square shape and application of the 2×2 quadrature point rule followed by the return to the initial quadrilateral shape. b) Transformation of the initial triangular cell into an isoparametric triangular shape and application of the 3-point quadrature point rule followed by the return to the initial triangular shape.

Table 3.1 - Integration points coordinates and weights for quadrilateral "cells".

| Points | ξ | η | Weight |
|--------|-----------------------|-----------------------|-----------------|
| a | 0 | 0 | 4 |
| a | $-\frac{1}{\sqrt{3}}$ | $-\frac{1}{\sqrt{3}}$ | 1 |
| b | $+\frac{1}{\sqrt{3}}$ | $-\frac{1}{\sqrt{3}}$ | 1 |
| c | $-\frac{1}{\sqrt{3}}$ | $+\frac{1}{\sqrt{3}}$ | 1 |
| d | $+\frac{1}{\sqrt{3}}$ | $+\frac{1}{\sqrt{3}}$ | 1 |
| a | $-\sqrt{\frac{3}{5}}$ | $-\sqrt{\frac{3}{5}}$ | $\frac{25}{81}$ |
| b | 0 | $-\sqrt{\frac{3}{5}}$ | $\frac{40}{81}$ |
| c | $+\sqrt{\frac{3}{5}}$ | $-\sqrt{\frac{3}{5}}$ | $\frac{25}{81}$ |
| d | $-\sqrt{\frac{3}{5}}$ | 0 | $\frac{40}{81}$ |
| e | 0 | 0 | $\frac{64}{81}$ |
| f | $+\sqrt{\frac{3}{5}}$ | 0 | $\frac{40}{81}$ |
| g | $-\sqrt{\frac{3}{5}}$ | $+\sqrt{\frac{3}{5}}$ | $\frac{25}{81}$ |
| h | 0 | $+\sqrt{\frac{3}{5}}$ | $\frac{40}{81}$ |
| i | $+\sqrt{\frac{3}{5}}$ | $+\sqrt{\frac{3}{5}}$ | $\frac{25}{81}$ |

Table 3.2 - Integration points coordinates and weights for triangular "cells".

| Points | ξ | η | Weight |
|--------|---------------|---------------|------------------|
| a | $\frac{1}{3}$ | $\frac{1}{3}$ | $\frac{1}{2}$ |
| a | $\frac{1}{6}$ | $\frac{1}{6}$ | $\frac{1}{6}$ |
| b | $\frac{2}{3}$ | $\frac{1}{6}$ | $\frac{1}{6}$ |
| c | $\frac{1}{6}$ | $\frac{2}{3}$ | $\frac{1}{6}$ |
| a | $\frac{1}{3}$ | $\frac{1}{3}$ | $-\frac{27}{96}$ |
| b | $\frac{1}{5}$ | $\frac{1}{5}$ | $\frac{25}{96}$ |
| c | $\frac{3}{5}$ | $\frac{1}{5}$ | $\frac{25}{96}$ |
| d | $\frac{1}{5}$ | $\frac{3}{5}$ | $\frac{25}{96}$ |

The Nodal shape functions (N_i) are define for quadrilaterals as:

$$N_1(\xi, \eta) = \frac{1}{4}(1 - \xi)(1 - \eta);$$

$$N_2(\xi, \eta) = \frac{1}{4}(1 - \xi)(1 + \eta);$$

$$N_3(\xi, \eta) = \frac{1}{4}(1 + \xi)(1 + \eta);$$

$$N_4(\xi, \eta) = \frac{1}{4}(1 + \xi)(1 - \eta);$$

(3.4)

and for triangles as:

$$\begin{aligned} N_1(\xi, \eta) &= 1 - \xi - \eta; \\ N_2(\xi, \eta) &= \eta; \\ N_3(\xi, \eta) &= \xi. \end{aligned} \quad (3.5)$$

The integration weight of the integration point is obtained by multiplying the isoparametric weight of the correspondent point with the Jacobian matrix determinant of the respective cell, as described in Equation (3.6).

$$[J] = \begin{pmatrix} \frac{\partial x}{\partial \xi} & \frac{\partial x}{\partial \eta} \\ \frac{\partial y}{\partial \xi} & \frac{\partial y}{\partial \eta} \end{pmatrix} \quad (3.6)$$

The differential equation integration is finally done using,

$$\int_{-1}^1 \int_{-1}^1 f(\mathbf{X}) dx dy = \sum_{i=1}^m \sum_{j=1}^n \omega_i \omega_j f(\mathbf{X}) \quad (3.7)$$

where ω_i and ω_j is the weight in each direction of the integration point \mathbf{X} .

This integration method can be extrapolated for three dimensional problems using for this tetrahedral solids instead.

3.2.3.2 - NNRPIM

Since the NNRPIM uses the Galerkin weak form, a background integration mesh is necessary. In this method, the integration mesh is obtained using directly and exclusively the nodal distribution, namely the previously constructed Voronoï diagram [83]. Using the Delaunay triangulation, the area of each Voronoï cell is subdivided in several sub-areas. Thus, each area of the Voronoï cell of node x_j , A^{Vj} , is divided into k sub-areas A_i^{Vj} , in which $A_i^{Vj} = \sum_{i=1}^k A_i^{Vj}$, as can be seen in Figure 3.4 c). Then, following the Gauss-Legendre quadrature rule, it is possible to distribute integration points inside each subarea A_i^{Vj} . In Figure 3.4 c), it is exemplified a 4×4 distribution. By repeating the mentioned procedure for the N Voronoï cells from the Voronoï diagram, the background integration mesh discretizing the problem domain is obtained.

Previous research works on the NNRPIM show that one integration point per sub-area A_i^{Vj} is sufficient to integrate accurately the integro-differential equations [83], [87].

3.2.4 - Interpolation Functions

Considering the RPIM and the NNRPIM, the interpolation functions for both methods possess the Kronecker delta property, satisfying the following condition:

$$\varphi_i(\mathbf{x}_j) = \delta_{ij}, \quad (3.8)$$

where δ_{ij} is the Kronecker delta, $\delta_{ij} = 1$ if $i = j$ and $\delta_{ij} = 0$ if $i \neq j$. This property simplifies greatly the process of imposition of the essential boundary conditions, because it allows to apply them directly in the stiffness matrix.

The interpolation functions for both methods are determined using the RPI technique [78], which requires the combination of a polynomial basis with a RBF. Therefore, considering the function $u(x_I)$ defined in the domain $\Omega \subset \mathbb{R}^2$, the value of function $u(x_I)$ at the point of interest x_I is defined by:

$$u(x_I) = \sum_{i=1}^n R_i(x_I) \cdot a_i(x_I) + \sum_{j=1}^m p_j(x_I) \cdot b_j(x_I) = \mathbf{R}^T(x_I) \cdot \mathbf{a}(x_I) + \mathbf{p}^T \cdot \mathbf{b}(x_I) \quad (3.9)$$

where $R_i(x_I)$ is the RBF, $p_j(x_I)$ is the polynomial basis function and $a_i(x_I)$ and $b_j(x_I)$ are non-constant coefficients of $R_i(x_I)$ and $p_j(x_I)$, respectively [87]. The variable defined on the RBF is the distance r_{Ii} between the relevant node x_I and the neighbour node x_i , given by $r_{Ii} = \|x_i - x_I\|$. The most frequently used globally supported RBFs are the multi-quadrics (MQ) functions [89], $R_i(x_I) = R(r_{Ii}) = (r_{Ii}^2 + c^2)^p$, in which shape parameter c takes a value close to zero, $c \cong 0$, and p close to one, $p \cong 1$ [83], [90]. These parameters need to be determined and optimized in order to obtain accurate results. Regarding the Equation (3.9), it is still needed to obtain the non-constant coefficients a and b . The polynomial basis functions used have the following monomial term as

$$\mathbf{p}^T(x_I) = [1, x, y, x^2, xy, y^2, \dots]. \quad (3.10)$$

Considering Equation (3.9) for each node inside the influence-cell domain and including an extra equation, $\sum_{i=1}^n p_j(x_I) a_i = 0$, in order to guarantee a unique solution [91], a system of equations is obtained:

$$\begin{bmatrix} \mathbf{R} & \mathbf{p} \\ \mathbf{p}^T & \mathbf{0} \end{bmatrix} \begin{Bmatrix} \mathbf{a} \\ \mathbf{b} \end{Bmatrix} = \begin{Bmatrix} \mathbf{u}_S \\ \mathbf{0} \end{Bmatrix}. \quad (3.11)$$

Through this system of equations, and being the vector of the nodal function values for the nodes on the influence-cell defined by: $\mathbf{u}_S = \{u_1, u_2, \dots, u_n\}^T$ these coefficients are determined (Eq. (3.12)).

$$\begin{Bmatrix} \mathbf{a} \\ \mathbf{b} \end{Bmatrix} = \begin{bmatrix} \mathbf{R} & \mathbf{p} \\ \mathbf{p}^T & \mathbf{0} \end{bmatrix}^{-1} \begin{Bmatrix} \mathbf{u}_S \\ \mathbf{0} \end{Bmatrix} \Rightarrow \begin{Bmatrix} \mathbf{a} \\ \mathbf{b} \end{Bmatrix} = \mathbf{M}^{-1} \begin{Bmatrix} \mathbf{u}_S \\ \mathbf{0} \end{Bmatrix} \quad (3.12)$$

Recalling that a certain field variable value for an interest point x_I is interpolated using the shape function values obtained at the nodes inside the support domain of x_I , it is now possible to define the interpolation function, by substituting in Equation (3.9) the result from Eq. (3.12). The interpolation function $\Phi(x_I) = \{\varphi_1(x_I), \varphi_2(x_I), \dots, \varphi_n(x_I)\}$ for an interest point x_I is then defined by

$$u(x_I) = \{\mathbf{R}^T(x_I), \mathbf{p}^T(x_I)\} \mathbf{M}^{-1} \begin{Bmatrix} \mathbf{u}_S \\ \mathbf{0} \end{Bmatrix} = \Phi(x_I) \begin{Bmatrix} \mathbf{u}_S \\ \mathbf{0} \end{Bmatrix}. \quad (3.13)$$

In order to compute the partial derivatives of the interpolated field function, it is necessary to obtain the respective RPI shape functions partial derivatives. For a 2D problem the partial derivatives of $\phi(x_I)$ are defined as:

$$\begin{aligned}\Phi_{,x}(\mathbf{x}_I) &= \{\mathbf{R}^T(\mathbf{x}_I), \mathbf{p}^T(\mathbf{x}_I)\}_{,x} \mathbf{M}^{-1}; \\ \Phi_{,y}(\mathbf{x}_I) &= \{\mathbf{R}^T(\mathbf{x}_I), \mathbf{p}^T(\mathbf{x}_I)\}_{,y} \mathbf{M}^{-1}.\end{aligned}\quad (3.14)$$

The first order partial derivative of the RBF vector with respect to the same 2D problem is defined as:

$$\mathbf{R}(\mathbf{x}_I)_{,x} = \{R_1(\mathbf{x}_I)_{,x} \ R_2(\mathbf{x}_I)_{,x} \ \dots \ R_n(\mathbf{x}_I)_{,x}\}^T = \left\{ \frac{\partial R_1(\mathbf{x}_I)}{\partial x} \ \frac{\partial R_2(\mathbf{x}_I)}{\partial x} \ \dots \ \frac{\partial R_n(\mathbf{x}_I)}{\partial x} \right\}^T \quad (3.15)$$

$$\mathbf{R}(\mathbf{x}_I)_{,y} = \{R_1(\mathbf{x}_I)_{,y} \ R_2(\mathbf{x}_I)_{,y} \ \dots \ R_n(\mathbf{x}_I)_{,y}\}^T = \left\{ \frac{\partial R_1(\mathbf{x}_I)}{\partial y} \ \frac{\partial R_2(\mathbf{x}_I)}{\partial y} \ \dots \ \frac{\partial R_n(\mathbf{x}_I)}{\partial y} \right\}^T \quad (3.16)$$

being the partial derivatives of the MQ-RBF obtained with

$$\frac{\partial R_1(\mathbf{x}_I)}{\partial x} = -2p(r_{iI}^2 + c^2)^{p-1}(x_i - x_I) \quad (3.17)$$

$$\frac{\partial R_1(\mathbf{x}_I)}{\partial y} = -2p(r_{iI}^2 + c^2)^{p-1}(y_i - y_I). \quad (3.18)$$

It is possible to extend these formulations to a 3D problem by considering the third dimension (zz axis).

Chapter 4

Solid mechanics

In this chapter the mechanical fundamentals behind the numerical applications presented in this work are developed. Firstly, it is present a brief exposition of the continuum formulation where are shown the solid kinematics and constitutive equations. Following, it is presented the used weak form and the consequent generated discrete system.

The continuum mechanics is the foundation of the nonlinear numerical analysis. It is known that solids and structures subjected to loads or forces become stressed. These stresses lead to strains, which can be interpreted as deformations or relative displacements [74].

The concepts of strain and stress are introduced, followed by an explanation of the equilibrium and the used constitutive equations. In this work, only isotropic and linear elastic materials are considered. In solid elastic materials, the deformation in the solid caused by loading disappears fully with the unloading. For isotropic materials, the material properties do not change with the direction.

4.1 - Fundamentals

The study of Solid Mechanics is mainly devoted on the relationships between stress and strain and strain and displacements, for a given solid and boundary conditions (external forces and displacements constrains) [92]. So, when analyzing a deformation, the consequent change in the body configuration is defined by the stress and the strain terms. This way, the virtual work can be expressed as an integral over the known body volume. It is important to guarantee that both strain tensor and stress tensor are referred to the same deformed state. For simplicity sake, only the 2D deformation theories are here presented, nevertheless, it is possible to find in the literature extensive descriptions concerning the 3D deformation theory [74]. To represent the stresses of the current configuration, the symmetric Cauchy stress tensor, Λ , can be defined as:

$$\Lambda = \begin{bmatrix} \sigma_{xx} & \sigma_{xy} \\ \sigma_{yx} & \sigma_{yy} \end{bmatrix}. \quad (4.1)$$

This work, uses the Voigt notation, expressing tensors in column vectors. Therefore, stress tensor Λ is reduced to the stress vector σ ,

$$\boldsymbol{\sigma} = \{\sigma_{xx} \sigma_{yy} \sigma_{xy}\}^T \quad (4.2)$$

and the strain tensor can be reduced to the strain vector $\boldsymbol{\varepsilon}$,

$$\boldsymbol{\varepsilon} = \{\varepsilon_{xx} \varepsilon_{yy} \varepsilon_{xy}\}^T. \quad (4.3)$$

Solids can show different behaviors, depending on the solid material. Isotropic materials can be fully described by only two independent material properties, the Young modulus, E , and the Poisson ratio, ν . Thus, the relation between stress and strain in the solid domain is given by the constitutive equation, known as Hooke's Law:

$$\boldsymbol{\sigma} = \mathbf{c}\boldsymbol{\varepsilon} \quad (4.4)$$

in which, \mathbf{c} is the constitutive matrix, given by $\mathbf{c} = \mathbf{s}^{-1}$, being the matrix \mathbf{s} the compliance elasticity matrix. For a general orthotropic material case and considering a plane stress formulation, the matrix \mathbf{s} is given by

$$\mathbf{s}_{plane\ stress} = \begin{bmatrix} \frac{1}{E_{11}} & -\frac{\nu_{21}}{E_{22}} & 0 \\ -\frac{\nu_{12}}{E_{11}} & \frac{1}{E_{22}} & 0 \\ 0 & 0 & \frac{1}{G_{12}} \end{bmatrix} \quad (4.5)$$

while, when considering a plane strain formulation, matrix \mathbf{s} is given by:

$$\mathbf{s}_{plane\ strain} = \begin{bmatrix} \frac{1 - \nu_{31}\nu_{13}}{E_{11}} & -\frac{\nu_{12} + \nu_{31}\nu_{23}}{E_{22}} & 0 \\ -\frac{\nu_{12} + \nu_{32}\nu_{13}}{E_{11}} & \frac{1 - \nu_{32}\nu_{23}}{E_{22}} & 0 \\ 0 & 0 & \frac{1}{G_{12}} \end{bmatrix}, \quad (4.6)$$

being E_{ij} the elasticity modulus, ν_{ij} the material Poisson coefficient and G_{ij} the distortion modulus in material direction i and j .

Obtaining the constitutive matrix \mathbf{c} , it is possible to align it with a new material referential $Ox'y'$ defined by the versors $i = \{i'_x, i'_y\}$ and $j = \{j'_x, j'_y\}$, using the following expression:

$$\mathbf{c}' = \mathbf{T}^T \mathbf{c} \mathbf{T} \quad (4.7)$$

being \mathbf{T} the transformation matrix given by

$$\mathbf{T} = \begin{bmatrix} \cos^2 \alpha & \sin^2 \alpha & -\sin 2\alpha \\ \sin^2 \alpha & \cos^2 \alpha & \sin 2\alpha \\ \sin \alpha \cdot \cos \alpha & -\sin \alpha \cdot \cos \alpha & \cos^2 \alpha \cdot \sin^2 \alpha \end{bmatrix} \quad (4.8)$$

where the angle α is the angle between the original material axis Ox and the new material axis Ox' : $\alpha = \cos^{-1}(i, i')$.

Now, considering the displacement field given by $\mathbf{u} = \{u, v\}$, strain components are expressed as

$$\begin{aligned}\varepsilon_{xx} &= \frac{\partial u}{\partial x} \\ \varepsilon_{yy} &= \frac{\partial v}{\partial y} \\ \varepsilon_{xy} &= \frac{\partial u}{\partial y} + \frac{\partial v}{\partial x}\end{aligned}\tag{4.9}$$

Thus, the strain vector can be defined by the combination of a differential operator and the displacement field, \mathbf{u} ,

$$\boldsymbol{\varepsilon} = \mathbf{L}\mathbf{u}\tag{4.10}$$

where \mathbf{L} is given by

$$\mathbf{L} = \begin{bmatrix} \frac{\partial}{\partial x} & 0 & \frac{\partial}{\partial y} \\ 0 & \frac{\partial}{\partial y} & \frac{\partial}{\partial x} \end{bmatrix}^T.\tag{4.11}$$

4.2 - Weak Form

The strong form system equations are the partial differential system equations governing the studied physic phenomenon. Using this formulation, it is possible to obtain a numerical solution very close with the analytical solution. However this is usually an extremely difficult task in complex practical engineering problems.

On the other hand, formulations based on weak forms give a discretized system of equations but with a weaker consistency on the adopted approximation (or interpolation) functions. This formulation is able to produce stable algebraic system equations and more accurate results [74].

4.2.1 - Galerkin Weak Form

In this work, the discrete equation system is obtained using the Galerkin weak form, which is a variational method based on energy minimization.

So, considering a body described by the domain $\Omega \subset \mathbb{R}^2$ and bounded by Γ , where $\Gamma \in \Omega : \Gamma_u \cup \Gamma_t = \Gamma \wedge \Gamma_u \cap \Gamma_t = \emptyset$, being Γ_u the essential boundary and Γ_t the natural boundary, the equilibrium equations governing the linear elastostatic problem are defined as

$$\nabla \boldsymbol{\Lambda} + \mathbf{b} = 0\tag{4.12}$$

in which ∇ is the nabla operator, \mathbf{b} the body force per unit volume and $\boldsymbol{\Lambda}$ the Cauchy stress tensor, as defined previously. The natural boundary respect the condition $\boldsymbol{\Lambda}\mathbf{n} = \bar{\mathbf{t}}$ on Γ_t , being \mathbf{n} the unit outward normal to the boundary of domain Ω and $\bar{\mathbf{t}}$ the traction on the natural boundary Γ_t . The essential boundary condition is $\mathbf{u} = \bar{\mathbf{u}}$ on Γ_u , in which $\bar{\mathbf{u}}$ is the prescribed displacement on the essential boundary Γ_u .

According to the Galerkin Weak form, the real solution is the one that minimizes the Lagrangian functional, L , given by

$$L = T - U + W_f \quad (4.13)$$

being T the kinetic energy, U is the strain energy and W_f is the work produced by the external forces. The kinetic energy is defined by

$$T = \frac{1}{2} \int_{\Omega} \rho \dot{\mathbf{u}}^T \dot{\mathbf{u}} d\Omega \quad (4.14)$$

where the solid volume is defined by Ω , $\dot{\mathbf{u}}$ is the displacement first derivative with respect to time and ρ is the solid mass density. The strain energy, for elastic materials, is defined as

$$U = \frac{1}{2} \int_{\Omega} \boldsymbol{\varepsilon}^T \boldsymbol{\sigma} d\Omega \quad (4.15)$$

being $\boldsymbol{\varepsilon}$ the strain vector and $\boldsymbol{\sigma}$ the stress vector. The work produced by the external forces can be expressed as

$$W_f = \int_{\Omega} \mathbf{u}^T \mathbf{b} d\Omega + \int_{\Gamma_t} \mathbf{u}^T \bar{\mathbf{t}} d\Gamma \quad (4.16)$$

in which \mathbf{u} represents the displacement, \mathbf{b} the body forces and Γ_t the traction boundary where the external forces $\bar{\mathbf{t}}$ are applied. Therefore the Galerkin weak form can be represented as

$$L = \frac{1}{2} \int_{\Omega} \rho \dot{\mathbf{u}}^T \dot{\mathbf{u}} d\Omega - \frac{1}{2} \int_{\Omega} \boldsymbol{\varepsilon}^T \boldsymbol{\sigma} d\Omega + \int_{\Omega} \mathbf{u}^T \mathbf{b} d\Omega + \int_{\Gamma_t} \mathbf{u}^T \bar{\mathbf{t}} d\Gamma \quad (4.17)$$

and then minimized,

$$\delta \int_{t_1}^{t_2} \left[\frac{1}{2} \int_{\Omega} \rho \dot{\mathbf{u}}^T \dot{\mathbf{u}} d\Omega - \frac{1}{2} \int_{\Omega} \boldsymbol{\varepsilon}^T \boldsymbol{\sigma} d\Omega + \int_{\Omega} \mathbf{u}^T \mathbf{b} d\Omega + \int_{\Gamma_t} \mathbf{u}^T \bar{\mathbf{t}} d\Gamma \right] dt = 0. \quad (4.18)$$

Moving the variation operator δ inside the integrals,

$$\int_{t_1}^{t_2} \left[\frac{1}{2} \int_{\Omega} \delta(\rho \dot{\mathbf{u}}^T \dot{\mathbf{u}}) d\Omega - \frac{1}{2} \int_{\Omega} \delta(\boldsymbol{\varepsilon}^T \boldsymbol{\sigma}) d\Omega + \int_{\Omega} \delta \mathbf{u}^T \mathbf{b} d\Omega + \int_{\Gamma_t} \delta \mathbf{u}^T \bar{\mathbf{t}} d\Gamma \right] dt = 0. \quad (4.19)$$

The integrand function in the second integral term can be written as

$$\delta(\boldsymbol{\varepsilon}^T \boldsymbol{\sigma}) = \delta \boldsymbol{\varepsilon}^T \boldsymbol{\sigma} + \boldsymbol{\varepsilon}^T \delta \boldsymbol{\sigma} \quad (4.20)$$

in which $\boldsymbol{\varepsilon}^T \delta \boldsymbol{\sigma} = (\boldsymbol{\varepsilon}^T \delta \boldsymbol{\sigma})^T = \delta \boldsymbol{\sigma}^T \boldsymbol{\varepsilon}$. Using the constitutive Eq. (3.4) and the symmetric property of the material matrix, $\mathbf{c}^T = \mathbf{c}$, it is possible to write

$$\delta \boldsymbol{\sigma}^T \boldsymbol{\varepsilon} = \delta(\mathbf{c} \boldsymbol{\varepsilon})^T \boldsymbol{\varepsilon} = \delta \boldsymbol{\varepsilon}^T \mathbf{c}^T \boldsymbol{\varepsilon} = \delta \boldsymbol{\varepsilon}^T \mathbf{c} \boldsymbol{\varepsilon} = \delta \boldsymbol{\varepsilon}^T \boldsymbol{\sigma}. \quad (4.21)$$

Consequently, Eq. (4.20) becomes

$$(\boldsymbol{\varepsilon}^T \boldsymbol{\sigma}) = 2 \delta \boldsymbol{\varepsilon}^T \boldsymbol{\sigma}. \quad (4.22)$$

Retaking Eq. (4.19), it can be expressed as

$$-\rho \int_{\Omega} (\delta \rho \dot{\mathbf{u}}^T \dot{\mathbf{u}}) d\Omega - \int_{\Omega} \delta \boldsymbol{\varepsilon}^T \boldsymbol{\sigma} d\Omega + \int_{\Omega} \delta \mathbf{u}^T \mathbf{b} d\Omega + \int_{\Gamma_t} \delta \mathbf{u}^T \bar{\mathbf{t}} d\Gamma = 0. \quad (4.23)$$

Considering the stress-strain relation, $\boldsymbol{\sigma} = \mathbf{c}\boldsymbol{\varepsilon}$, and the strain-displacement relation, $\boldsymbol{\varepsilon} = \mathbf{L}\mathbf{u}$, Eq. (4.23) can be rearranged into the following expression:

$$\int_{\Omega} (\delta \mathbf{L}\mathbf{u})^T \mathbf{c}(\mathbf{L}\mathbf{u}) d\Omega - \int_{\Omega} \delta \mathbf{u}^T \mathbf{b} d\Omega - \int_{\Gamma_t} \delta \mathbf{u}^T \bar{\mathbf{t}} d\Gamma + \int_{\Omega} \rho(\delta \mathbf{u}^T \dot{\mathbf{u}}) d\Omega = 0, \quad (4.24)$$

which is the generic Galerkin weak form written in terms of displacement, very useful in solid mechanical problems. In static problems the fourth term of Eq. (4.24) disappears.

4.3 - Discrete Equation System

According to the principle of virtual work used in meshless methods, the discrete equations are obtained using meshless shape functions as trial and test functions. Thus, recalling Eq. (3.13), the virtual displacements, or the test functions, can be defined as

$$\delta u(x_i) = \delta \mathbf{u}_i = \mathbf{I} \begin{Bmatrix} \Phi_i \\ \Phi_i \end{Bmatrix} \delta \mathbf{u}_s = \begin{bmatrix} \varphi_1(x_i) & 0 & \dots & \varphi_n(x_i) & 0 \\ 0 & \varphi_1(x_i) & \dots & 0 & \varphi_n(x_i) \end{bmatrix} \begin{Bmatrix} \delta u_1 \\ \delta v_1 \\ \vdots \\ \delta u_n \\ \delta v_n \end{Bmatrix} = \mathbf{H}_i \delta \mathbf{u}_s \quad (4.25)$$

being \mathbf{I} a 2×2 identity matrix and $\mathbf{u}_i = \{u_i, v_i\}$, having two degrees of freedom, since it is being considered a 2D problem.

Therefore, the virtual work of the first term of Eq. (4.24),

$$\begin{aligned} \int_{\Omega} (\delta \mathbf{L}\mathbf{u})^T \mathbf{c}(\mathbf{L}\mathbf{u}) d\Omega &= \int_{\Omega} (\mathbf{L}\mathbf{H}_i \delta \mathbf{u}_s)^T \mathbf{c}(\mathbf{L}\mathbf{H}_i \mathbf{u}_s) d\Omega = \int_{\Omega} \delta \mathbf{u}_s^T \mathbf{B}_i^T \mathbf{c} \mathbf{B}_i \mathbf{u}_s d\Omega \\ &= \delta \mathbf{u}_s^T \int_{\Omega} \mathbf{B}_i^T \mathbf{c} \mathbf{B}_i d\Omega \mathbf{u}_s \end{aligned} \quad (4.26)$$

in which the deformability matrix \mathbf{B}_i for the n nodes constituting the influence-cell of interest point x_i , can be defined as

$$\mathbf{B}_i = \begin{bmatrix} \frac{\partial \varphi_1(x_i)}{\partial x} & 0 & \vdots & \frac{\partial \varphi_2(x_i)}{\partial x} & 0 & \vdots & \vdots & \frac{\partial \varphi_n(x_i)}{\partial x} & 0 \\ 0 & \frac{\partial \varphi_1(x_i)}{\partial y} & \vdots & 0 & \frac{\partial \varphi_2(x_i)}{\partial y} & \vdots & \dots & 0 & \frac{\partial \varphi_n(x_i)}{\partial y} \\ \frac{\partial \varphi_1(x_i)}{\partial y} & \frac{\partial \varphi_1(x_i)}{\partial x} & \vdots & \frac{\partial \varphi_2(x_i)}{\partial y} & \frac{\partial \varphi_2(x_i)}{\partial x} & \vdots & \vdots & \frac{\partial \varphi_n(x_i)}{\partial y} & \frac{\partial \varphi_n(x_i)}{\partial x} \end{bmatrix}. \quad (4.27)$$

In an analogous way, remaining terms of Eq. (4.24) can be also simplified, obtaining the following:

$$\int_{\Omega} \delta \mathbf{u}^T \mathbf{b} d\Omega = \int_{\Omega} (\mathbf{H}_i \delta \mathbf{u}_s)^T \mathbf{b} d\Omega = \delta \mathbf{u}_s^T \int_{\Omega} \mathbf{H}_i^T \mathbf{b} d\Omega; \quad (4.28)$$

$$\int_{\Gamma_t} \delta \mathbf{u}^T \bar{\mathbf{t}} d\Gamma = \int_{\Gamma_t} (\mathbf{H}_i \delta \mathbf{u}_s)^T \bar{\mathbf{t}} d\Gamma = \delta \mathbf{u}_s^T \int_{\Gamma_t} \mathbf{H}_i^T \bar{\mathbf{t}} d\Gamma; \quad (4.29)$$

$$\int_{\Omega} \rho(\delta \mathbf{u}^T \ddot{\mathbf{u}}) d\Omega = \delta \mathbf{u}_s^T \int_{\Omega} \mathbf{H}_I^T \rho \mathbf{H}_I d\Omega \ddot{\mathbf{u}}_s \quad (4.30)$$

Thus, Eq. (4.24) can become the following

$$\begin{aligned} \delta L = & \delta \mathbf{u}_s^T \underbrace{\int_{\Omega} \mathbf{B}_I^T \mathbf{c} \mathbf{B}_I d\Omega}_{\mathbf{K}} \mathbf{u}_s - \delta \mathbf{u}_s^T \underbrace{\int_{\Omega} \mathbf{H}_I^T \mathbf{b} d\Omega}_{\mathbf{f}_b} - \delta \mathbf{u}_s^T \underbrace{\int_{\Gamma_t} \mathbf{H}_I^T \bar{\mathbf{t}} d\Gamma}_{\mathbf{f}_t} + \\ & + \delta \mathbf{u}_s^T \underbrace{\int_{\Omega} \mathbf{H}_I^T \rho \mathbf{H}_I d\Omega}_{\mathbf{M}} \ddot{\mathbf{u}}_s = 0 \end{aligned} \quad (4.31)$$

The equilibrium equation is then obtained and defined as

$$\mathbf{K} \mathbf{u} + \mathbf{M} \ddot{\mathbf{u}} = \mathbf{f}_b + \mathbf{f}_t, \quad (4.32)$$

being \mathbf{K} , the stiffness matrix, \mathbf{u} , the displacement field, \mathbf{M} , the mass matrix, \mathbf{f}_b , the body weight vector and \mathbf{f}_t , the external forces vector. So, considering the vector $\mathbf{f} = \mathbf{f}_b + \mathbf{f}_t$ as the sum vector of the forces applied, it is possible to, using Eq. (4.32), obtain the displacement field \mathbf{u} .

Thenceforward, it is possible to determine numerous variable fields. The strain $\boldsymbol{\varepsilon}(\mathbf{x}_I)$, in an interest point $\mathbf{x}_I \in \Omega$ can be obtained using Eq. (4.10). Then, using the Hooke's Law present in Eq. (4.4), the stress field, $\boldsymbol{\sigma}(\mathbf{x}_I)$ can be also obtained.

Considering both the strain and the stress fields, the Strain Energy Density (SED) field for an interest point \mathbf{x}_I and a specific load case can be determined as

$$\mathbf{U}(\mathbf{x}_I) = \frac{1}{2} \int_{\Omega_I} \boldsymbol{\sigma}(\mathbf{x}_I)^T \boldsymbol{\varepsilon}(\mathbf{x}_I) d\Omega_I. \quad (4.33)$$

The principal stresses $\sigma(\mathbf{x}_I)$ for the interest point \mathbf{x}_I are obtained from the Cauchy stress tensor $\boldsymbol{\Lambda}(\mathbf{x}_I)$ using the expression

$$\det \left(\begin{bmatrix} \sigma_{xx}(\mathbf{x}_I) & \sigma_{xy}(\mathbf{x}_I) \\ \sigma_{xy}(\mathbf{x}_I) & \sigma_{yy}(\mathbf{x}_I) \end{bmatrix} - \sigma(\mathbf{x}_I)_i \begin{bmatrix} 1 & 0 \\ 0 & 1 \end{bmatrix} \right) = 0 \quad (4.34)$$

and the principal directions $\mathbf{n}((\mathbf{x}_I)_i) = \{n_x((\mathbf{x}_I)_i), n_y((\mathbf{x}_I)_i)\}^T$ are obtained with

$$\left(\begin{bmatrix} \sigma_{xx}(\mathbf{x}_I) & \sigma_{xy}(\mathbf{x}_I) \\ \sigma_{xy}(\mathbf{x}_I) & \sigma_{yy}(\mathbf{x}_I) \end{bmatrix} - \sigma(\mathbf{x}_I)_i \begin{bmatrix} 1 & 0 \\ 0 & 1 \end{bmatrix} \right) \begin{Bmatrix} n_x(\mathbf{x}_I)_i \\ n_y(\mathbf{x}_I)_i \end{Bmatrix} = 0 \quad (4.35)$$

The three principal stresses obtained can be used to determine the von Mises effective stress for each interest point \mathbf{x}_I with the following expression

$$\sigma_{eq}(\mathbf{x}_I) = \sqrt{\frac{1}{2} ((\sigma(\mathbf{x}_I)_1 - \sigma(\mathbf{x}_I)_2)^2 + (\sigma(\mathbf{x}_I)_2 - \sigma(\mathbf{x}_I)_3)^2 + (\sigma(\mathbf{x}_I)_3 - \sigma(\mathbf{x}_I)_1)^2)}. \quad (4.36)$$

The von Mises equivalent effective strain can be obtain in similar way:

$$\varepsilon_{eq} = \frac{2}{3} \sqrt{\frac{3(e_{xx}^2 + e_{yy}^2 + e_{zz}^2)}{2} + \frac{3(\gamma_{xy}^2 + \gamma_{yz}^2 + \gamma_{zx}^2)}{4}}. \quad (4.37)$$

With the deviatoric strains:

$$\begin{aligned} e_{xx} &= +\frac{2}{3}\varepsilon_{xx} - \frac{1}{3}\varepsilon_{yy} - \frac{1}{3}\varepsilon_{zz}; \\ e_{yy} &= -\frac{1}{3}\varepsilon_{xx} + \frac{2}{3}\varepsilon_{yy} - \frac{1}{3}\varepsilon_{zz}; \\ e_{zz} &= -\frac{1}{3}\varepsilon_{xx} - \frac{1}{3}\varepsilon_{yy} + \frac{2}{3}\varepsilon_{zz}. \end{aligned} \quad (4.38)$$

The engineering strains γ are defined as:

$$\gamma_{ij} = 2 \times \varepsilon_{ij}. \quad (4.39)$$

4.3.1 - Dynamic Equations

The equilibrium equations governing the linear dynamic response can be represented as in Eq. (4.32). The fundamental mathematical method used to solve Eq. (4.32) is the separation of variables. In order to change the equilibrium equations to the modal generalized displacements [59] was performed the following transformation:

$$\mathbf{u}(t) = \mathbf{\Phi} \mathbf{x}(t) \quad (4.40)$$

where $\mathbf{\Phi}$ is a $m \times m$ square matrix containing m spatial vectors independent of the time variable t , $\mathbf{x}(t)$ is a time dependent vector and $m = 2N$ for the 2D case and $m = 3N$ for the 3D case, being N the total number of nodes in the problem domain. From Eq. (4.40) also follows that $\dot{\mathbf{u}}(t) = \mathbf{\Phi} \dot{\mathbf{x}}(t)$ and $\ddot{\mathbf{u}}(t) = \mathbf{\Phi} \ddot{\mathbf{x}}(t)$. The components of $\mathbf{u}(t)$ are called generalized displacements. For which the solution can be presented in the form,

$$\mathbf{u}(t) = \mathbf{\phi} \sin(\omega(t - t_0)) \quad (4.41)$$

Being $\mathbf{\phi}$ the vector of order m , t the time variable, the constant initial time is defined by t_0 and ω is the vibration frequency vector. Substituting Eq. (4.41) into (4.32) the generalized eigenproblem is obtain, from which $\mathbf{\phi}$ and ω must be determined,

$$\mathbf{K}\mathbf{\phi} = \omega^2 \mathbf{M}\mathbf{\phi}. \quad (4.42)$$

Eq. (4.42) yields the m eigensolutions:

$$\begin{cases} \mathbf{K}\mathbf{\phi}_1 = \omega_1^2 \mathbf{M}\mathbf{\phi}_1 \\ \mathbf{K}\mathbf{\phi}_2 = \omega_2^2 \mathbf{M}\mathbf{\phi}_2 \\ \vdots \\ \mathbf{K}\mathbf{\phi}_m = \omega_m^2 \mathbf{M}\mathbf{\phi}_m \end{cases}. \quad (4.43)$$

The vector ϕ_i is called the i th mode shape vector and ω_i is the corresponding frequency of vibration. Defining a matrix Φ whose columns are the eigenvectors ϕ_i ,

$$\Phi = [\phi_1 \phi_2 \dots \phi_m] \quad (4.44)$$

and a diagonal matrix Ω which stores the eigenvalues ω_i ,

$$\Omega = \begin{bmatrix} \omega_1^2 & 0 & \dots & 0 \\ 0 & \omega_2^2 & \dots & 0 \\ \vdots & \vdots & \ddots & \vdots \\ 0 & 0 & \dots & \omega_m^2 \end{bmatrix}; \quad (4.45)$$

the m solutions can be written as:

$$K \Phi = M \Phi \Omega . \quad (4.46)$$

It is required that the space functions satisfy the following stiffness and mass orthogonality conditions:

$$\Phi^T K \Phi = \Omega \quad (4.47)$$

and

$$\Phi^T M \Phi = I . \quad (4.48)$$

After substituting Eq. (4.40) and its time derivatives into Eq. (4.32) and pre-multiplying by Φ^T , the equilibrium equation that corresponds to the modal generalized displacement is obtained:

$$\ddot{x}(t) + \Omega x(t) = \Phi^T F(t). \quad (4.49)$$

The initial conditions on $x(t)$ are obtained using Eq. (4.40) and considering the M-orthonormality of Φ^T at time $t = 0$,

$$\begin{cases} x_0 = \Phi^T M u_0 \\ \dot{x}_0 = \Phi^T M \dot{u}_0 \end{cases} \quad (4.50)$$

Equation (4.49) can be represented as m individual equations of the form

$$\begin{cases} \ddot{x}_i(t) + \omega_i^2 x_i(t) = f_i(t) \\ f_i(t) = \phi_i^T F(t) \end{cases} \quad (4.51)$$

with the initial conditions:

$$\begin{cases} x_i^{t=0} = \phi_i^T M u_0 \\ \dot{x}_i^{t=0} = \phi_i^T M \dot{u}_0 \end{cases} \quad (4.52)$$

For the complete response, the solution to all m equations in Eq. (4.51) must be calculated and then the nodal point displacement are obtained by superposition of the response in each mode:

$$\mathbf{u}(t) = \sum_{i=1}^m \Phi_i \mathbf{x}_i(t). \quad (4.53)$$

Therefore the response analysis requires, first, the solution of the eigenvalues and eigenvectors of the problem, Eq. (4.42), then the solution of the decoupled equilibrium equations in Eq. (4.51) and, finally, the superposition of the response in each eigenvector as expressed in Eq. (4.53).

4.3.2 - Results Parameterization

Knowing that tensile stress (σ) and strain (ε) are correlated by the Young modulus (E),

$$\sigma = E \varepsilon, \quad (4.54)$$

is possible to parameterize the results by a parameter α and then :

$$\sigma = \alpha E \varepsilon. \quad (4.55)$$

This kind of parameterization is useful for example to obtain a “virtual” displacement or stress distribution field for each vibrational mode that is proportional to its vibration frequency. Thus, recalling Eq. (4.40) is possible to write:

$$\mathbf{u}_i(t) = \omega_i \Phi_i \mathbf{x}_i(t). \quad (4.56)$$

From Eq. (4.10) , the strain vector can be redefined as

$$\varepsilon_i = \omega_i \mathbf{L} \Phi_i \mathbf{x}_i(t) \quad (4.57)$$

and for consequence,

$$\sigma_i = \mathbf{c} \varepsilon_i = \omega_i \mathbf{c} \mathbf{L} \Phi_i \mathbf{x}_i(t). \quad (4.58)$$

Chapter 5

The Modelling Process

Finite element modelling generally involves four stages [93]. When first applied to biomechanics, it involved five stages. A first stage was necessary to develop special coding in order to address the specific computational problem. Better performing procedures are still under development, such as the isogeometric analysis concept [94], but nowadays many of the necessary features are already incorporated into the major program packages available on the market (e.g., ABAQUS, ANSYS, NASTRAN, MARC, ADINA, COMSOL, CASTEM, and LUSAS). However, many established research groups in the computational mechanics community have developed their own research codes for advanced problems that are not adequately covered by the above general purpose codes. Examples are the isogeometric analysis code [94], [95], COMES-GEO [96], Pandas [97], Swandyne [98] and FEMAS [99], which was used during this project and is addressed in Sec. 5.3 - . These allow advances in computational biomechanics to push even further.

The aforementioned first phase is now known as *preprocessing* and involves defining the mesh geometry, specifying the material property distributions, and designating the loading conditions. During the second phase, the computation of solution is carried out (this phase involves the choice of numerical algorithm and choice of convergence criteria). The third phase is generally known as *postprocessing* and it includes the extraction of meaningful parameters and variables of interest from the simulation. The last phase is represented by the validation procedure and the interpretation of the results.

Validation of the models entails that models should be verified and validated by means of combining computational and experimental protocols [93].

5.1 - Geometry

Regarding geometry, we should differentiate the case of 3D and 2D models. 2D models are generally adopted when the object of interest can be modeled considering approximately both geometrical and material symmetry about a single axis (axisymmetric simplification) [93], in the case of 2D plane stress simulations (e.g., influence of surrounding tissues on biomechanics of the aortic wall [100]). 2D simulation is also often used as a preliminary stage of development

of a 3D computational model. Otherwise, nowadays 3D models are the state of the art of FEA in biomechanics applications.

In order to define the model's geometry of living subjects organs, digital images are generally preferred as obtained by CT and MRI. The latter is favored as it represents an accurate and noninvasive method. MRI is used to develop subject-specific biomechanical models, either of normal or of pathologic subjects.

Obviously, subject-specific digitized images are always preferable for purposes of accuracy in the reconstruction of biological geometries. When possible, the finite element mesh can be coupled with the source geometry for simplifying result interpretation. Nowadays, several software packages have been developed for image segmentation purposes. Some can directly generate the mesh to run the finite element model simulation, some others may be used to segment tissue geometry automatically and to provide the surface STL format (which is a computer-aided design format) to be imported either into a mesh generator specific software or into the software for running the complete finite element simulation. The image segmentation procedure is one of the most time-consuming procedures within the finite element model analysis [93].

Despite the many advantages of using images and segmentation procedures to obtain the model's geometry, in many problems it is impossible to use such methodology, either because of technical difficulties or impossibilities (for example by contraindications of medical imaging techniques), associated costs or even the absence of appropriate targeting segmentation methods. Therefore, there are alternative software that allow to build the geometric surface of the model based on drawing tools. The quality and approximation of the model to the real problem will be as better as the expertise and knowledge of these tools by the researcher but is also dependent on the flexibility and capabilities of the used software. It should be taken into consideration the choice of the most suitable program. Some of the available systems are: Solidworks, Onshape, Rhino3D, CATIA and Autodesk.

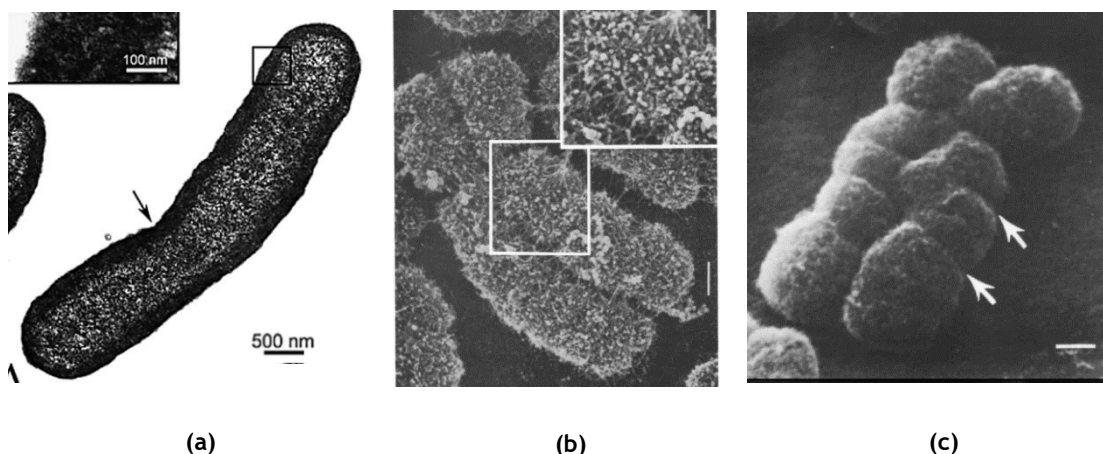


Figure 5.1 - Microscopic images of human metaphase chromosomes: (a) chromosome number 2 from normal lymphocytes observed by transmission electron microscopy (TEM) [101]; (b) G-banded human chromosome 10 by scanning electron microscopy (SEM), Bar = $0,5 \mu m$ [102]; (c) Uncoated, G-banded human chromosome 12, viewed at 45° tilt in Cambridge S4-10 electron microscope, Bar = $0,5 \mu m$ [102].

The obtaining of the geometry of a chromosome can be supported in microscopic images (Figure 5.1 presents the 3 images of human chromosomes, used as references to construct both 2D and 3D models used in this work). However, there are no available solutions for the

automatic obtaining of its geometry, reason why in this work it will be used a mesh generator commercial code software.

To obtain the geometry of the chromosomes with reference to the images of Figure 5.1, there are two steps to the construction of the two-dimensional and three-dimensional models that is common to both. In the first place, it is necessary to mark a set of points that define the outer limits of the chromosome. In Figure 5.2 (a) the points that define chromosome number 2 (Figure 5.1 (a)) are shown. After defining the set of points is necessary to introduce a scaling transformation in order to obtain the points in real coordinates. The scaling factor (s_f) (equal in all directions) is calculated using the scale mentioned in the original figure (s_i) and the actual length of the scale bar (l), therefore, it is given by: $s_f = \frac{s_i}{l}$.

For a 2D model the following steps were performed:

- Use of the defined points (Figure 5.2 (a)) to construct a closed spline that delimitates de chromosome and can describe a surface domain (Figure 5.2 (b));
- Definition of number of nodes along the curve or minimal distance between them;
- Using the nodes in the boundary as a reference/pattern, the nodes that discretizes the total problem domain are defined and is possible to elaborate a mesh to be used by FEM (Figure 5.2 (c)).

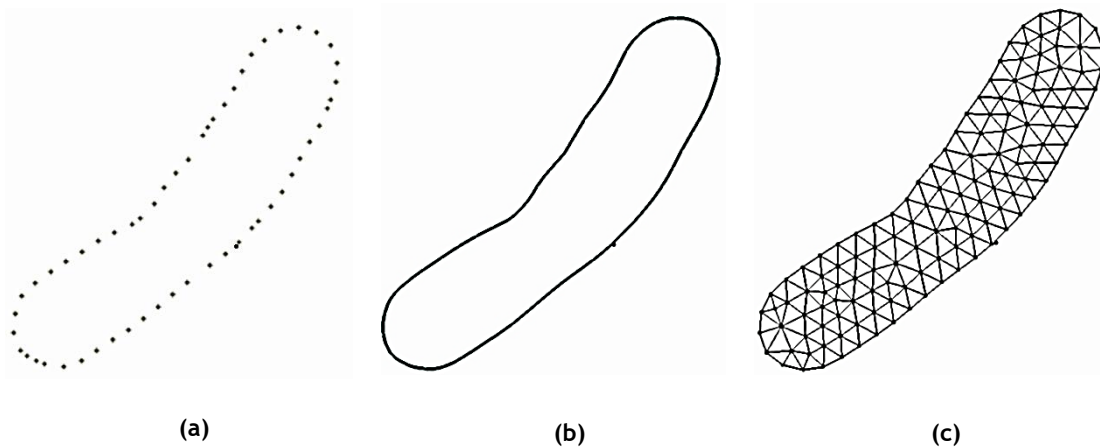


Figure 5.2 - 2D models development process.

Obtaining a three-dimensional model from a two-dimensional figure requires more intermediate steps and the making of some assumptions. Thus, the chromosomes were considered similar to cylindrical tubular structures with inconstant radius along with its length. After obtain the curve that best describes the 2D geometry, the next steps are:

- Draw circles in a perpendicular plane to the one where the boundary curve is so that it crosses opposite points belonging to the curve; These circles should preferably be equally spaced describing the curvature of the chromosome; To draw each one of the circles it is necessary to define the plane to which it belongs to; In Figure 5.3 (a) it is possible to observe the boundary curve, the global axis system, 2 circumferences and the drawing plane of one of them;
- By drawing the circumferences one by one, it is possible at the end to already visualize the final shape of the three-dimensional model as shown in the Figure 5.3 (b);
- Using the circumferences the next step is to build a boundary surface that delimitates de tridimensional solid, Figure 5.3 (c);

- As occurred in 2D case, the discretization starts with defining the number of nodes along the curves that describes the surface;
- The nodes along the curves are used as reference to define the nodes in all surface (Figure 5.3 (c)) and by its turn, the nodes inside are defined by correspondence with surface nodes; In Figure 5.3 (d) is presented one model of chromosome number 2 with some cross-sectional cuts to visualize interior nodes and it is also represented the mesh to be used for FEM simulation.

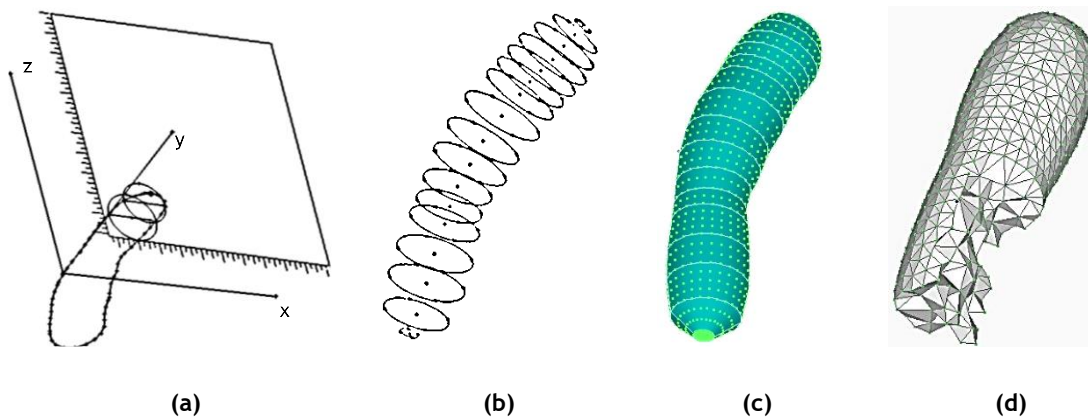


Figure 5.3 - 3D models development process.

5.2 - Mesh Definition

The next step after the construction of the object geometry is to convert the object into a mesh with a smooth surface/outlines that is as close as possible to the actual domain [93]. The accurate surface definition of an object depends heavily on the segmentation algorithm/methodology used, while the mesh quality influences the quality of the FEA. The spatial discretization should be of the right size, quality, and shape for obtaining an accurate solution [103]. For traditional engineering applications in which object boundaries may be described, analytically or piecewise analytically powerful mesh generating methods exist [104], [105].

In order to generate the chromosome mesh it was used the same software used to create its geometry. This software allows to receive or export the information regarding its geometry in STL format. In 3D models it was necessary to use another software, the AUTODESK Meshmixer (freeware), in order to smooth the surface. The geometry hand-created had sharp edges on the poles and in chromosomes number 10 and 12, where is distinguishable the two chromatids, the region between them was not well defined.

5.3 - Finite Element Meshless Method Analysis Software - FEMAS

FEMAS is a meshless computational framework developed at FEUP since 2014 by Prof. Jorge Belinha. It is an original code implemented in the commercial software MATLAB that uses the formulations presented in Chapter 3 and Chapter 4. Through a graphical user interface (GUI),

Figure 5.4, this software allows an easy construction of numerical models and their analysis using several different discretization techniques.

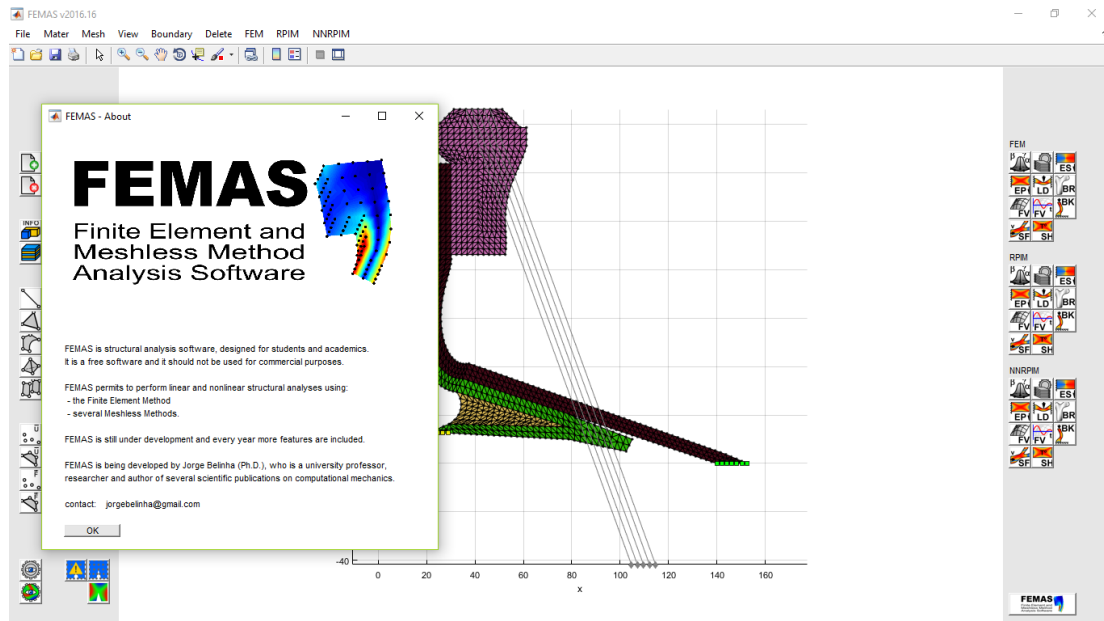


Figure 5.4 - FEMAS Graphical User Interface.

In terms of numerical analysis, FEMAS allows the use of FEM, RPIM and NNRPIM and currently allows the following analysis:

- Linear Static Linear-Elastic;
- Non-Linear Elasto-Plastic;
- Non-Linear Large Deformations;
- Crack opening path;
- Free Vibration;
- Forced Vibration;
- Buckling;
- Static Fluid flow.

This framework is capable of performing simulations with isotropic and anisotropic materials, as well as, making analysis both in 3D and 2D settings, using for this the classical tridimensional deformation theory and the plane stress and plane strain two-dimensional deformation theory, respectively. FEMAS allows for the autonomous construction of the numerical models, allowing the user to control the nodal discretization, material disposition and location of essential and boundary conditions. All these tasks can be performed directly in the software without the need to use any external CAD software. Nonetheless, meshes can also be created using other CAD software and imported into FEMAS. Moreover, FEMAS allows to present the displacement, stress and strain fields along with the solid domain using both figures and arrays, which permits further data analyses.

All the examples and simulations shown in this work were made using the aforementioned software and were used the parameters mentioned in Table 5.1 and Table 5.2 in all RPIM and NNRPIM analysis.

Table 5.1 - RPIM Parameters

| RPIM | |
|---|--|
| 2D | 3D |
| Nodes in the influence-domain: 27 | Nodes in the influence-domain: 27 |
| $c = 1,42$ | $c = 1,42$ |
| $p = 1,03$ | $p = 1,03$ |
| Polynomial Basis: Constant | Polynomial Basis: Constant |
| Integration points: 1 per triangle | Integration points: 1 per tetrahedron |

Table 5.2 - NNRPIM Parameters

| NNRPIM | |
|---|---|
| 2D | 3D |
| Influence-cell: Second Order | Influence-cell: Second Order |
| $c = 0,0001$ | $c = 0,0001$ |
| $p = 0,999$ | $p = 0,999$ |
| Polynomial Basis: Constant | Polynomial Basis: Constant |
| Integration points: 1 per sub-cell | Integration points: 1 per sub-cell |

Chapter 6

Preliminary Studies

Before analyzing 2D and 3D models of human chromosomes, several preliminary studies were made. The first objective of these studies was to analyze the convergence of the RPIM and the NNRPIM when compared with FEM and to define the level of discretization needed in order to obtain the most accurate results. The second objective was to establish the mechanical properties for chromosomes from experimental data present in the literature (Sec. 2.2 -) and afterwards validate the accuracy of our simulations of this material.

The evolution of the processing power of computers has allowed the growth of the three-dimensional analysis and, therefore, more accurate analyses. However, there are still limitations, regarding the level of discretization, 3D analysis represent higher computational costs. In this way, 2D simulations continue to be useful. Thus, another objective is to try to understand if it is possible to improve 2D models and to approximate results.

6.1 - Model

To carry out these preliminary tests and to meet the objectives outlined above, a model of an artificial chromosome was developed, with a simulated geometry but as close as possible to the dimensions of the human chromosome number 2. In Figure 6.1 a scheme of the dimensions of the two-dimensional model is presented.

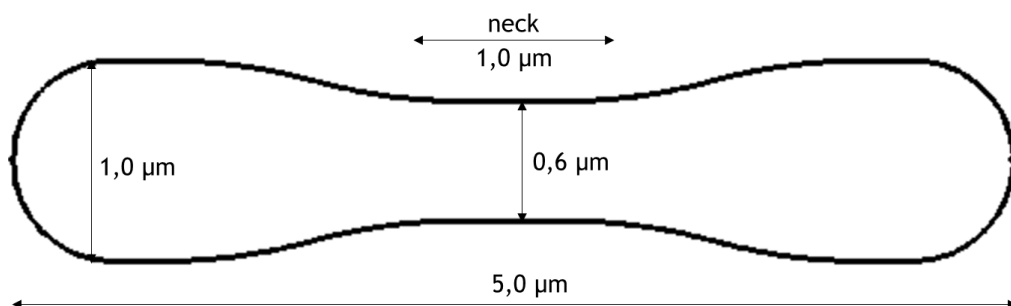


Figure 6.1 - Artificial chromosome 2D model dimentions.

The mechanical properties described in Sec. 2.2 - were obtained experimentally by strain-stress tests and all simulations of this procedure follow the essential and boundary conditions described in Figure 6.2 (a). The total force $\|\vec{F}\| = 300 \text{ pN}$. In addition, it is intended to perform a dynamic analysis and therefore it is also evaluated the first three modes of free vibrations. In this case, no forces are applied and, given the geometry of the problem, only the displacement, in all directions, of the most central point is restricted, as exemplified in Figure 6.2 (b). This condition attempts to simulate the effect of the centromere.

In order to take a first step also in the simulation of the cell division, more concretely in the processes that occur at the level of the nucleus during the division of the chromosomes, a bending test was also performed applying the essential and natural boundary conditions identified in the Figure 6.2 (c). On this case, it is applied a total force $\|\vec{F}\| = 7 \times 10^{-10} \text{ N}$ to simulate the mitotic spindle force. The applied force is localized in the central and thicker region in order to simulate a spindle-fiber attachment of median type (Figure 2.5).

For 3D cases it was used the same principles above described.

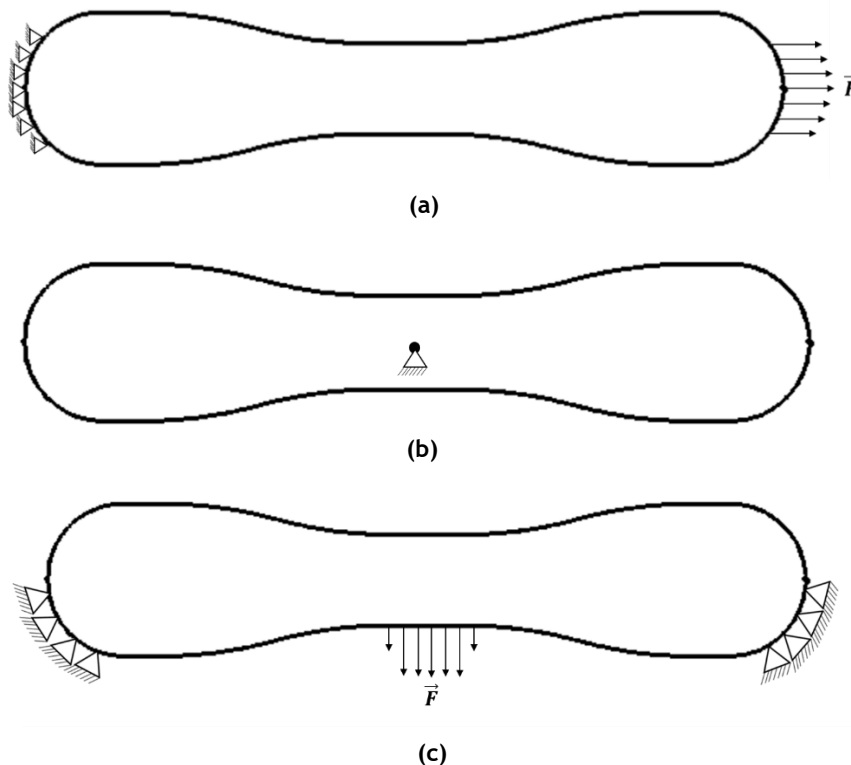


Figure 6.2 - Models for 2D preliminary studies: (a) stress-strain curve, (b) free vibrations and (c) bending simulations.

6.2 - Nodal Discretization Convergence Study

One of the aspects that can most influence the results when using this type of methods is the number and location of the nodes that describe the problem. In this way, the problem was analyzed with 6 two-dimensional models with increasing number of nodes. In all cases was considered a constant thickness of $1,0 \mu\text{m}$. It should be noted that in view of the processing requirements of the used software and the available hardware, no models with more than 2000 nodes were developed. In all the analyses, the nodes location were coincident for both FEM

and meshless methods (the meshes are the same for both FEM and meshless formulations). The nodal distribution in each model can be seen in Figure 6.3 and it should be noticed that even with a simple geometry with two axes of symmetry, in most of the models, it was not obtained an equally symmetric nodal distribution. This fact may, from the outset, influence the results.

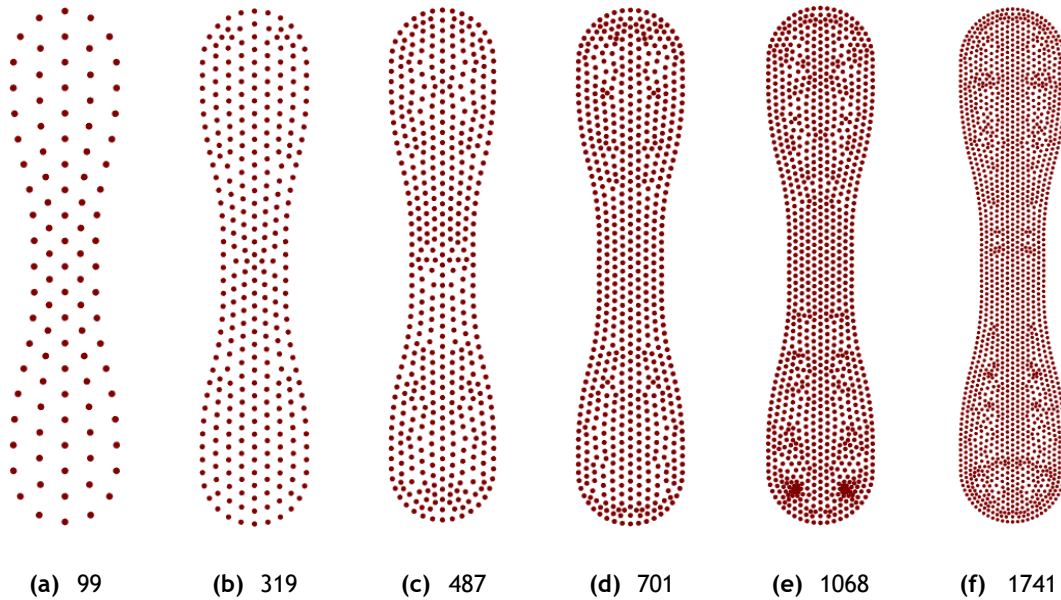


Figure 6.3 - Models with increasing number of nodes for discretization convergence study.

6.2.1 - Stress-strain experiment simulation

The Cauchy strain or engineering strain is expressed as the ratio of total deformation to the initial dimension of the material body in which the forces are being applied. The engineering normal strain of a material line element or fiber axially loaded is expressed as the change in length ΔL per unit of the original length L of the line element or fibers. The normal strain is positive if the material fibers are stretched and negative if they are compressed. Thus:

$$e = \frac{\Delta L}{L} = \frac{l - L}{L}. \quad (6.1)$$

Therefore, is calculated the Cauchy linear strain between two points located in the opposite extremities of the chromosome. As the artificial chromosome was loaded with $300 pN$, corresponding to the doubling force, according to the literature, it is expected a $e \approx 1$ because is expected the final chromosome length to be twice the initial length. In Figure 6.4 is presented the linear Cauchy strain obtained for an increasing number of nodes that discretizes the problem domain and for the three numerical method tested. In all simulations, it was obtained results very approximated to the expected, nevertheless is possible to observe that the results tended to stabilize for more than 487 nodes and for 1068 and more nodes the differences between FEM and NNRPIM results are negligible. Although the RPIM results always remained a bit higher, the differences are not so considerable.

Attending on Table 6.1, Table 6.2 and Table 6.3, where are presented the color maps for displacement, von Mises effective stress and equivalent effective strain fields, it is observable that meshless methods always produced smother results comparatively with FEM. It is also

possible to observe from Table 6.2 and Table 6.3 that the narrower central zone of the chromosome, coinciding with the centromere, is the one that shows a higher stress concentration of tensions and experiences the higher displacement. The linear deformation of Cauchy was also evaluated in this region, shown in Figure 6.5, and the convergence is fast and for models with more than 701 nodes there is no significant fluctuation of results.

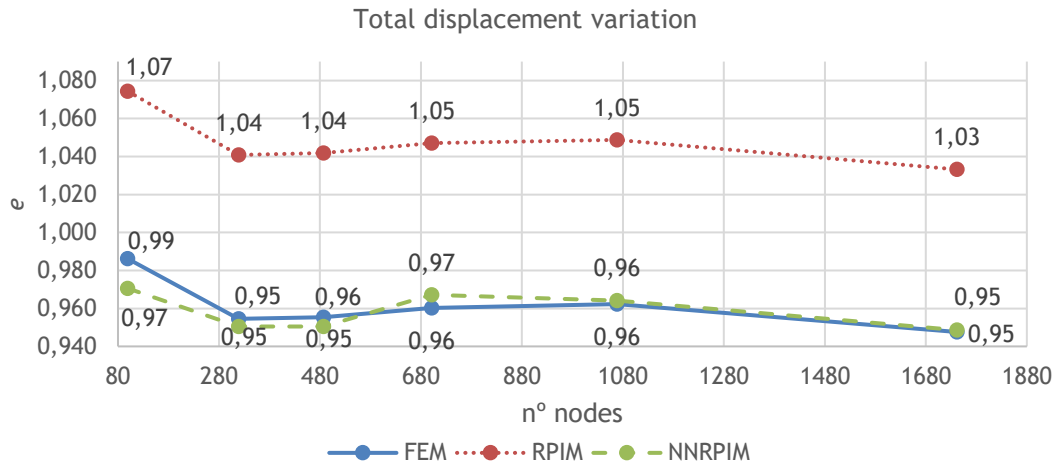


Figure 6.4 - Total displacement variation with increasing number of nodes and per numerical method.

Is possible to obtain the local equivalent stress (σ_{eq}) by

$$\sigma_{eq} = \frac{\|\vec{F}\|}{A_{eq}}, \tag{6.2}$$

where $\|\vec{F}\|$ is the total applied force intensity and A_{eq} is the cross-section area to be analyzed. Then, through Eq. (4.54), is possible to locally study the equivalent Young modulus using:

$$E_{eq} = \frac{\sigma_{eq}}{e}. \tag{6.3}$$

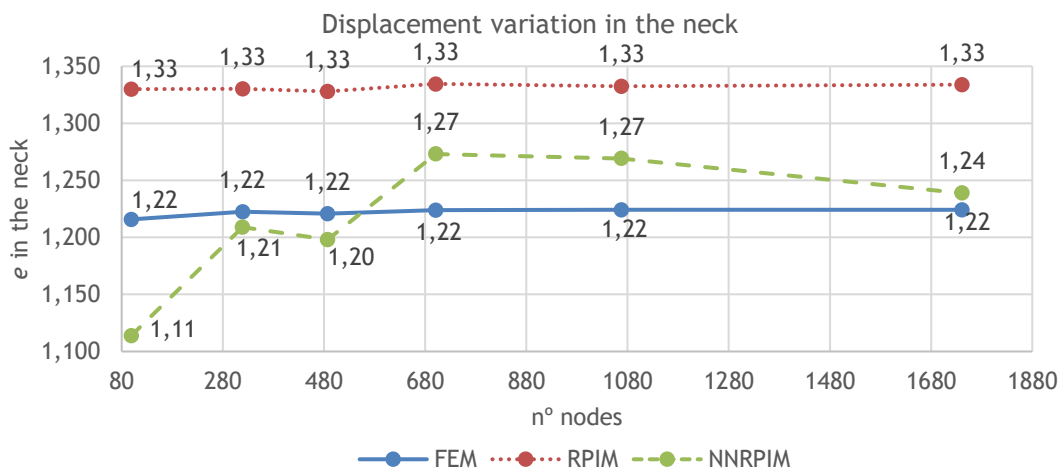


Figure 6.5 - Displacement in the neck region variation with increasing number of nodes and per numerical method.

Considering this approach of the problem, in Figure 6.6 are presented the results for the neck region and it was verified that in all the simulations, except for the RPIM, the equivalent Young modulus approximates the value defined in the literature ($400 Pa$, see Sec. 2.2 -) with a margin error lower than that indicated by the authors ($20 Pa$, see Sec. 2.2 -).

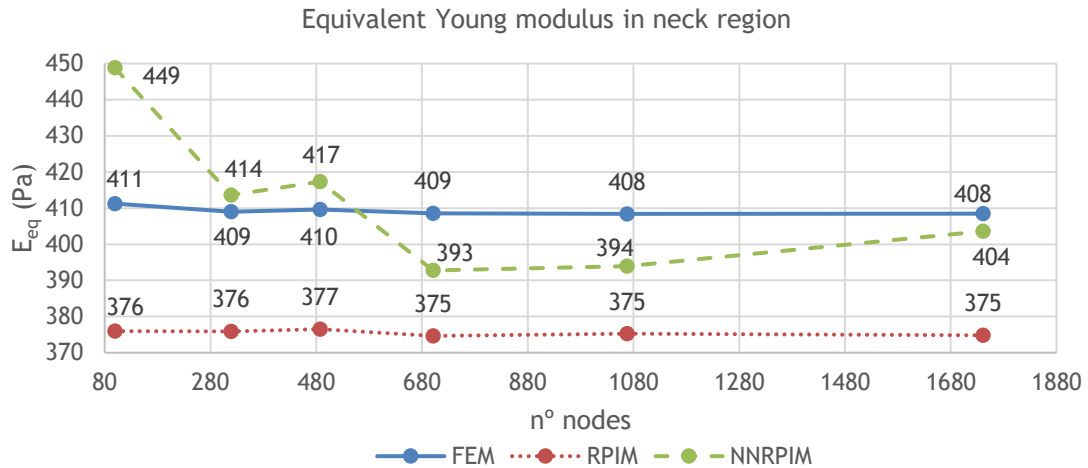


Figure 6.6 - Equivalent Young modulus in the neck region variation with increasing number of nodes and per numerical method.

By verifying all the data obtained we arrive at several conclusions:

- It is possible to say that the results will be so much more exact and close between different methods as greater the level of discretization is, that is to say, the more nodes are used to define the problem under study;
- However, from about 1068 nodes there is no great improvement / alteration of results and as the computational costs increase with the increase in the number of nodes, it is sufficient to use chromosome models with a number of nodes between 1100 and 2000;
- NNRPIM is the one that presents final results closer to those obtained using FEM even though the convergence process is not linear.
- The obtained results are in accordance with what was expected and then is possible to conclude that the utilized numerical methods can be applied to the simulation and *in silico* study of these microstructures;
- Observing again Table 6.2 and Table 6.3, it is verified the existence of four small areas where stresses accumulate and where higher deformations occur. These small regions match with the transitional sites between nodes where essential and boundary conditions are applied and those that remain unconstrained and unloaded. However, the accumulation of tensions and deformations is due to this abrupt breakdown of constraints, introducing artifacts in the results and leading to the loss of intelligence in the maps for the models with greater number of nodes. The fact that the nodes also are not uniformly distributed, in Figure 6.3 (d)-(f) is visible the concentration of nodes nearby these same mentioned regions, also introduce variation of results between the considered models.

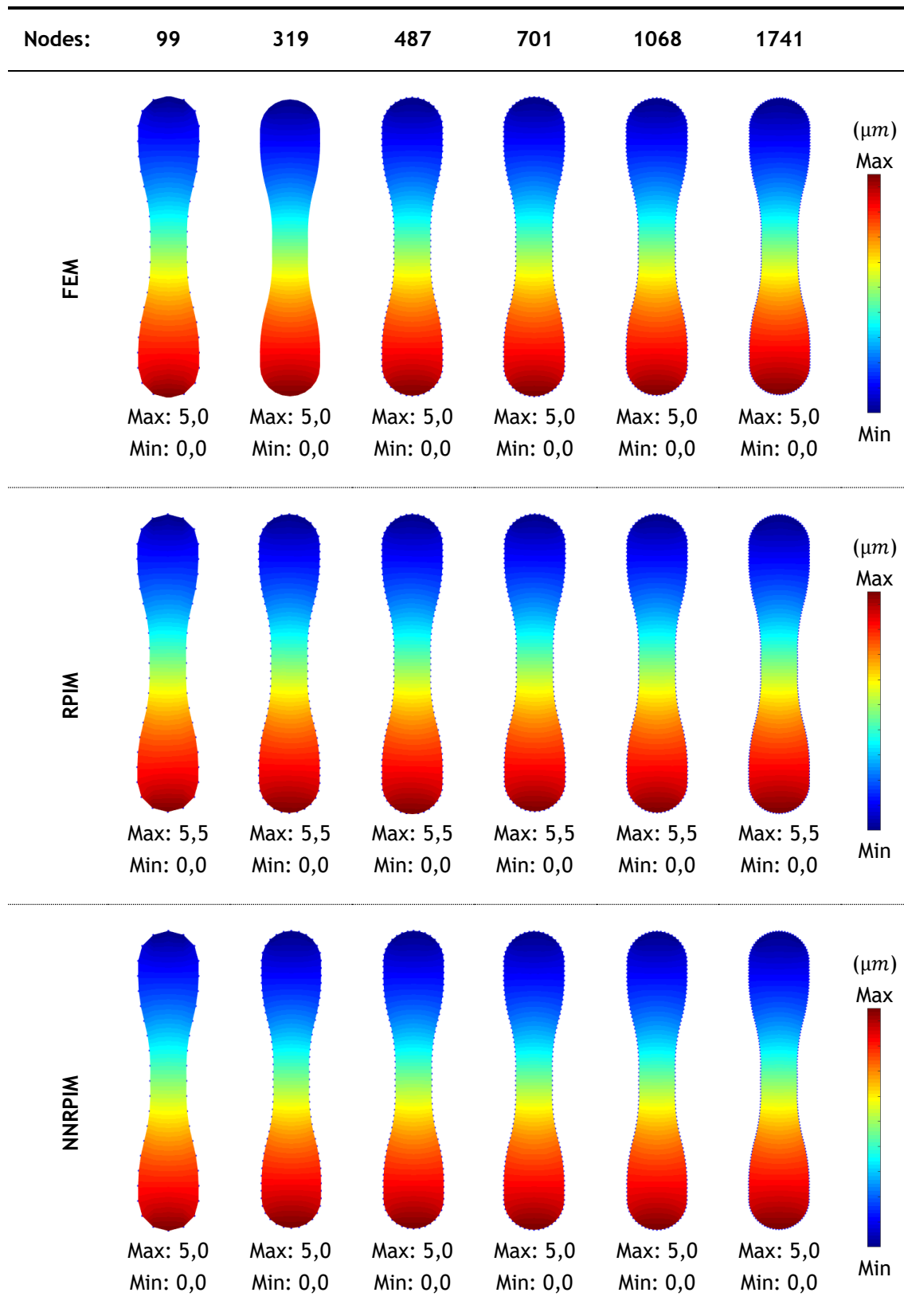
Table 6.1 - Displacement ($\|u\|$) field for elasto-static nodal discretization study.

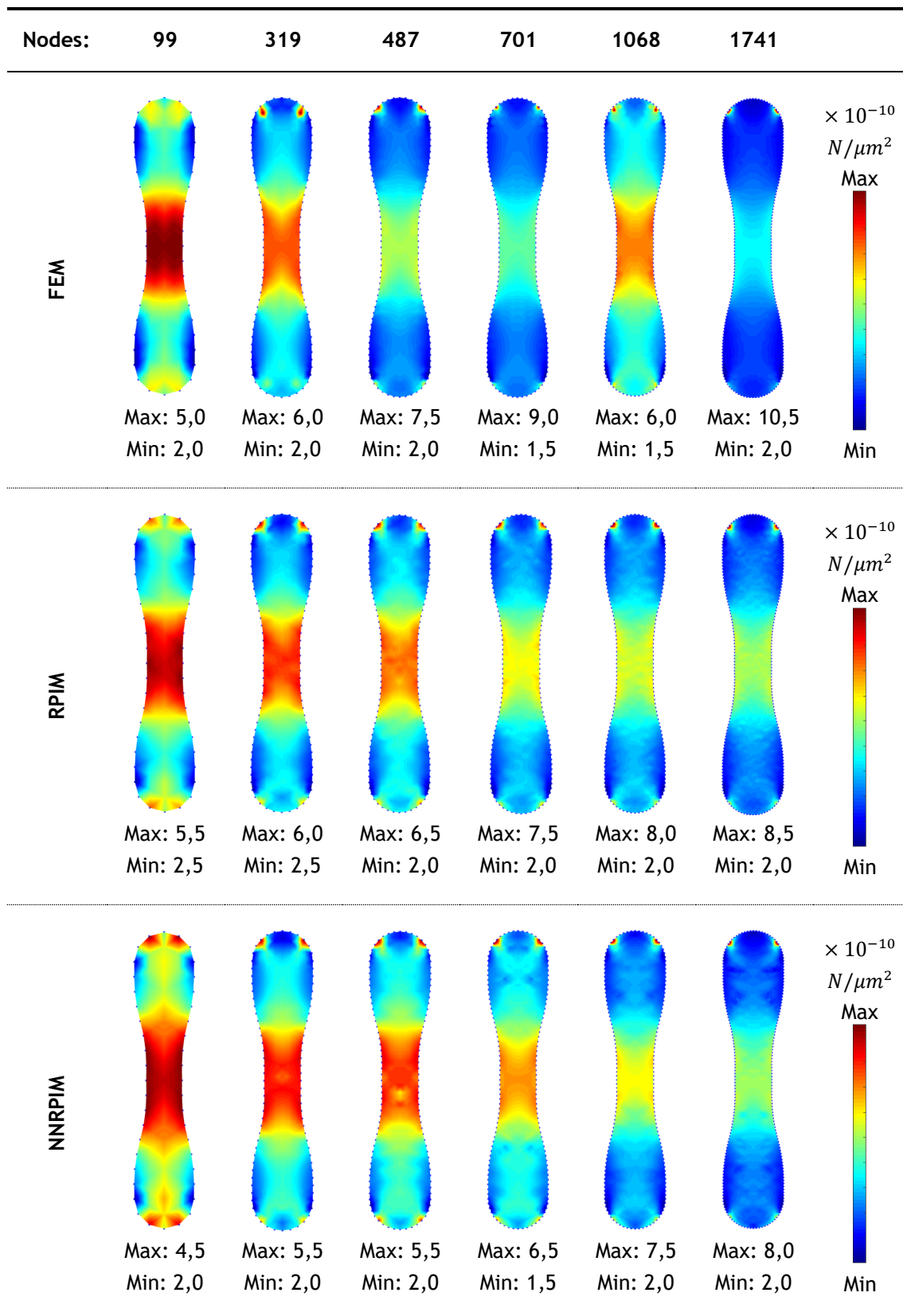
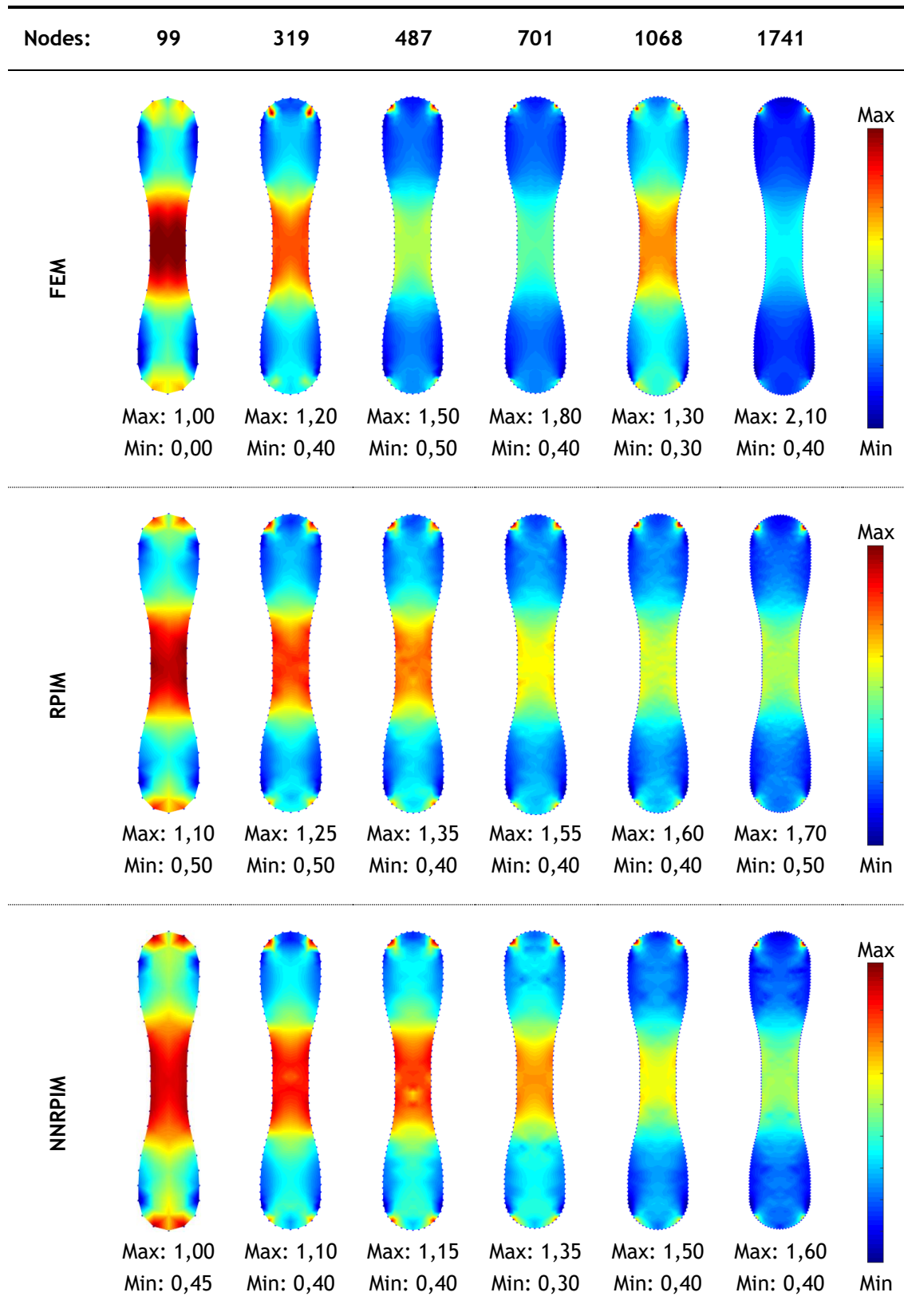
Table 6.2 - von Mises effective stress (σ_{eq}) field for elasto-static nodal discretization study.

Table 6.3 - Equivalent effective strain (ε_{eq}) field for elasto-static nodal discretization study.

6.2.2 - Free-Vibrations

Evaluating the convergence curves of the natural frequencies of vibration of the model under study, for a growing number of nodes, and for the first 3 modes of vibration, Figure 6.7 , Figure 6.8 and Figure 6.9, show that these tend to stabilize for a number higher than 1068 nodes. The third mode, with higher frequency, is the last to converge (with higher number of nodes).

According to Sec. 4.3.2 - , Table 6.4, Table 6.7 and Table 6.10 show the parameterized displacement field obtained using FEM, RPIM and NNRPIM respectively. On these cases, the maximum parameterized displacement that can be found actual corresponds to the vibration frequency of the given mode. In Table 6.5, Table 6.8 and Table 6.11 are presented the parameterized von Mises effective stress field of natural fibrational modes 1-3 usig FEM, RPIM and NNRPIM. And, for last, in Table 6.6, Table 6.9 and Table 6.12 are shown the parameterized equivalent effective strain using FEM, RPIM and NNRPIM, respectevly.

The obtained results using FEM for the model composed by 99 nodes were ignored because they were very different from the other, probably due to mesh incompatibilities.

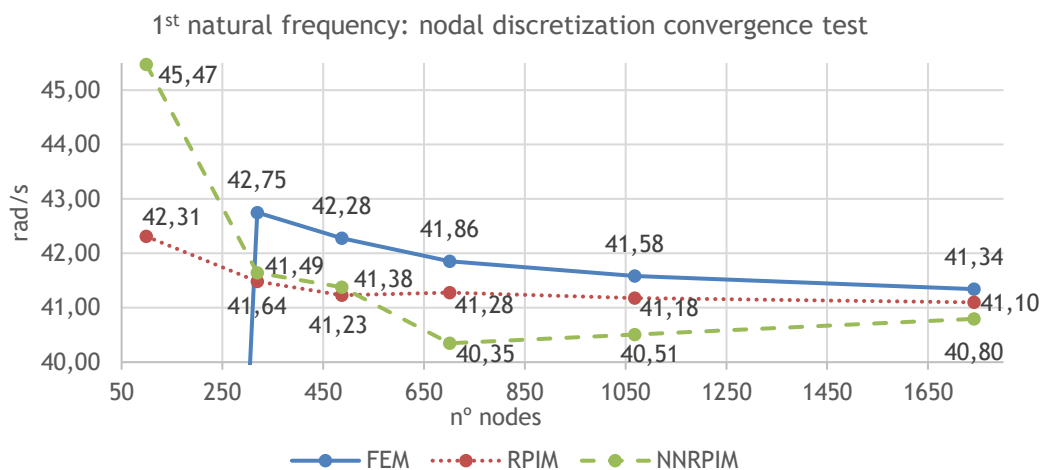


Figure 6.7 - 1st natural vibrational frequency evaluation with increasing number of nodes and per numerical method.

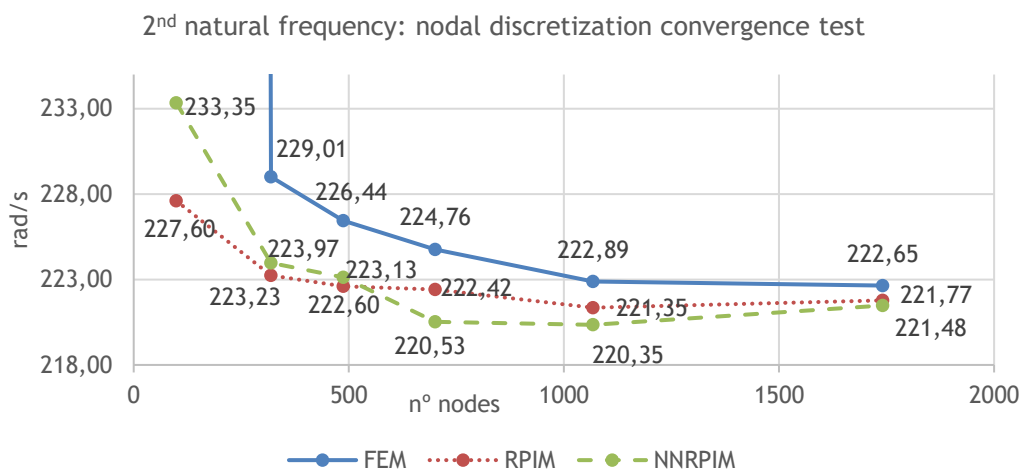


Figure 6.8 - 2nd natural vibrational frequency evaluation with increasing number of nodes and per numerical method.

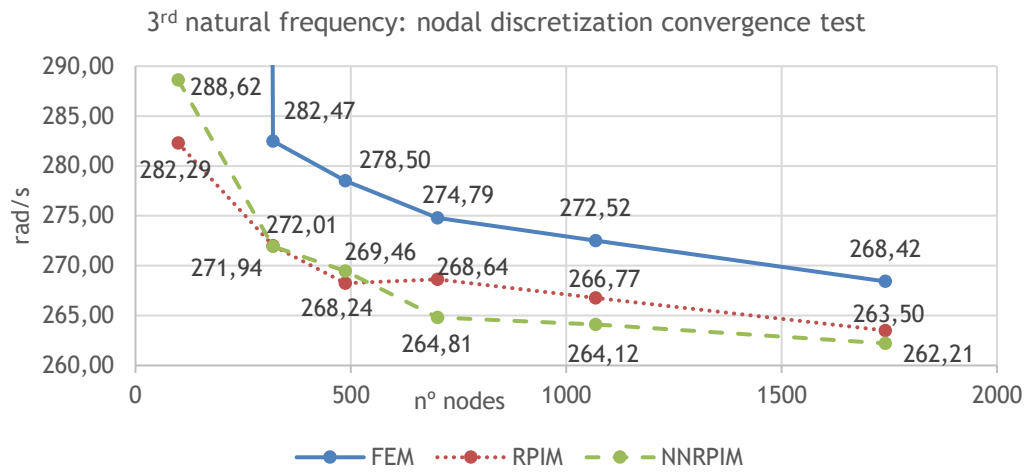


Figure 6.9 - 3rd natural vibrational frequency evaluation with increasing number of nodes and per numerical method.

Table 6.4 - Parameterized displacement field of natural vibrational modes 1-3 usig FEM.

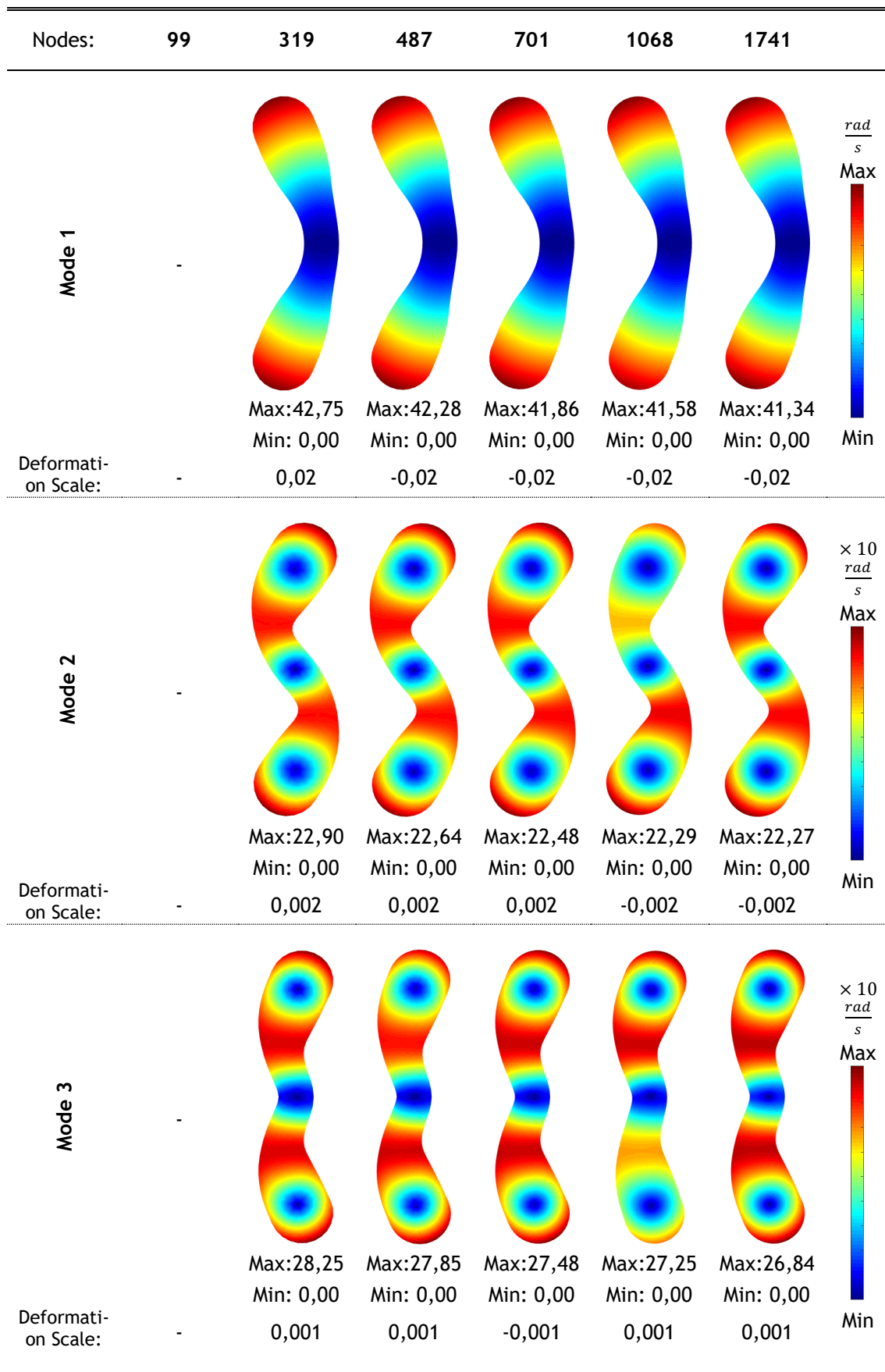


Table 6.5 - Parameterized von Mises effective stress field of natural vibrational modes 1-3 usig FEM.

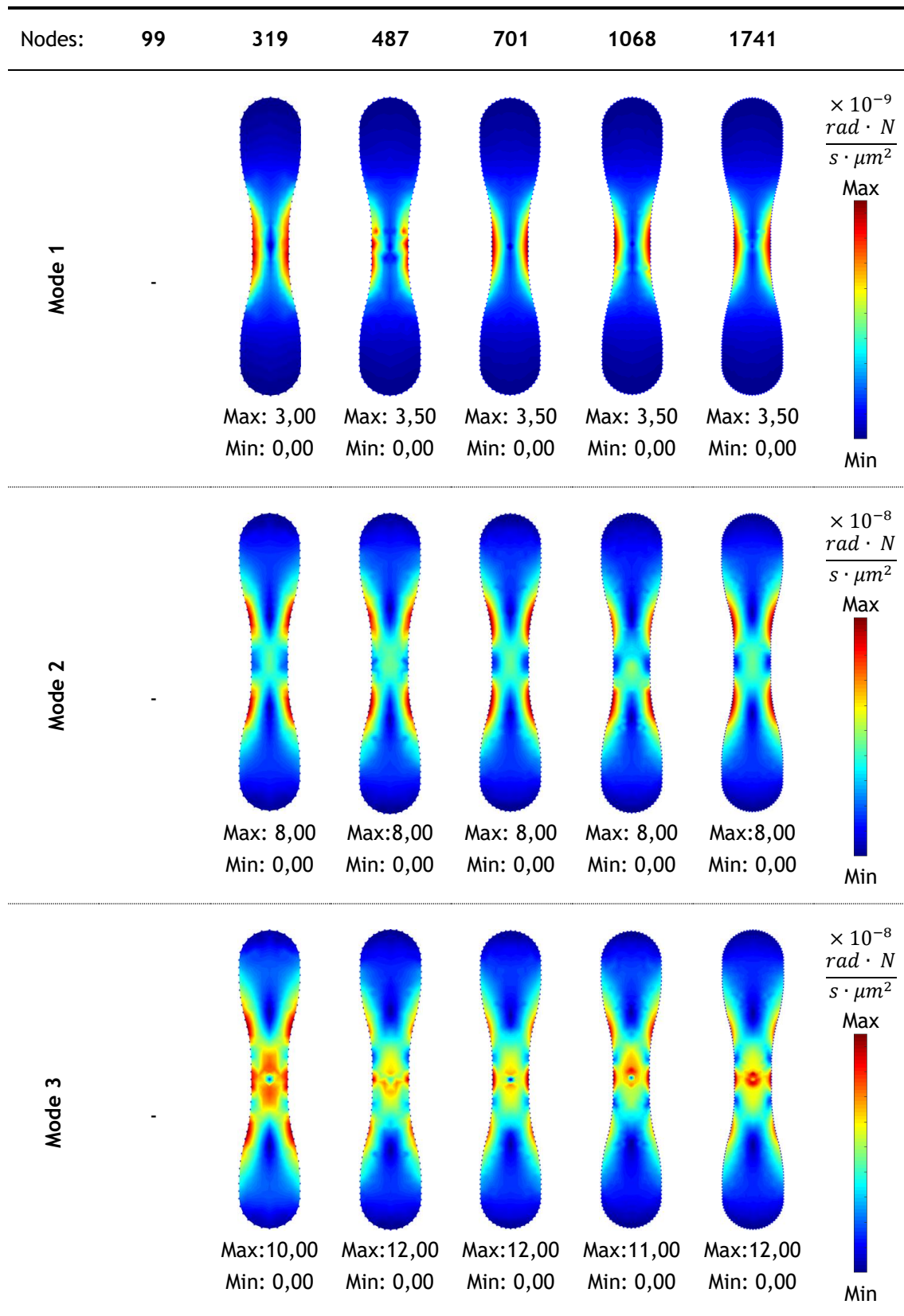


Table 6.6 - Parameterized equivalent effective strain of natural vibrational modes 1-3 using FEM.

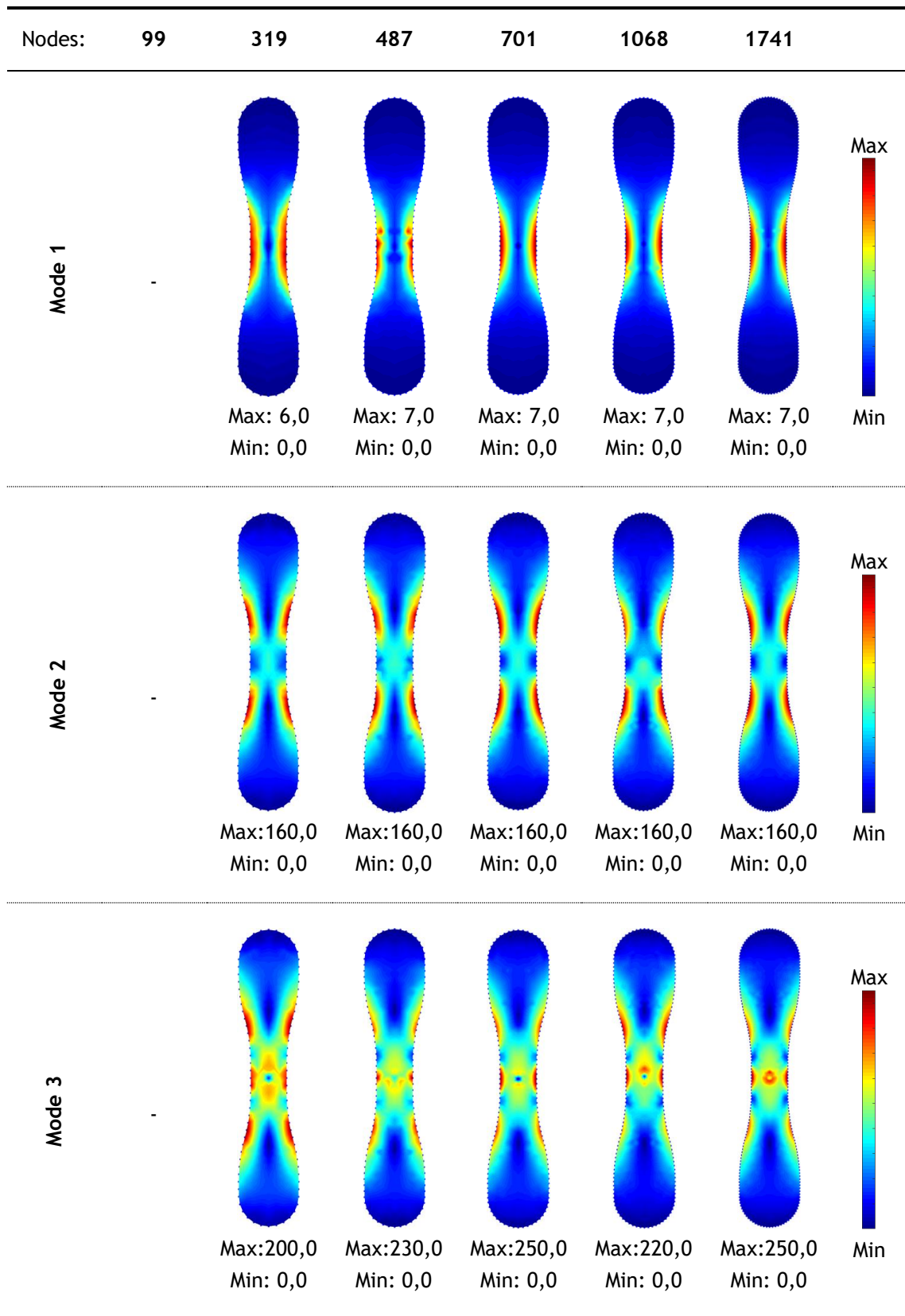


Table 6.7 - Parameterized displacement field of natural vibrational modes 1-3 usig RPIM.

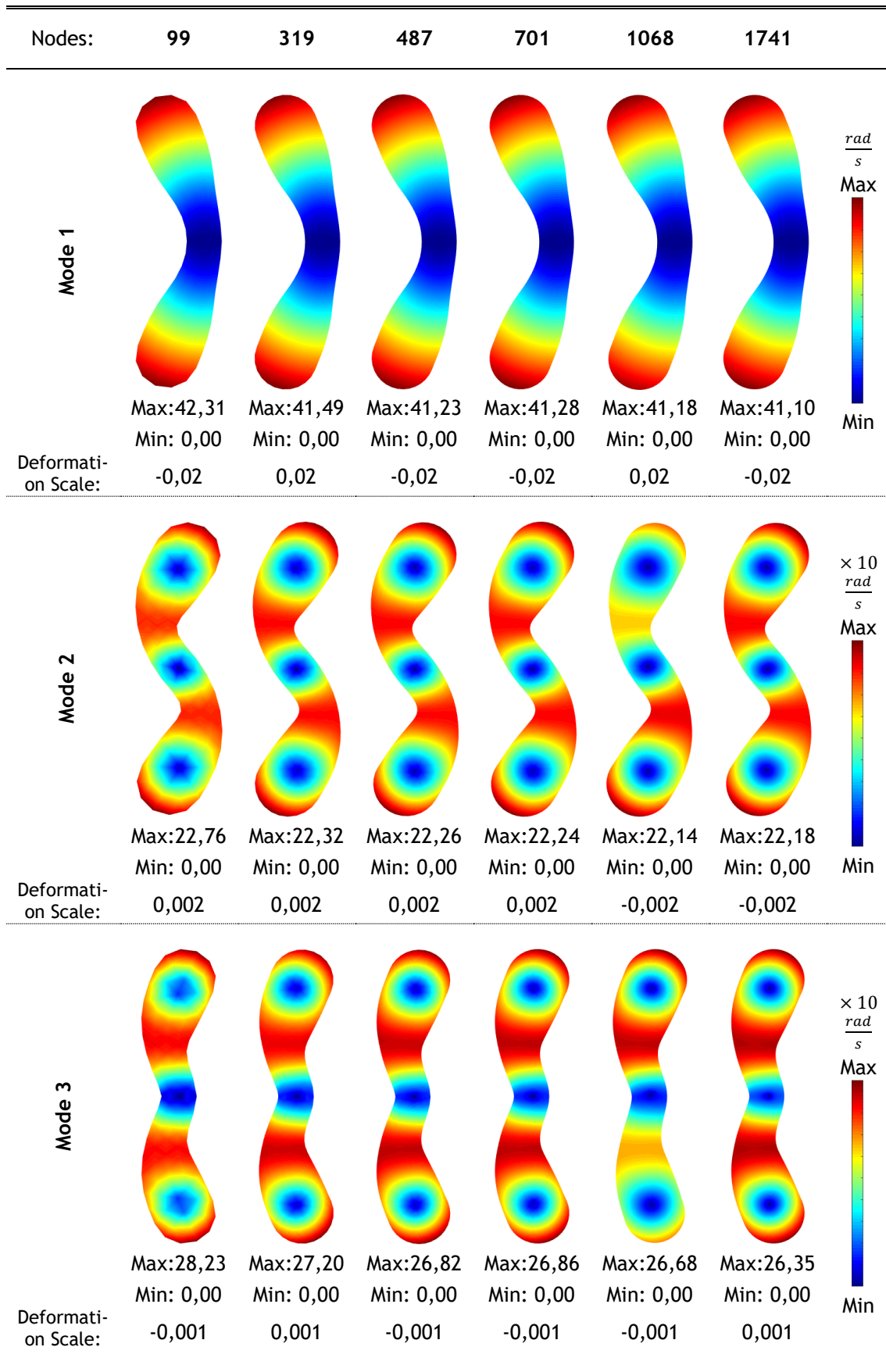


Table 6.8 - Parameterized von Mises effective stress field of natural vibrational modes 1-3 usig RPIM.

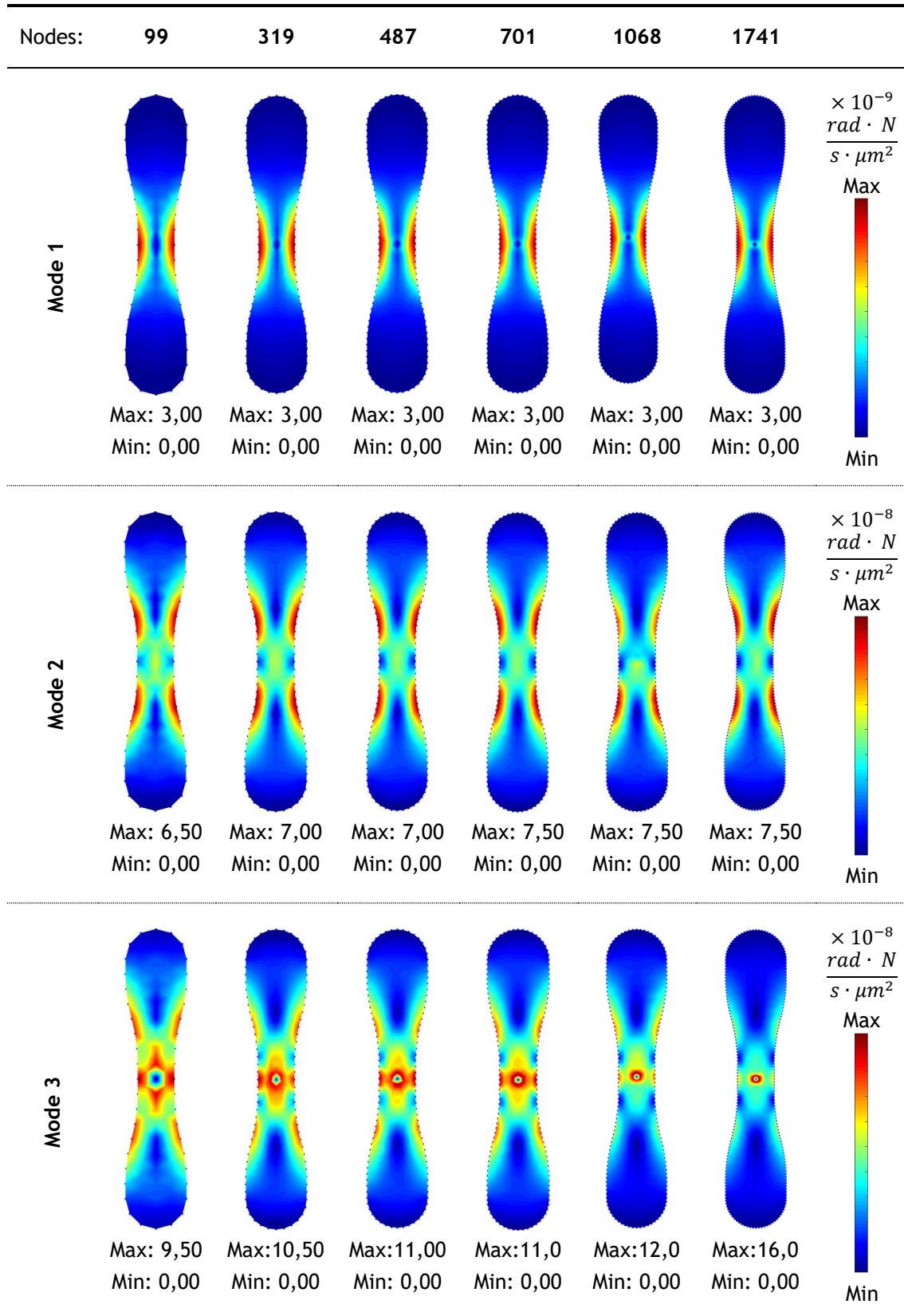


Table 6.9 - Parameterized equivalent effective strain of natural vibrational modes 1-3 usig RPIM.

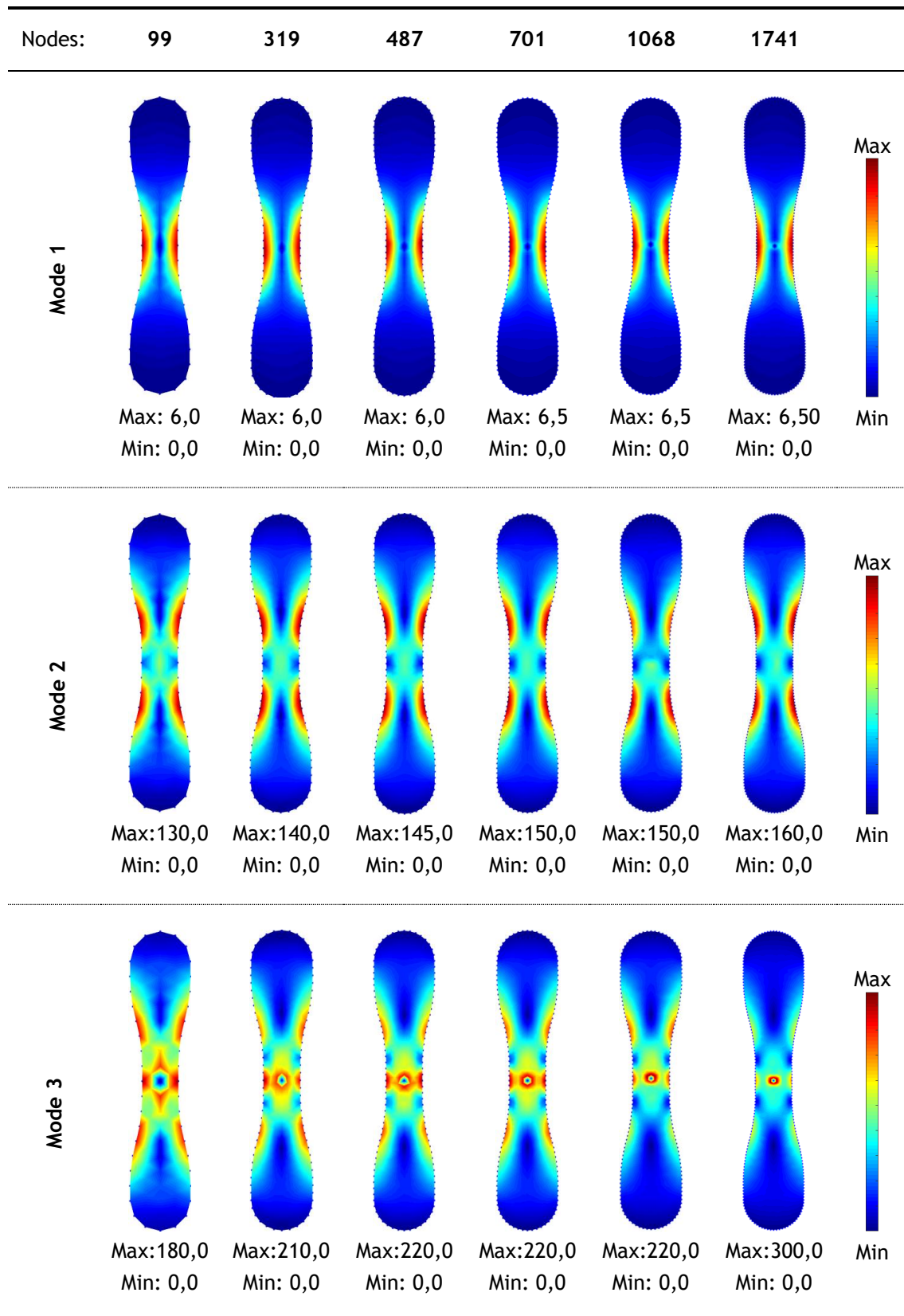


Table 6.10 - Parameterized displacement field of natural vibrational modes 1-3 usig NNRPIM.

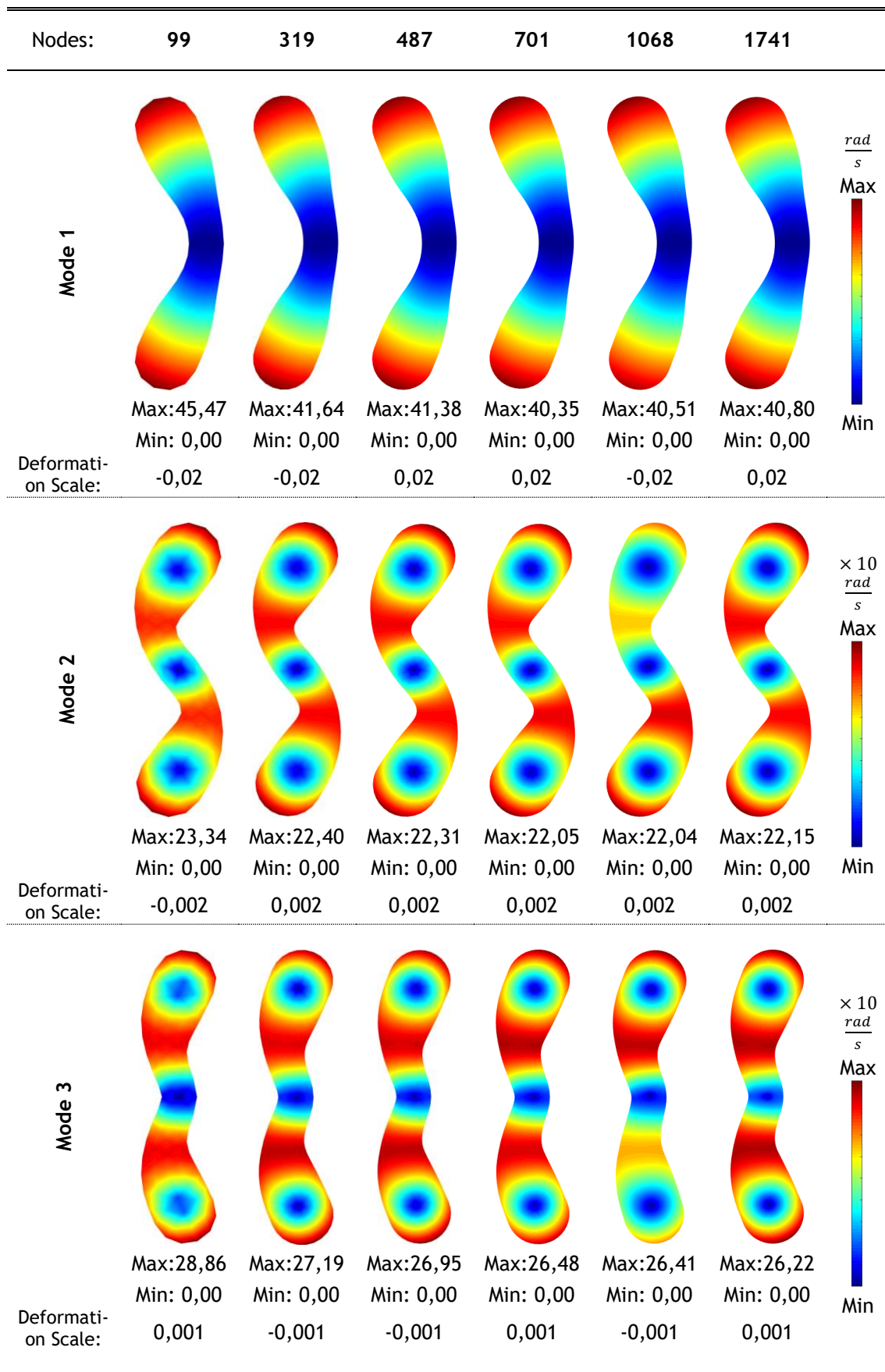


Table 6.11 - Parameterized von Mises effective stress field of natural vibrational modes 1-3 usig NNRPIM.

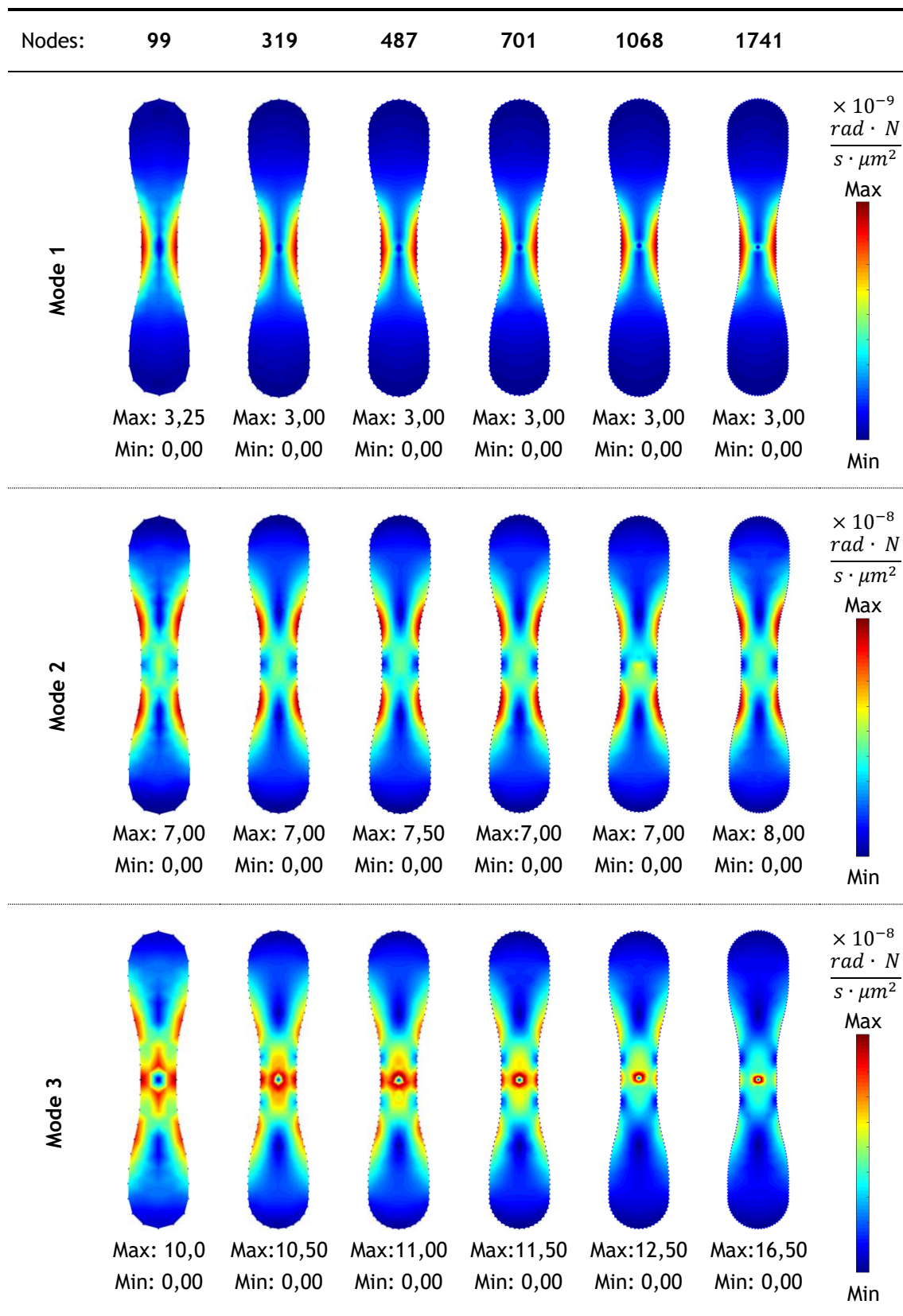
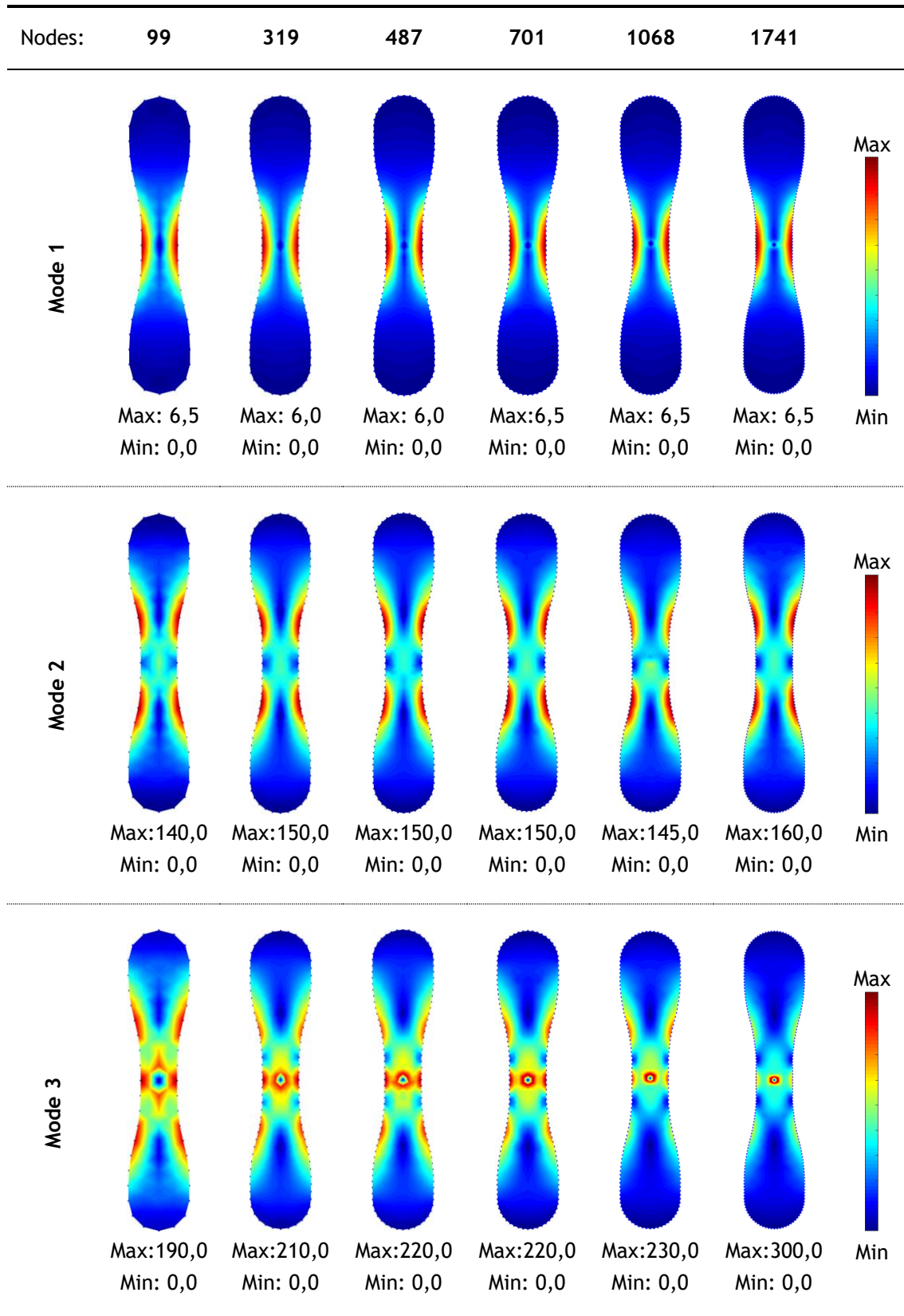


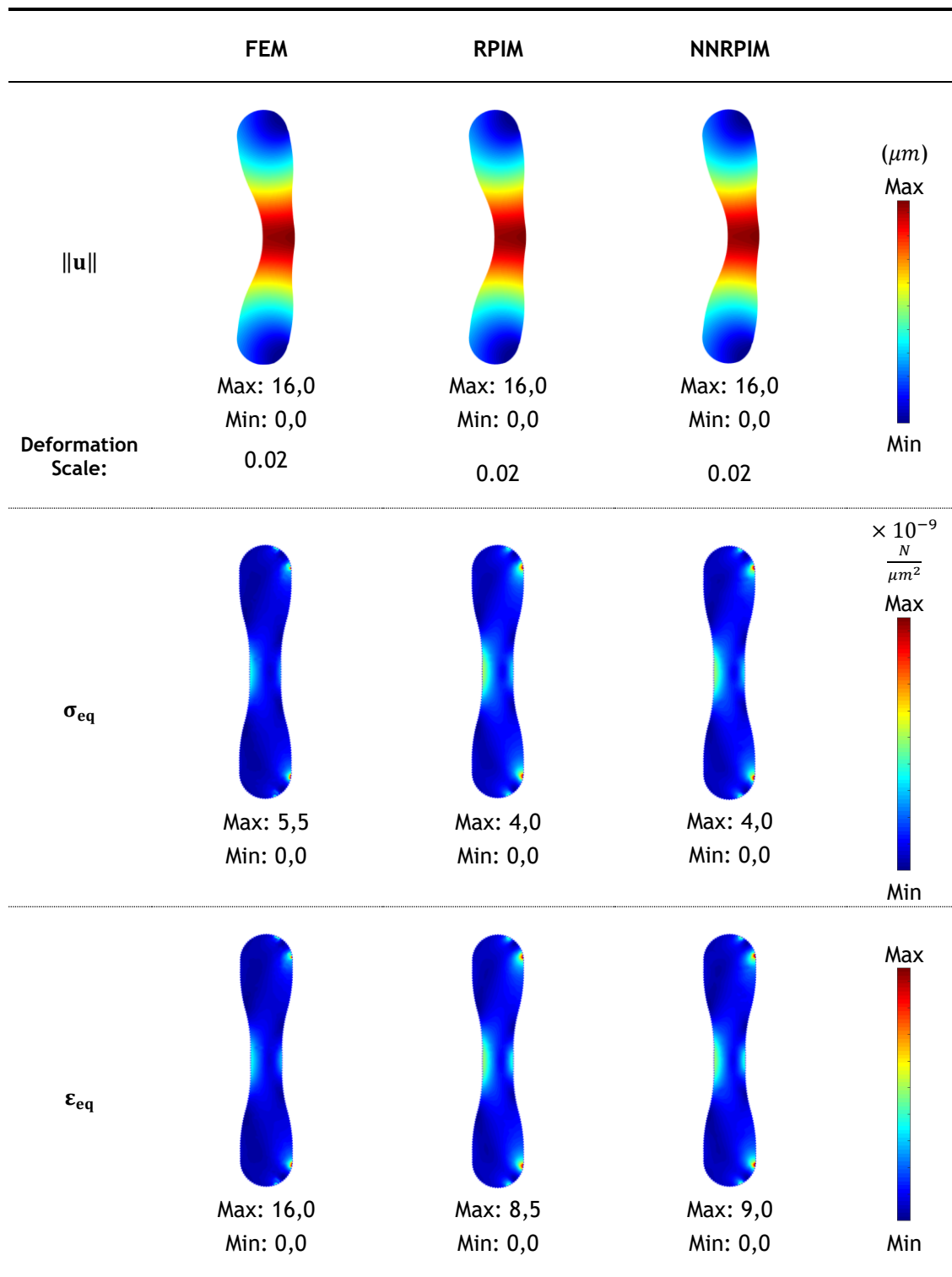
Table 6.12 - Parameterized equivalent effective strain of natural vibrational modes 1-3 using NNRPIM.



6.2.3 - Bending Test

After testing how the number of nodes influences the response to loading situations and the natural vibrations, which revealed the preference for higher number of nodes discretizing the problem in both situations, it was conducted the bending test with the model with 1761 nodes.

Table 6.13 - Bending test with 1761 nodes model



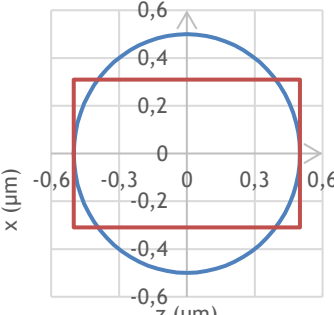
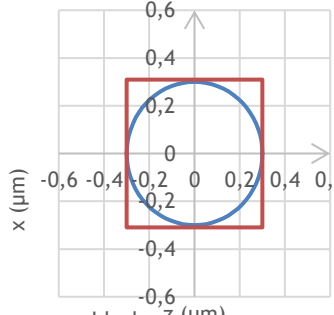

Analyzing the distribution of the effective stresses and the effective strain, it is once again visible the introduction of artifacts by the imposition of the boundary conditions. It is possible to see the typical field of deformation during the median chromosome division, but it is not possible to take many mechanical inferences on this biological process. Further study would require a more detailed analysis of the sites and how the fibers of the achromatic spindle attach to the chromosome and the properties of the surrounding environment but also study what are the best boundary conditions to impose on the model in order to simulate this specific process.

6.3 - 2D Shell-Like Convergence Study

As mentioned in the previous chapter, nowadays it is fashionable and preference is given to the use of three-dimensional models for a variety of reasons. The use of two-dimensional models is however still frequent and may prove to be advantageous. One of the concerns in their use is that they portray the 3D problem as reliably as possible and investigators have invested heavily in new techniques and comparative studies between the use of 2D and 3D models. One of the possible ways to try to approximate 2D models of chromosomes to three-dimensional models is to define areas with different thicknesses instead of assigning a single one to the entire domain. Thus, in this work, it is attempted to define several layers to approximate the chromosome to a cylindrical structure. The thickness of the various layers was approximated by reference to the larger cross-sectional area. Table 6.14 shows a schematization of how models with different number of layers were defined.

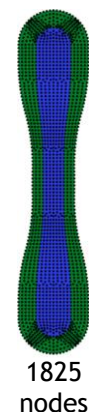
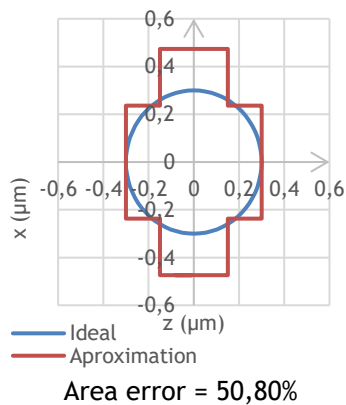
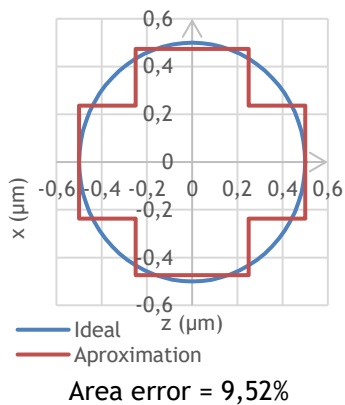
From the previous section, it turned out that more than 1068 nodes and less than 2000 should be used to discretize the problem. For reasons of comparison, models with a number of nodes as close as possible to 1741 should be used, however, because the models constructed to carry out this study are composed of different numbers of layers (similar to a shell or an onion), sometimes there is a deviation from this number. In the last column of the Table 6.14 can be visualized the final model used for each case, as well as the number of nodes that compose the model.

Table 6.14 - Schematization of the cross-sectional area at two different points and definition of the thickness of each layer that compose each model.

| N° Layers | Thickness (μm) | Largest cross-section | Smaller cross-section | XY View |
|-----------|-----------------------------|---|--|---|
| 1 | $e_1 = 0,619$ |  <p>— Ideal — Aproximation Area error = 21,18%</p> |  <p>— Ideal — Aproximation Area error = 31,36%</p> |  <p>1785 nodes</p> |

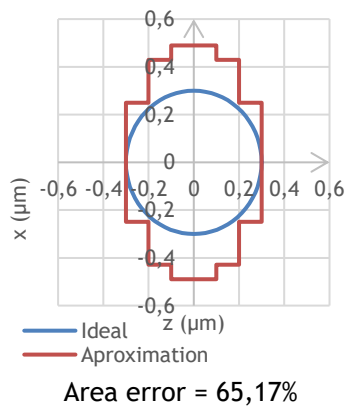
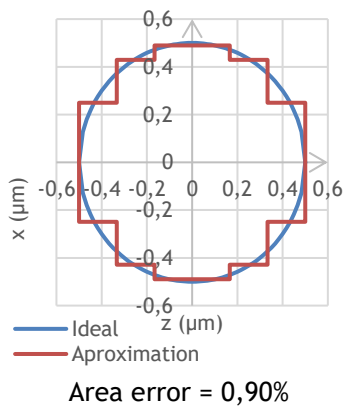
2

- $e_1 = 0,948$
- $e_2 = 0,474$



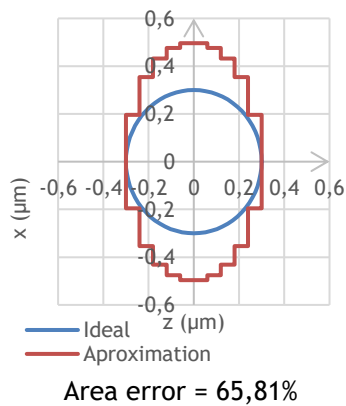
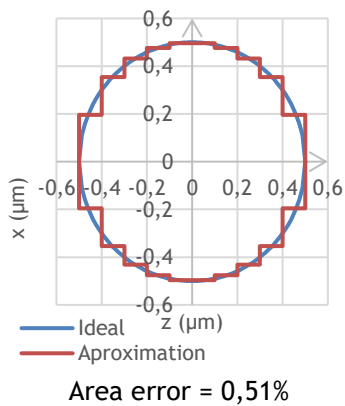
3

- $e_1 = 0,979$
- $e_2 = 0,857$
- $e_3 = 0,498$



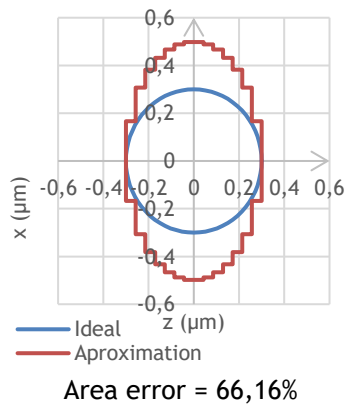
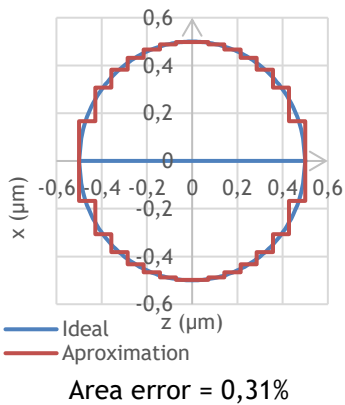
5

- $e_1 = 0,992$
- $e_2 = 0,952$
- $e_3 = 0,863$
- $e_4 = 0,708$
- $e_5 = 0,392$



7

- $e_1 = 0,996$
- $e_2 = 0,976$
- $e_3 = 0,933$
- $e_4 = 0,864$
- $e_5 = 0,764$
- $e_6 = 0,614$
- $e_7 = 0,334$



6.3.1 - Stress-strain experiment simulation

In Figure 6.10 is presented the Cauchy strain in the neck region, obtained for an increasing number of layers that discretizes the problem domain and for the three numerical methods tested. Figure 6.4 shows the equivalent Young modulus obtained from the displacement on this same region.

Table 6.15, Table 6.16 and Table 6.17 have the color maps for displacement, von Mises effective stress and equivalent effective strain fields, respectively.

The analysis of the convergence curves does not allow to clearly identify a tendency of convergence, so the use of a greater number of layers to describe the problem cannot be associated to a modeling closer to the exact one. In agreement with the study of convergence of the number of nodes, the zone of the chromosome that most influences in the test of traction is the thinner region - the neck. In this way, and at this moment without other studies, the two-dimensional model should privilege a greater approximation to the smaller area of cross-section and by the Table 6.14, a single layer should be used. Another point that does not allow to establish comparisons and define the best methodology is the simplicity of the used models' geometry. There are several important differences between the model geometry and the actual chromosomes structure and the most critical is the large and thin neck in the central portion of the model. This neck has a smooth transition to the arms extremities what does not happen in chromosomes and it was not considered the many groves along chromatid arms.

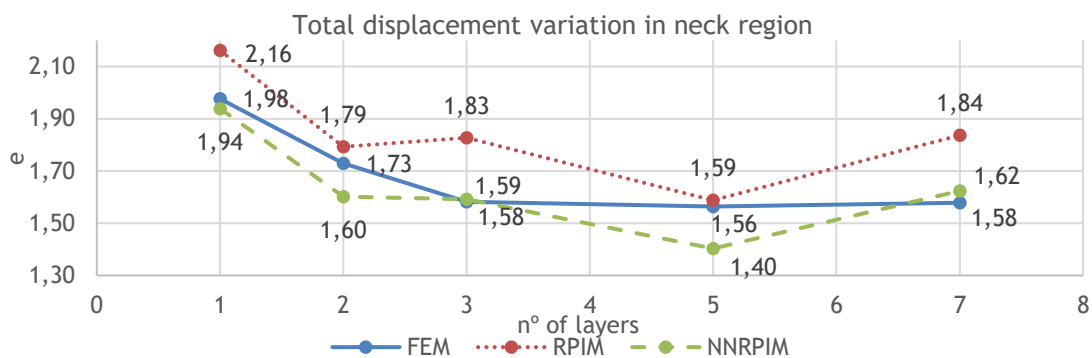


Figure 6.10 - Total displacement variation with increasing number of layers and per numerical method.

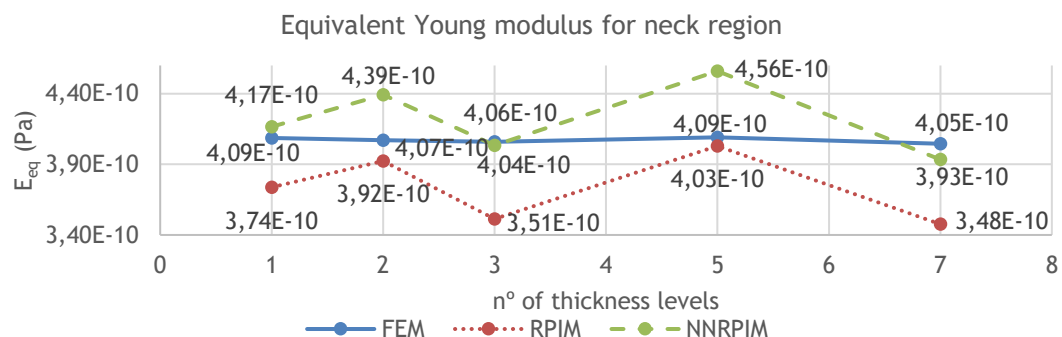


Figure 6.11 - Equivalent Young modulus variation with increasing number of layers and per numerical method.

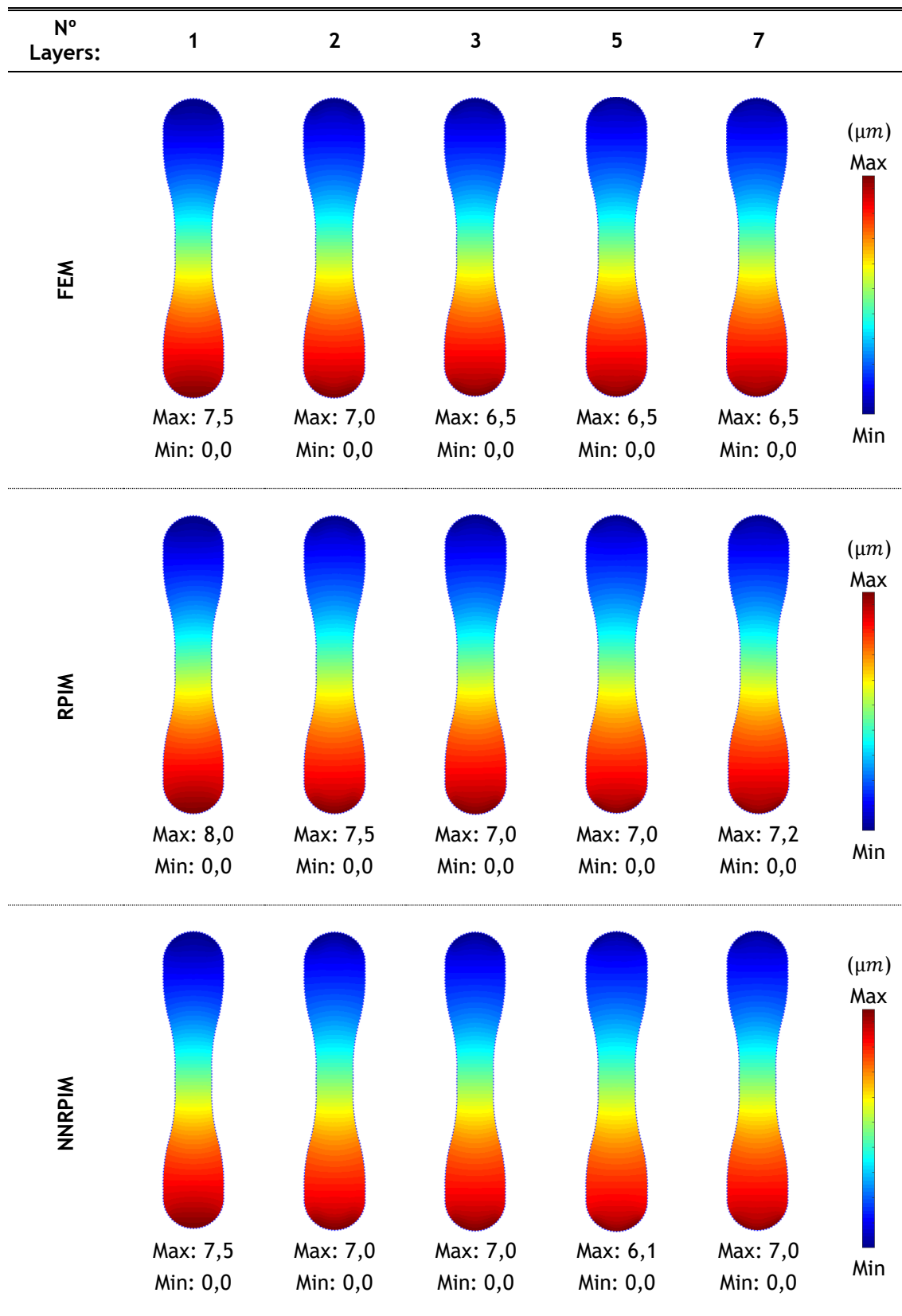
Table 6.15 - Displacement ($\|u\|$) field for elasto-static 2D shell-like convergence study.

Table 6.16 - von Mises effective stress (σ_{eq}) field for elasto-static 2D shell-like convergence study.

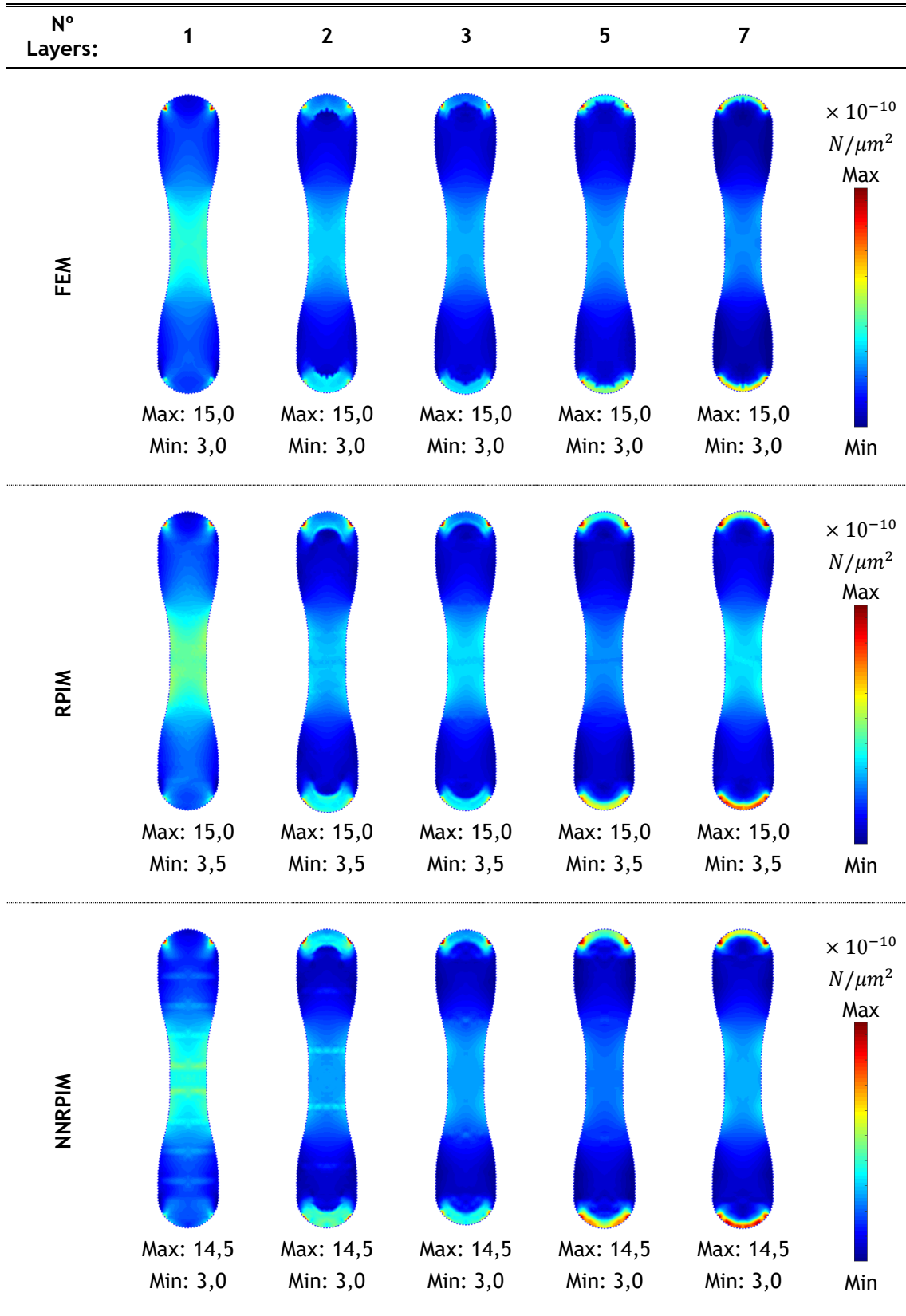
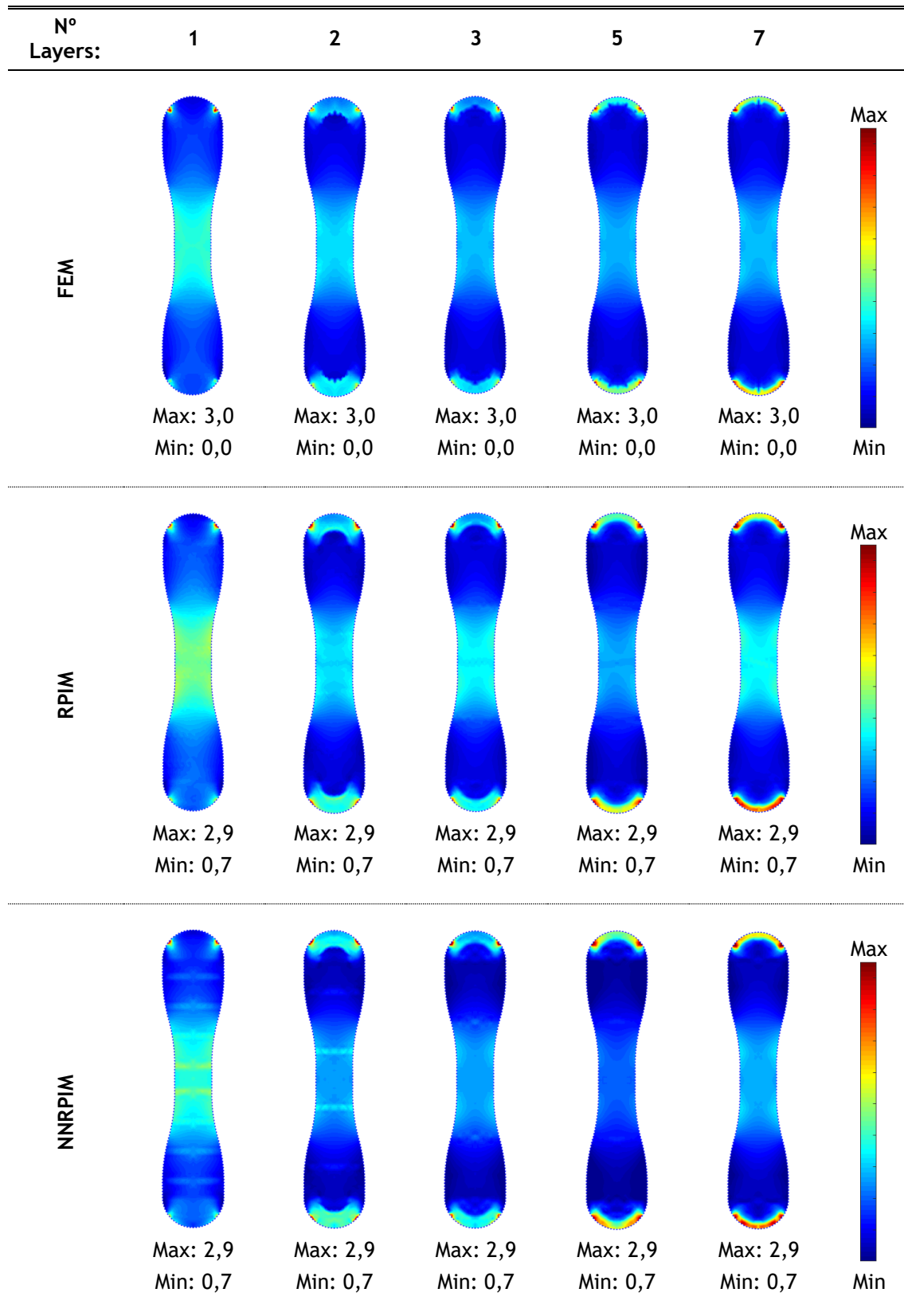


Table 6.17 - Equivalent effective strain (ε_{eq}) field for elasto-static 2D shell-like convergence study.



6.3.2 - Free-Vibrations

The study of the influence of using different number of layers with different thicknesses on the first three natural vibration frequencies is presented in Figure 6.12, Figure 6.13 and Figure 6.14. For a more exhaustive comparative study, Table 6.18, Table 6.21 and Table 6.24 show the parameterized displacement field obtained using FEM, RPIM and NNRPIM respectively; In Table 6.19, Table 6.22 and Table 6.25 *Erro! A origem da referência não foi encontrada.* are presented the parameterized von Mises effective stress field of natural vibrational modes 1-3 using FEM, RPIM and NNRPIM; And for last, in Table 6.20, Table 6.23 and Table 6.26 are shown the parameterized equivalent effective strain.

Unlike the stress-strain test, there seems to be a pattern of convergence at natural vibration frequencies. This convergence of results may however be due only to the fact that as more layers are used to describe the chromosome, the smaller the variations occurring at the level of the cross-sectional areas. This decrease in the variation of the cross-sectional area, the thickness of the chromosome, leads by itself to the convergence of the results and can not therefore be clearly associated with obtaining results that are closer to those that would be obtained in a three-dimensional simulation. At this point, it is not advantageous to use several layers for 2D problems also due to the greater effort that is necessary to employ in the construction of the models.

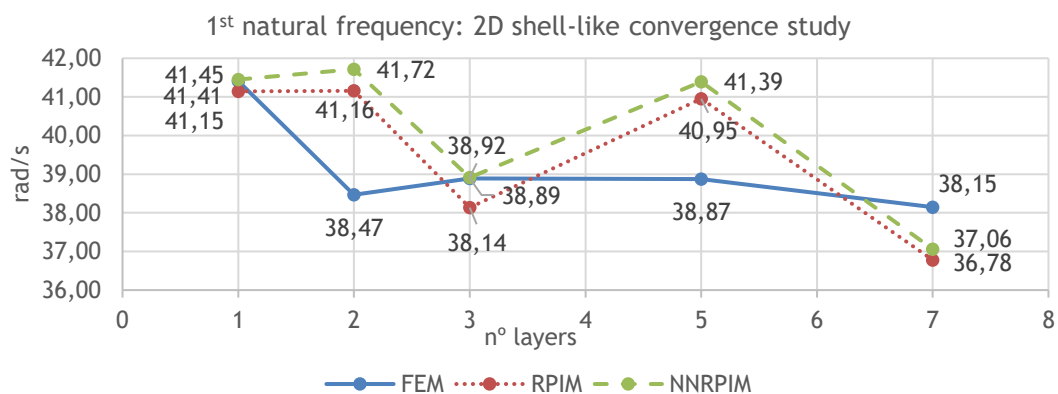


Figure 6.12 - 1st natural vibrational frequency evaluation with increasing number of layers and per numerical method.

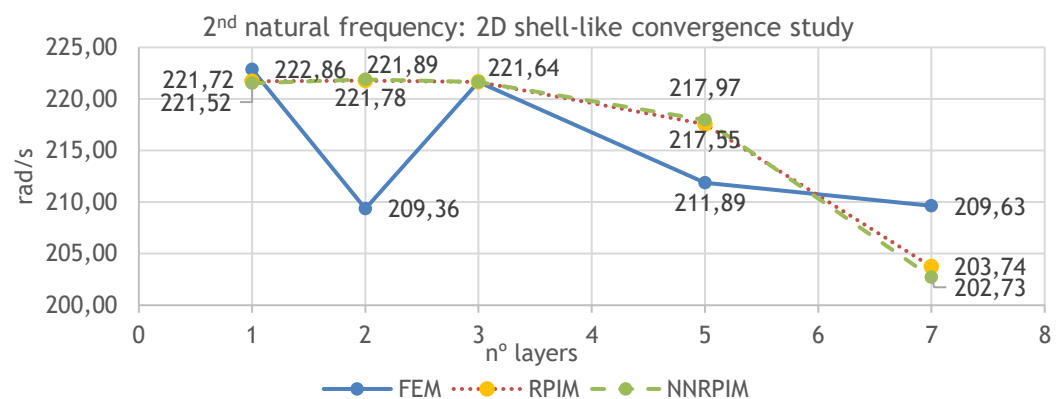


Figure 6.13 - 2nd natural vibrational frequency evaluation with increasing number of layers and per numerical method.

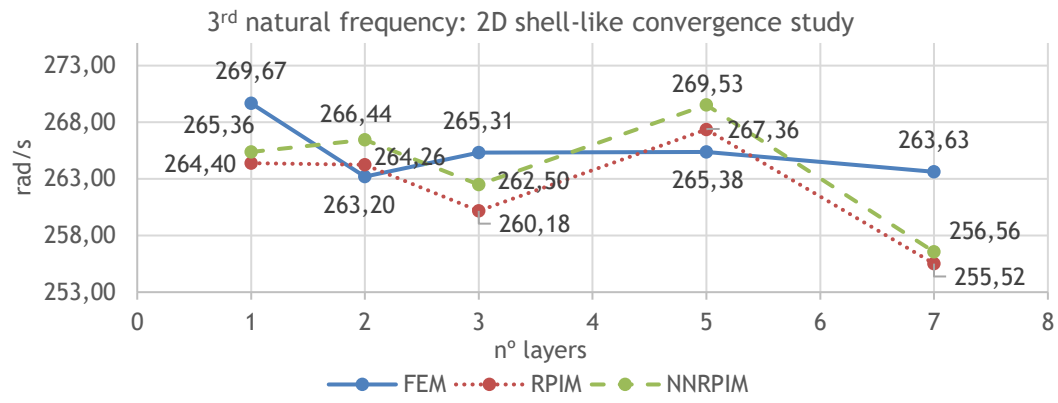


Figure 6.14 - 3rd natural vibrational frequency evaluation with increasing number of layers and per numerical method.

Table 6.18 - Parameterized displacement field of natural vibrational modes 1-3 usig FEM: 2D shell-like convergence study.

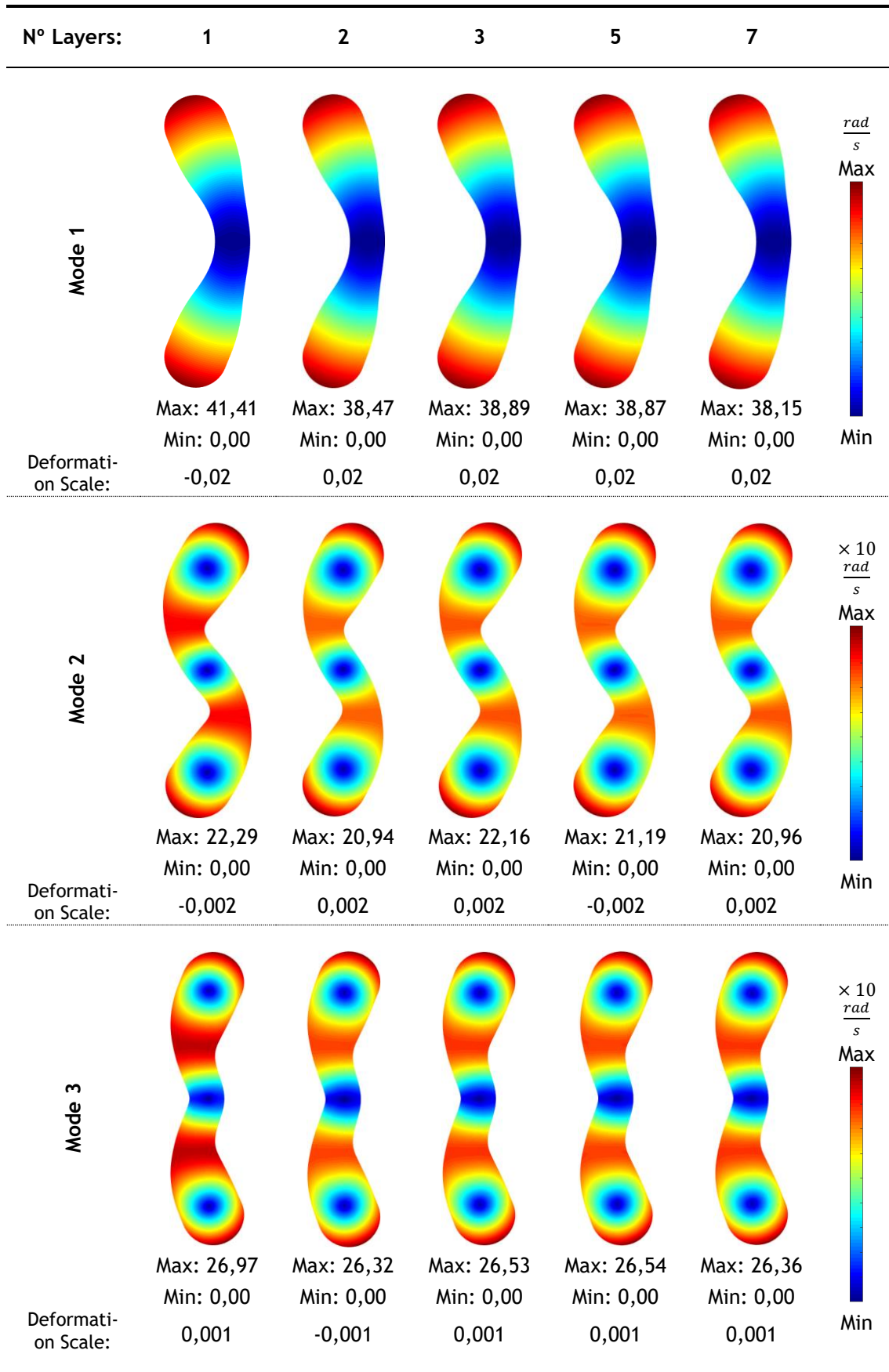


Table 6.19 - Parameterized von Mises effective stress field of natural vibrational modes 1-3 usig FEM: 2D shell-like convergence study.

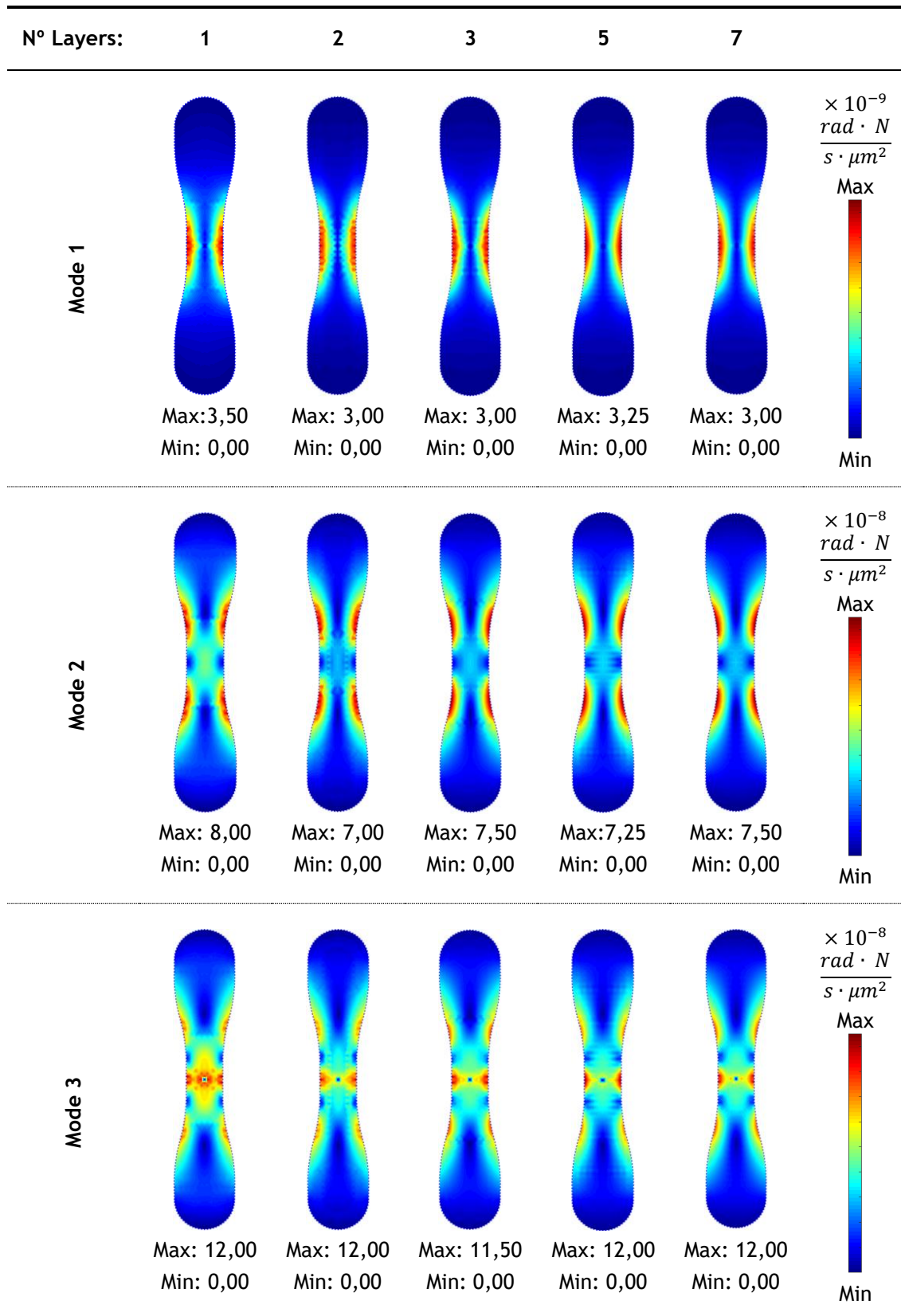


Table 6.20 - Parameterized equivalent effective strain field of natural vibrational modes 1-3 usig FEM: 2D shell-like convergence study.

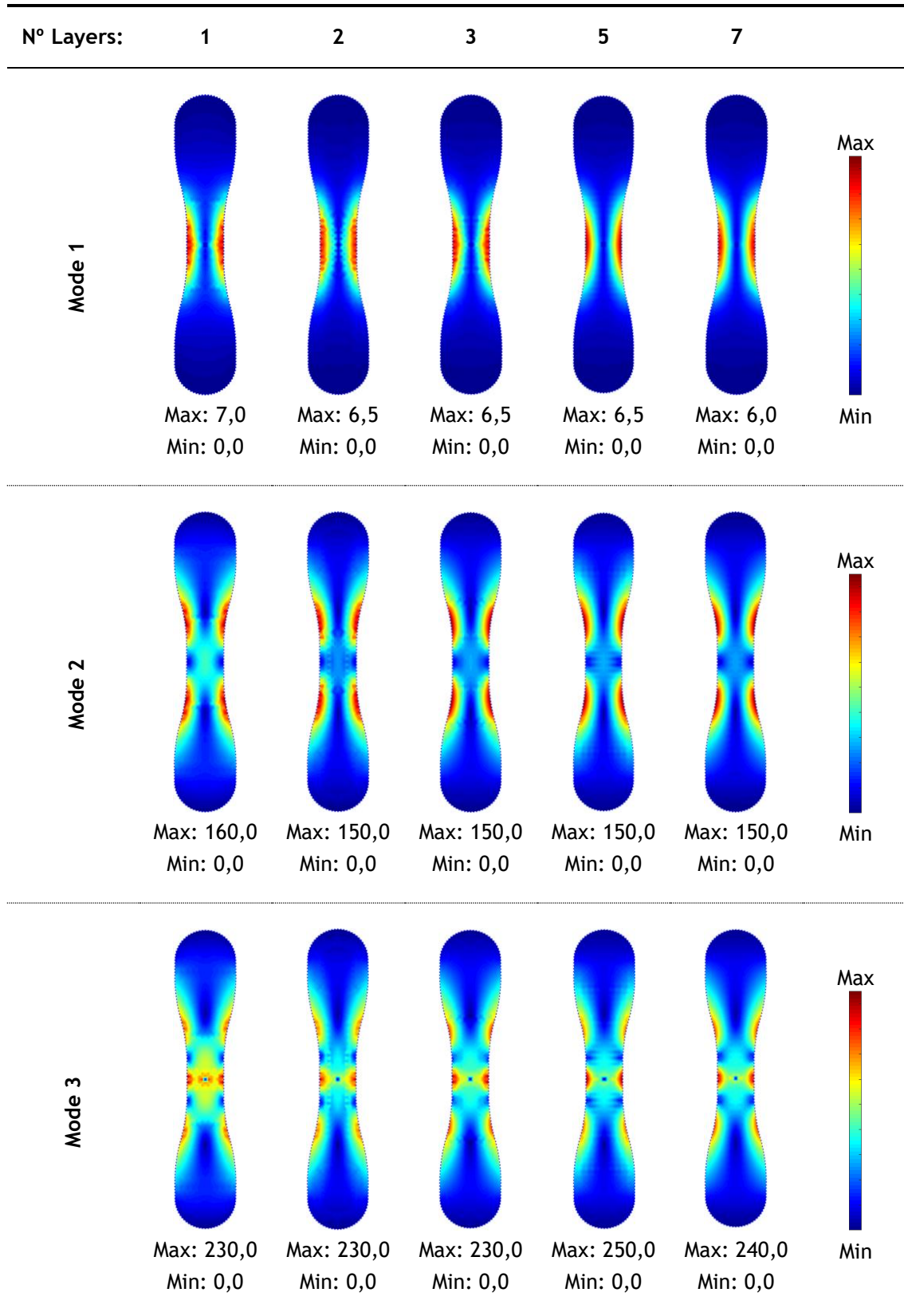


Table 6.21 - Parameterized displacement field of natural vibrational modes 1-3 using RPIM: 2D shell-like convergence study.

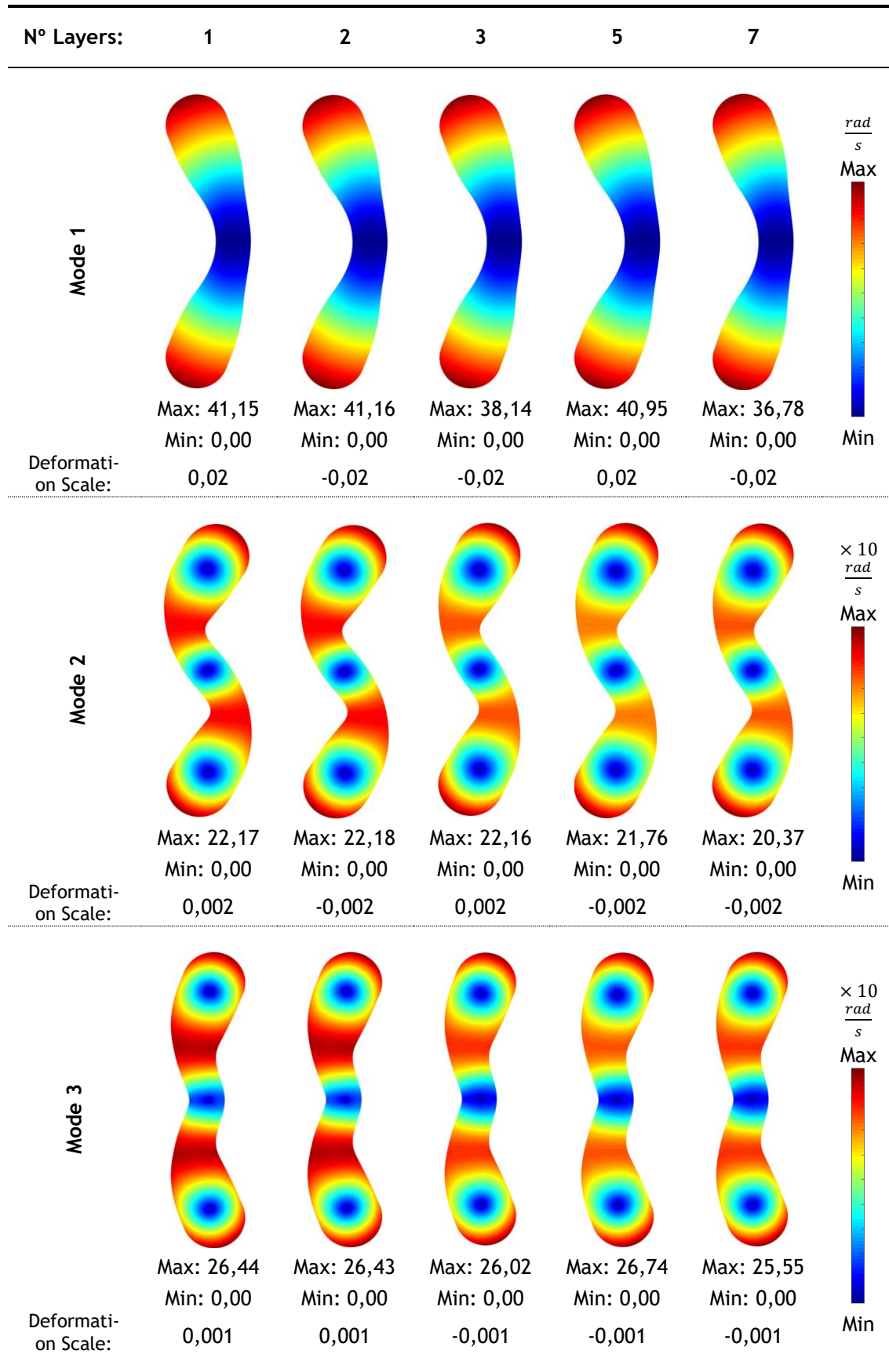


Table 6.22 - Parameterized von Mises effective stress field of natural vibrational modes 1-3 usig RPIM: 2D shell-like convergence study.

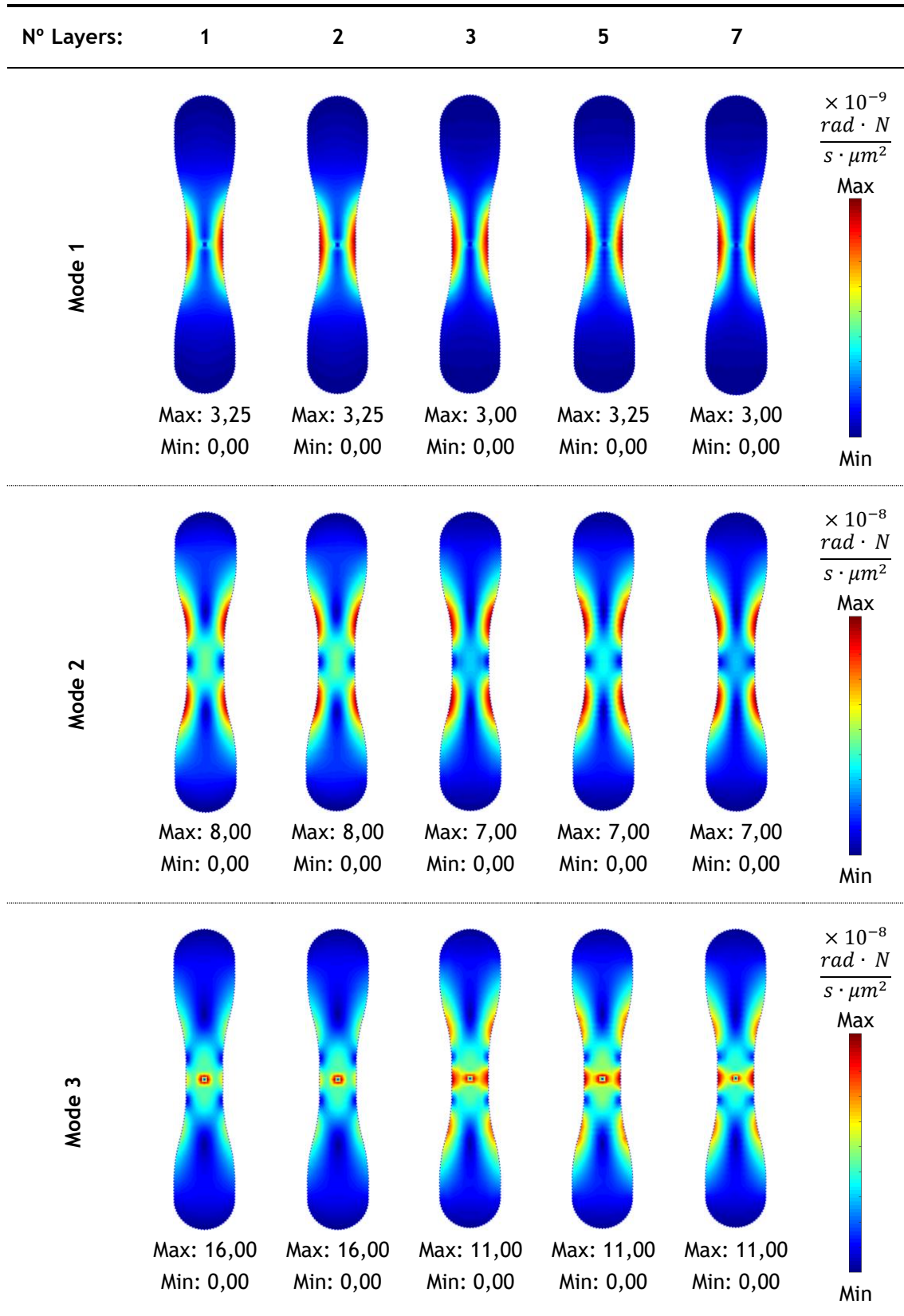


Table 6.23 - Parameterized equivalent effective strain field of natural vibrational modes 1-3 using RPIM: 2D shell-like convergence study.

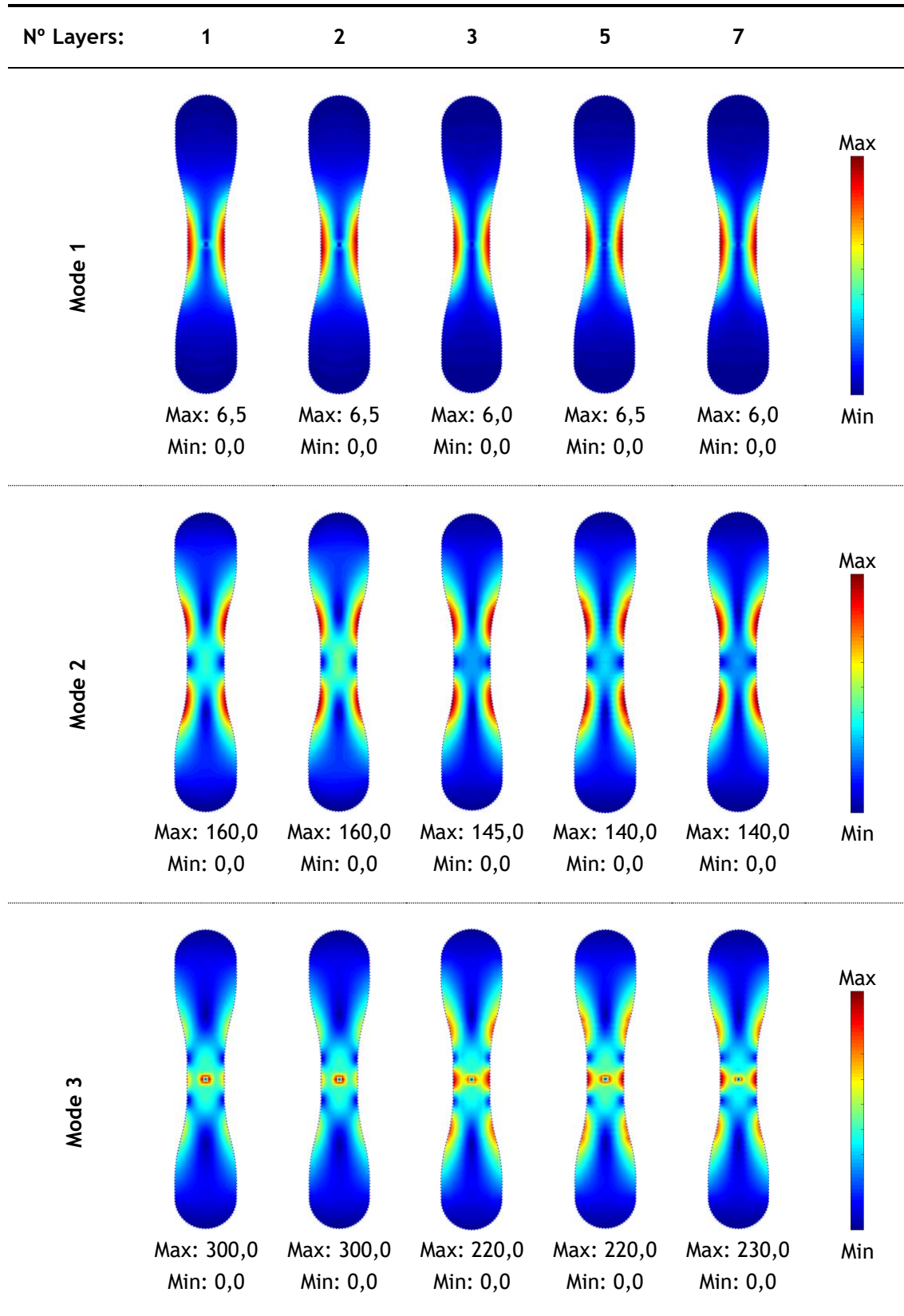


Table 6.24 - Parameterized displacement field of natural vibrational modes 1-3 using NNRPIM: 2D shell-like convergence study.







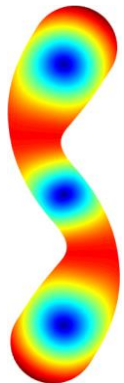
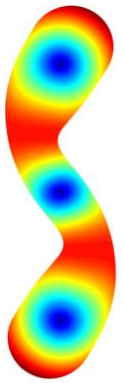
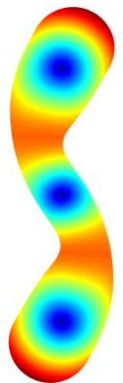
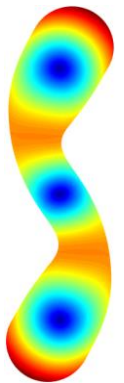
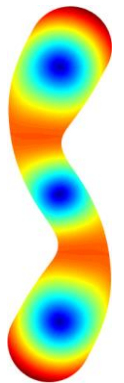

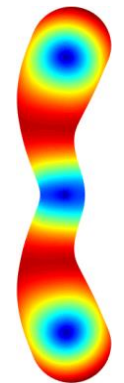
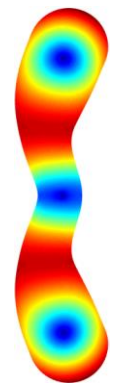
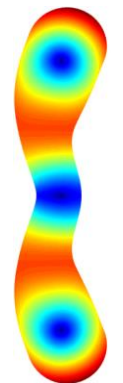
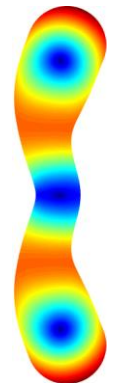
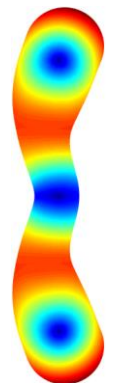
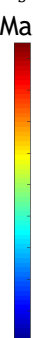
| N° Layers: | 1 | 2 | 3 | 5 | 7 | |
|--------------------|---|---|---|--|---|--|
| Mode 1 |  |  |  |  |  | $\frac{rad}{s}$ Max  Min |
| Deformation Scale: | Max: 41,45 Min: 0,00 0,02 | Max: 41,72 Min: 0,00 0,02 | Max: 38,92 Min: 0,00 -0,02 | Max: 41,39 Min: 0,00 0,02 | Max: 37,06 Min: 0,00 0,02 | |
| | | | | | | |
| Mode 2 |  |  |  |  |  | $\times 10 \frac{rad}{s}$ Max  Min |
| Deformation Scale: | Max: 22,15 Min: 0,00 0,002 | Max: 22,19 Min: 0,00 0,002 | Max: 22,16 Min: 0,00 0,002 | Max: 21,80 Min: 0,00 0,002 | Max: 20,27 Min: 0,00 0,002 | |
| | | | | | | |
| Mode 3 |  |  |  |  |  | $\times 10 \frac{rad}{s}$ Max  Min |
| Deformation Scale: | Max: 26,54 Min: 0,00 -0,001 | Max: 26,64 Min: 0,00 0,001 | Max: 26,25 Min: 0,00 0,001 | Max: 26,95 Min: 0,00 0,001 | Max: 25,66 Min: 0,00 0,001 | |
| | | | | | | |

Table 6.25 - Parameterized von Mises effective stress field of natural vibrational modes 1-3 usig NRPIM: 2D shell-like convergence study.

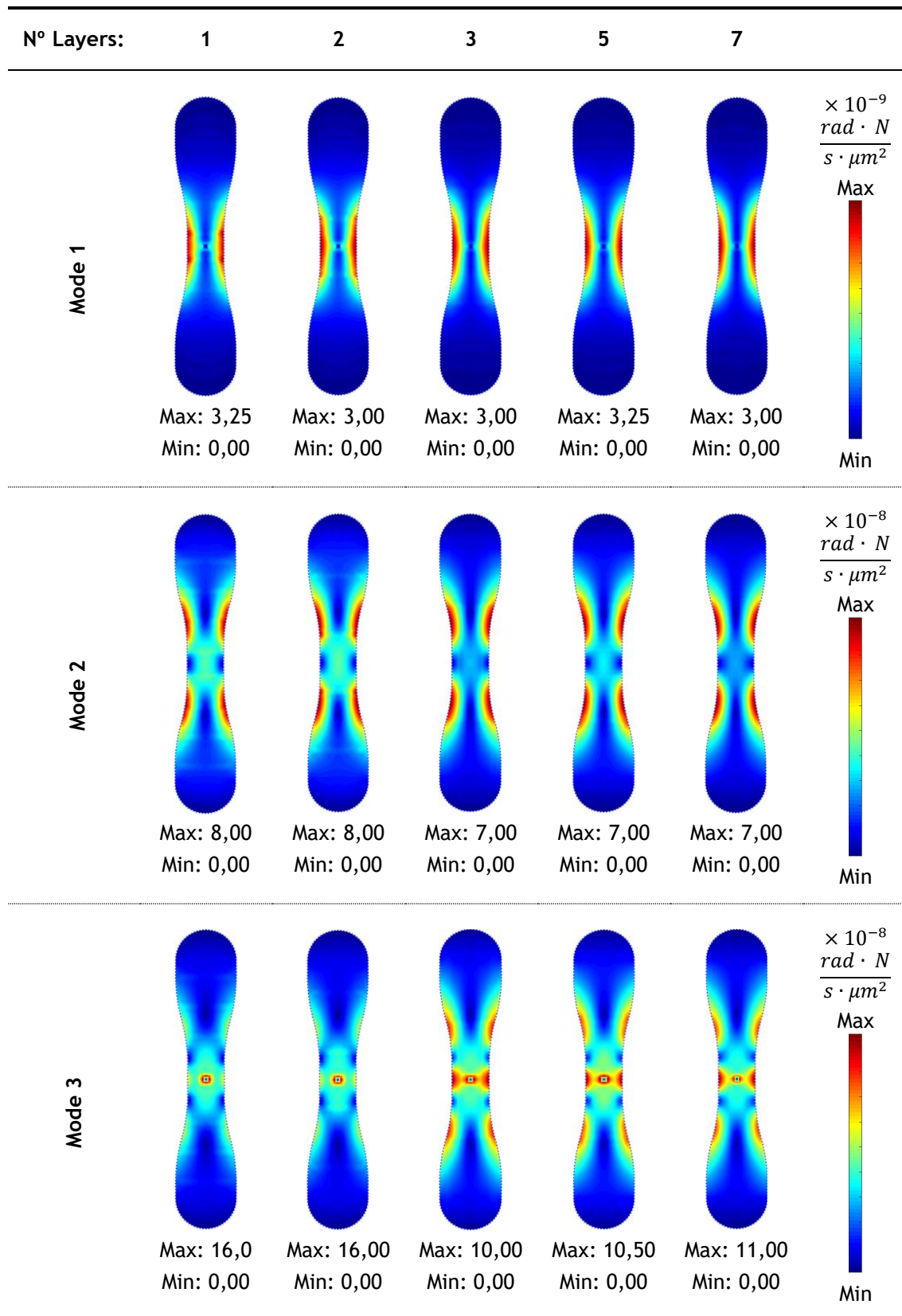
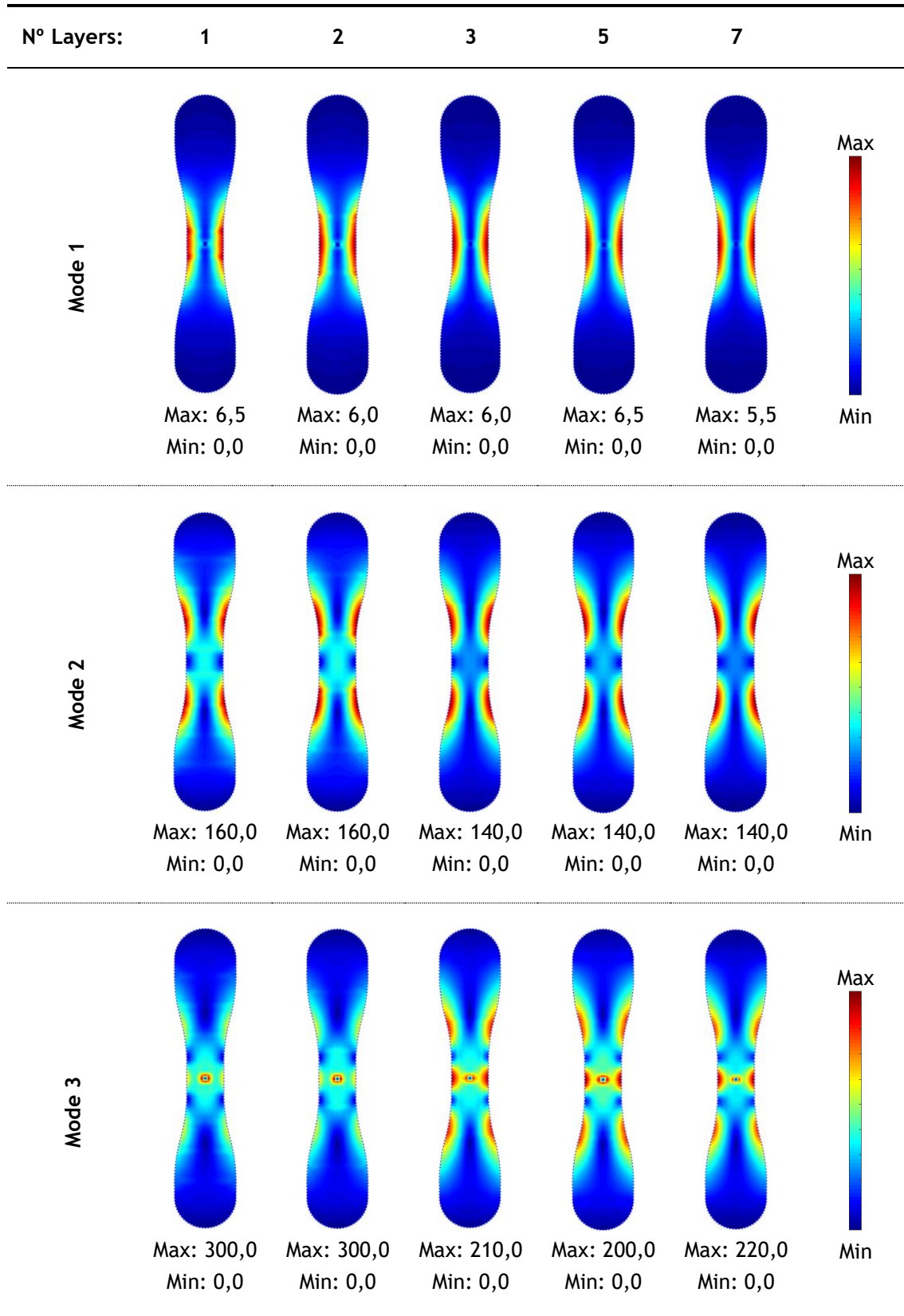


Table 6.26 - Parameterized equivalent effective strain field of natural vibrational modes 1-3 usig NNRPIM: 2D shell-like convergence study.



6.3.3 - Bending Test

Compared to the bending test performed in Sec. 6.2 - , since no significant advantage was found in using several layers with different thicknesses, the only change in this simulation is in the value used to define the thickness of the “artificial” chromosome. In Sec. 6.2 - it was defined as being $1,0 \mu m$ thick and in this case was used the mentioned in Table 6.14 for a single layer model.

Since the loads and properties of the material have been transversal to all simulations, using Eq. (6.2) and Eq. (4.54), it is possible to establish the following relations:

$$A_1\sigma_1 = A_2\sigma_2 \quad (6.4)$$

and

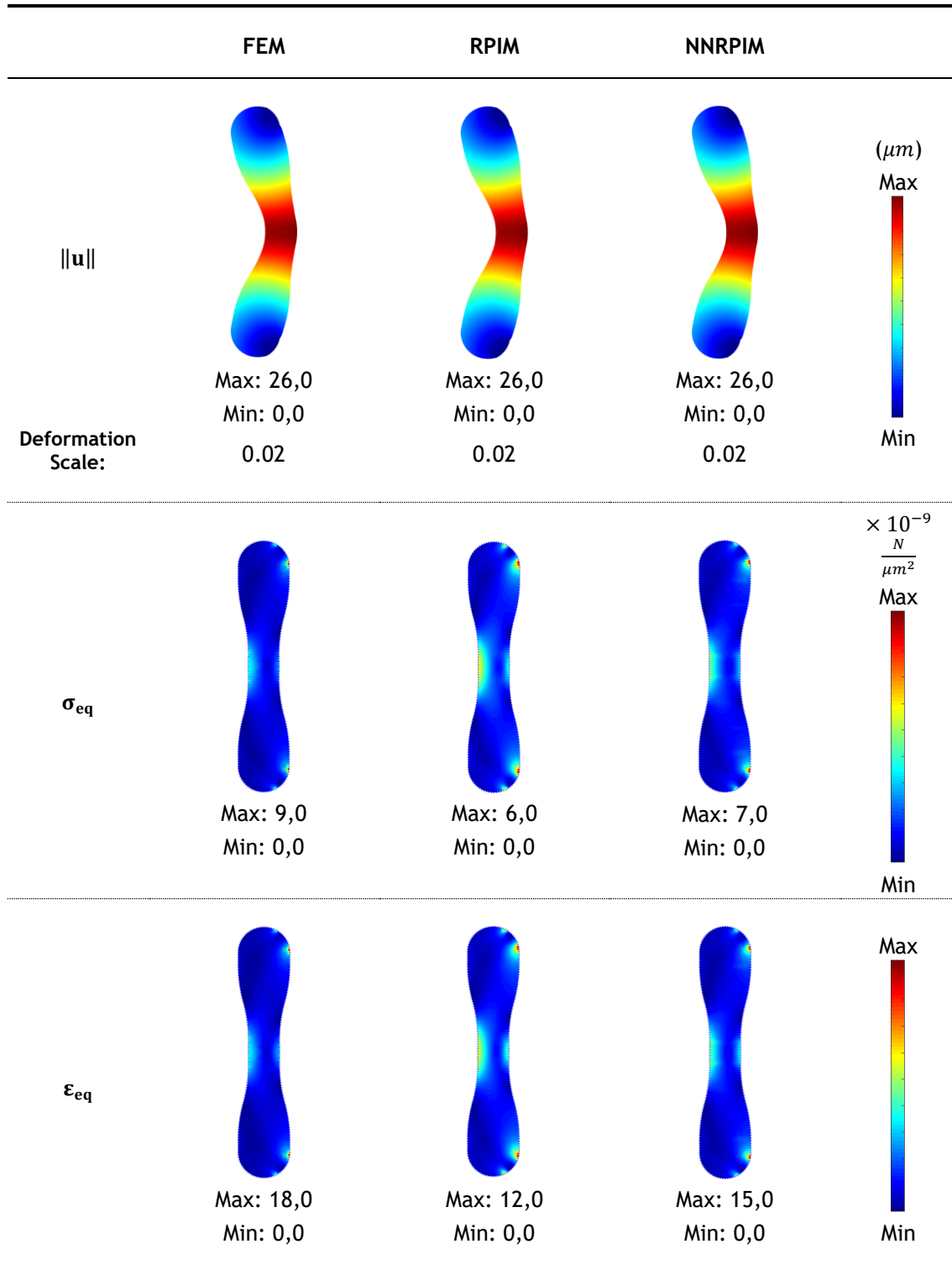
$$A_1\varepsilon_1 = A_2\varepsilon_2 \quad (6.5)$$

which are verified and allows to establish comparisons between 2D models with different thicknesses and also between 2D and 3D models.

As stated before, this type of simulation can elucidate us about chromosomes response to pulling forces when pulled by the fibers of the achromatic spindle (in cell division) with the cytoplasm opposition, but further studies on the interaction of the genetic material with the surrounding fluid with the very fibers exerting the tensile forces and the way chromatin interacts itself and divides.

In Table 6.27 are presented the displacement, von Mises effective strain and equivalent effective strain fields which were obtained using FEM and the meshless methods RPIM and NNRPIM.

Table 6.27 - Bending test with one layer model



6.4 - 3D Model

The 3D model was constructed following the dimensions described in Figure 6.1 being constituted with 1268 nodes. The smaller cross-section area is $A_{eq1} = \pi \times 0,3^2 \approx 0,283 \mu m^2$ and the largest cross-section area is $A_{eq2} = \pi \times 0,5^2 \approx 0,785 \mu m^2$. It was performed a stress-strain assay, a free vibration study and also a bending test. It is then possible to compare with 2D models and conclude about the convergence between 2D and 3D models.

6.4.1 - Stress-strain

In Table 6.28 is presented the Cauchy strain in the neck region obtained for the tri-dimensional model of an “artificial” chromosome using the three numerical methods tested.

Table 6.28 - Displacement in neck region in 3D model

| FEM | RPIM | NNRPIM |
|------|------|--------|
| 2,61 | 2,70 | 2,63 |

The obtained strains are similar between the different methods but much higher than those obtained previously for the bi-dimensional models. These differences are, however, expected and through the Eq. (6.5) it is possible to relate the results. Using the strain values obtained for the 3D model, the expected strains were calculated for each one of the previous cases, that is, for the model with higher nodal density in Sec. 6.2 - and also for models with different number of layers, Sec. 6.3 - . These comparative studies are shown in Table 6.29 and Table 6.30 respectively.

In most of the cases, the error between the predicted deformation and the measured is small and, therefore, the differences in results between the different models can be mostly attributed to the better or worse representation that is made of the thickness of the chromosome over its entire length. Since the results are directly affected by this characteristic and it is not possible to faithfully reproduce the problem in two dimensions, preference is given to the use of three-dimensional models. The extension of these conclusions to “real” chromosome models, however, needs to be confirmed given the restrictions and simplifications of the models used as mentioned above in Sec. 6.3.1 - .

In Table 6.31 are displayed the displacement, von Mises effective stress and equivalent effective strain fields for the stress-strain experiment for the 3D model.

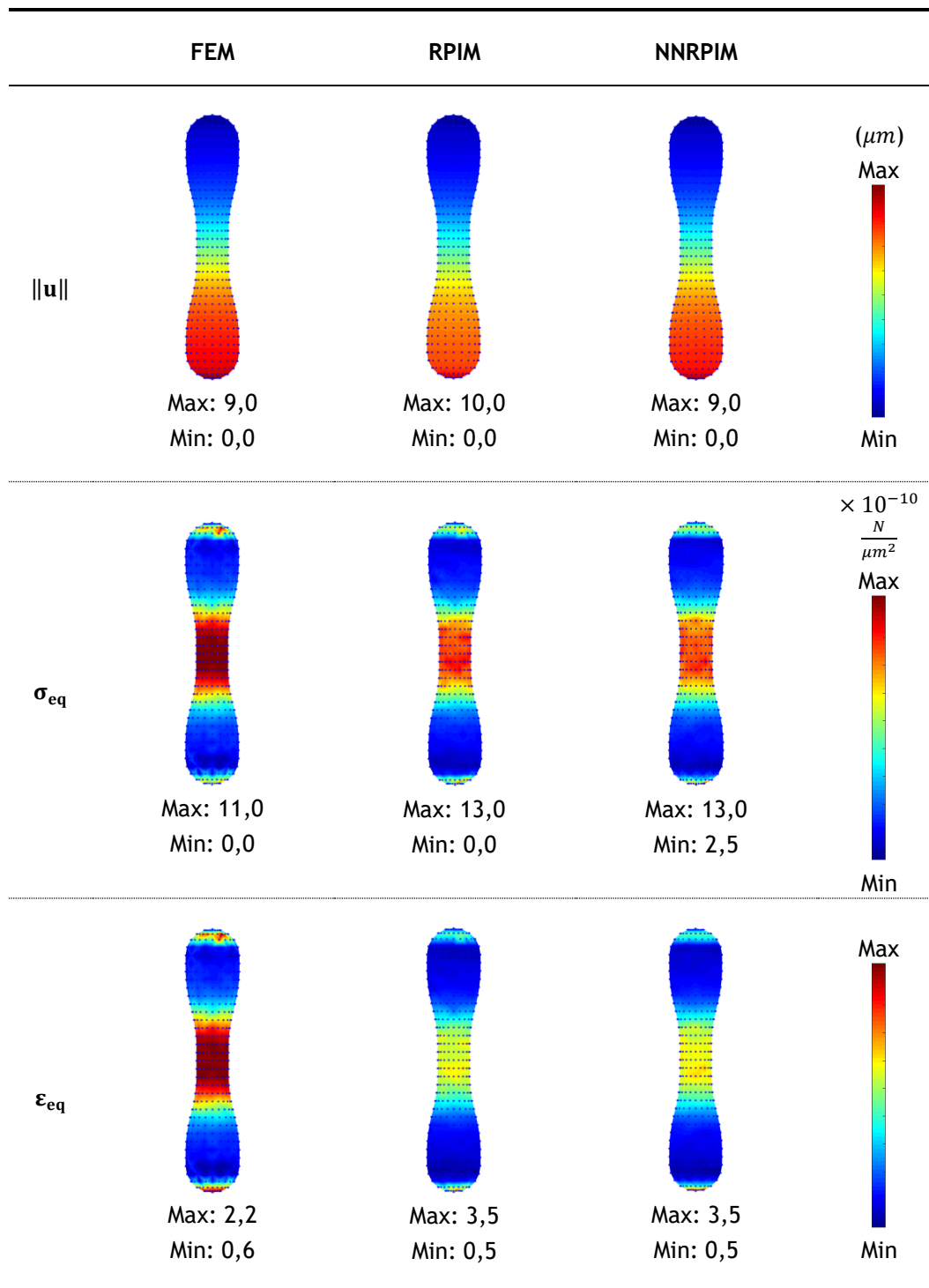
Table 6.29 - Comparative study of displacement in neck region between 3D model and 2D model with 1741 nodes model from Sec. 6.2.1 - .

| A_{eq1} μm^2 | Predicted based on 3D | | | Measured | | | Error % | | |
|------------------------|-----------------------|------|--------|----------|------|--------|---------|------|--------|
| | FEM | RPIM | NNRPIM | FEM | RPIM | NNRPIM | FEM | RPIM | NNRPIM |
| 0,600 | 1,23 | 1,27 | 1,24 | 1,22 | 1,33 | 1,24 | 0,6 | 4,8 | 0,1 |

Table 6.30 - Comparative study of displacement in neck region between 3D model and 2D models from Sec. 6.2.1 -

| N° Layers | A_{eq1} μm^2 | Predicted based on 3D | | | Measured | | | Error % | | |
|--------------|------------------------|-----------------------|------|--------|----------|------|--------|---------|------|--------|
| | | FEM | RPIM | NNRPIM | FEM | RPIM | NNRPIM | FEM | RPIM | NNRPIM |
| 1 | 0,371 | 1,99 | 2,06 | 2,00 | 1,98 | 2,16 | 1,94 | 0,6 | 5,1 | 3,0 |
| 2 | 0,426 | 1,73 | 1,79 | 1,74 | 1,73 | 1,79 | 1,60 | 0,2 | 0,1 | 8,0 |
| 3 | 0,467 | 1,58 | 1,64 | 1,59 | 1,58 | 1,83 | 1,59 | 0,0 | 11,8 | 0,1 |
| 5 | 0,469 | 1,58 | 1,63 | 1,58 | 1,56 | 1,59 | 1,40 | 0,7 | 2,5 | 11,4 |
| 7 | 0,470 | 1,57 | 1,63 | 1,58 | 1,58 | 1,84 | 1,62 | 0,4 | 13,0 | 2,7 |

Table 6.31 - Stress-strain curve simulation using 3D “artificial” chromosome



6.4.2 - Free-Vibrations

Table 6.32 - 3D "artificial" chromosome natural vibration frequencies for modes 1-3

| | Mode 1 | Mode 2 | Mode 3 |
|---------------|--------|--------|--------|
| FEM | 32,36 | 192,86 | 250,12 |
| | 32,83 | 205,90 | 252,57 |
| | - | 220,15 | - |
| RPIM | 30,45 | 176,35 | 230,01 |
| | 30,91 | 194,10 | 232,17 |
| | - | 201,37 | - |
| NNRPIM | 30,36 | 169,64 | 228,07 |
| | 30,81 | 195,22 | 229,64 |
| | - | 199,55 | - |

The natural vibration frequencies for the first three modes are presented in Table 6.32. Since a three-dimensional model is now being evaluated, it is possible to find more than one natural vibration frequency corresponding to the same mode. For a same mode, the frequencies found must be close to each other and correspond to the fact that a body can vibrate in different directions and orientations but always has the same characteristic deformation field. For a more exhaustive comparative study, Table 6.33, Table 6.36 and Table 6.39 show the parameterized displacement field obtained using FEM, RPIM and NNRPIM respectively; In Table 6.34, Table 6.37 and Table 6.40 are presented the parameterized von Mises effective stress field of natural vibrational modes 1-3 using FEM, RPIM and NNRPIM; And for last, in Table 6.35, Table 6.38 and Table 6.41 are shown the parameterized equivalent effective strain.

Considering all the studies of free vibrations performed it is verified that there is an inter-model proximity between the vibration frequencies of each of the three modes. The variation of results with respect to the vibration modes is not significant and therefore, once already assured that this type of numerical methods is applicable to this type of microstructures it is safe to proceed to a more detailed study of the natural vibration modes of human chromosomes.

Table 6.33 - Parameterized displacement field of natural vibrational modes 1-3 using FEM: 3D model

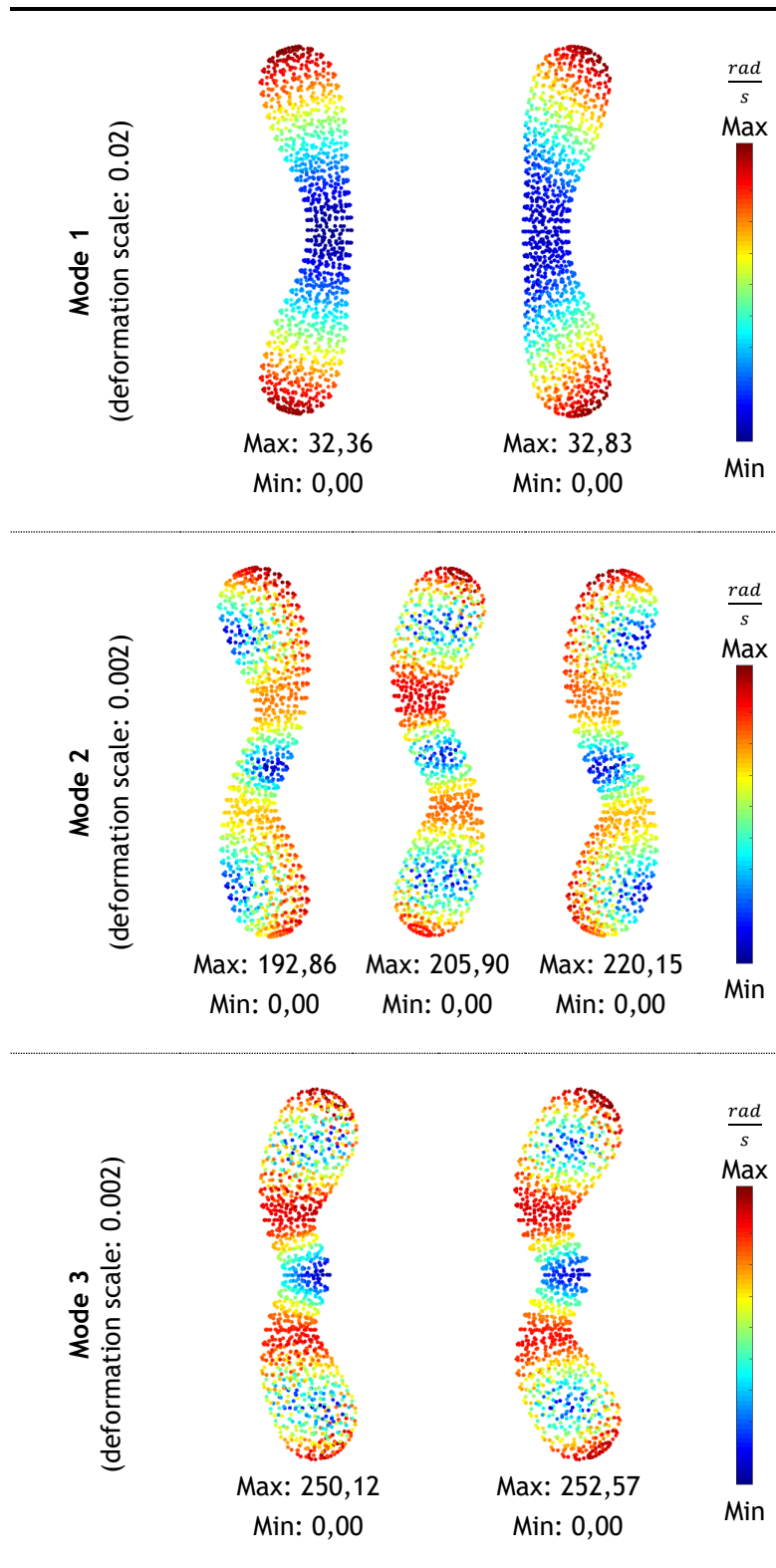


Table 6.34 - Parameterized von Mises effective stress field of natural vibrational modes 1-3 usig FEM: 3D model

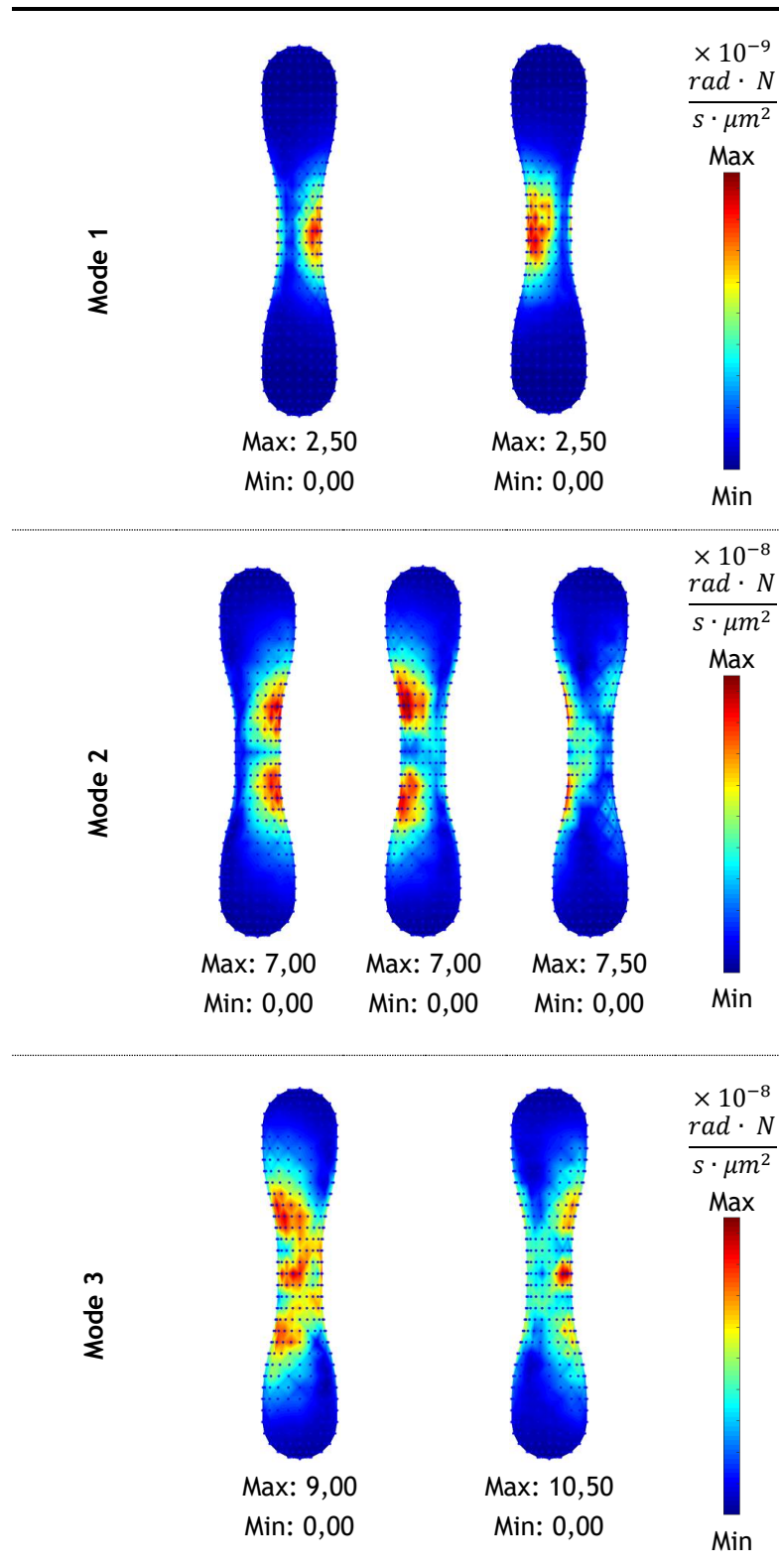


Table 6.35 - Parameterized equivalent effective strain field of natural vibrational modes 1-3 usig FEM: 3D model

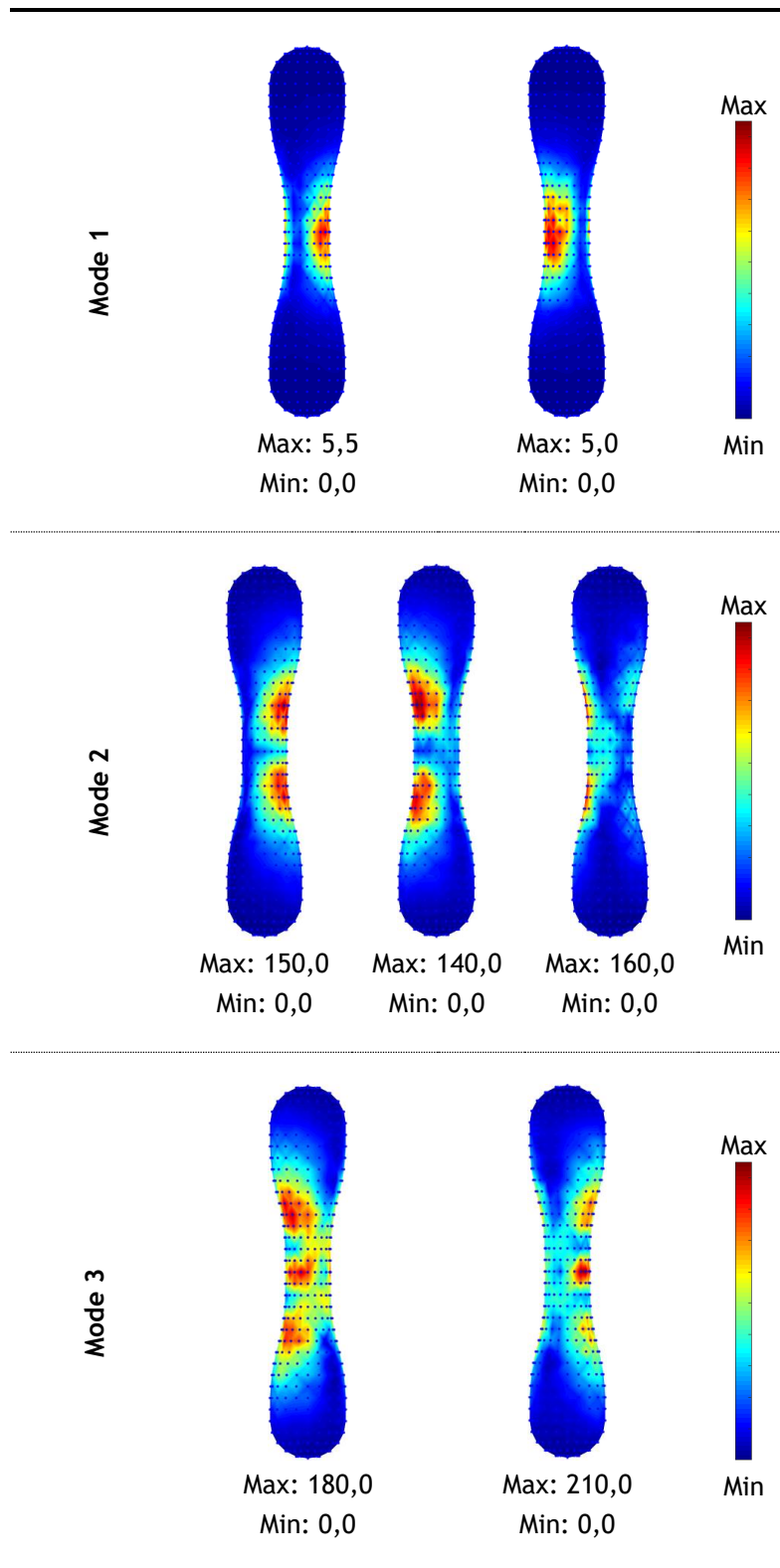


Table 6.36 - Parameterized displacement field of natural vibrational modes 1-3 usig RPIM: 3D model

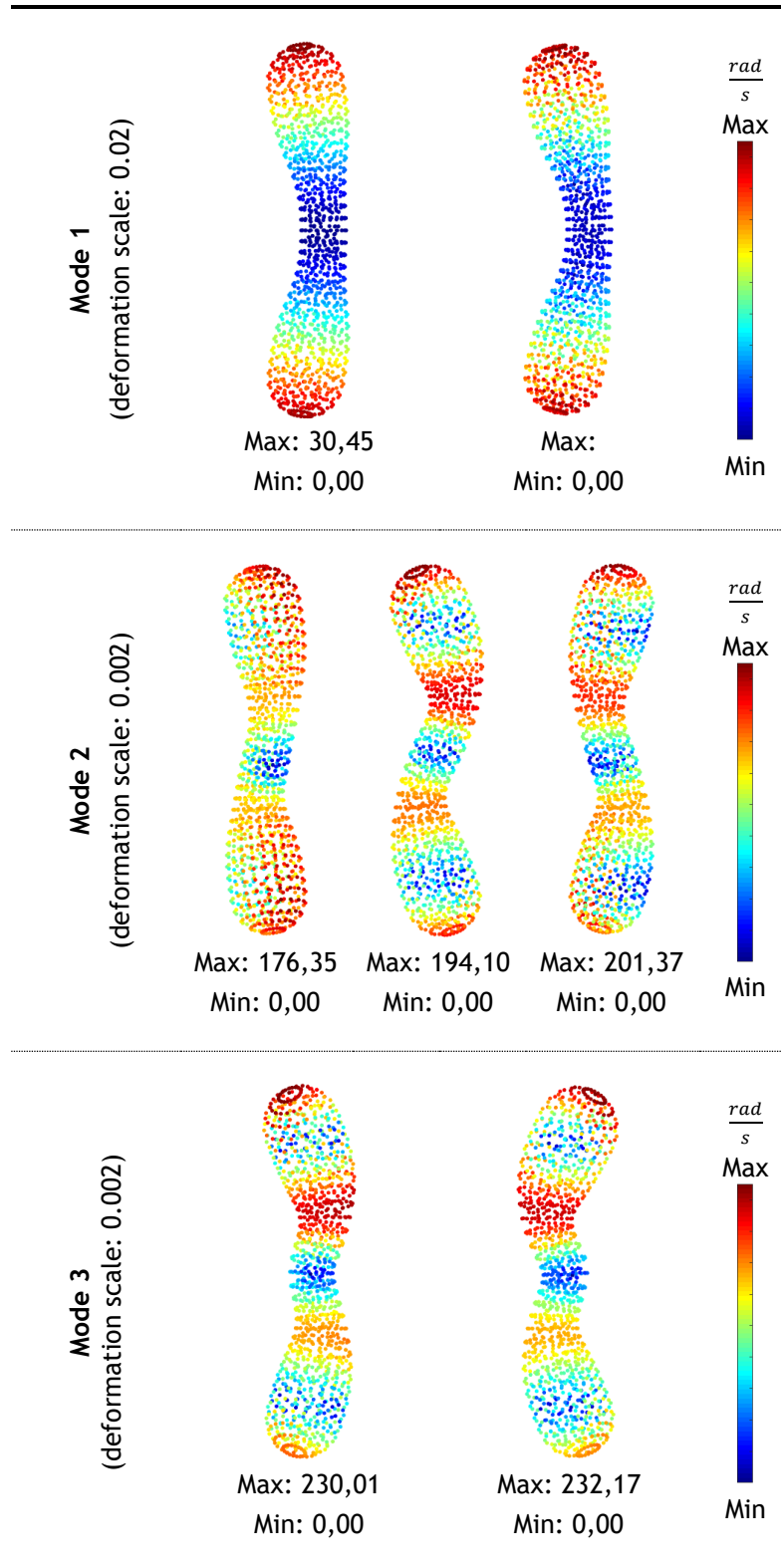


Table 6.37 - Parameterized von Mises effective stress field of natural vibrational modes 1-3 usig RPIM: 3D model

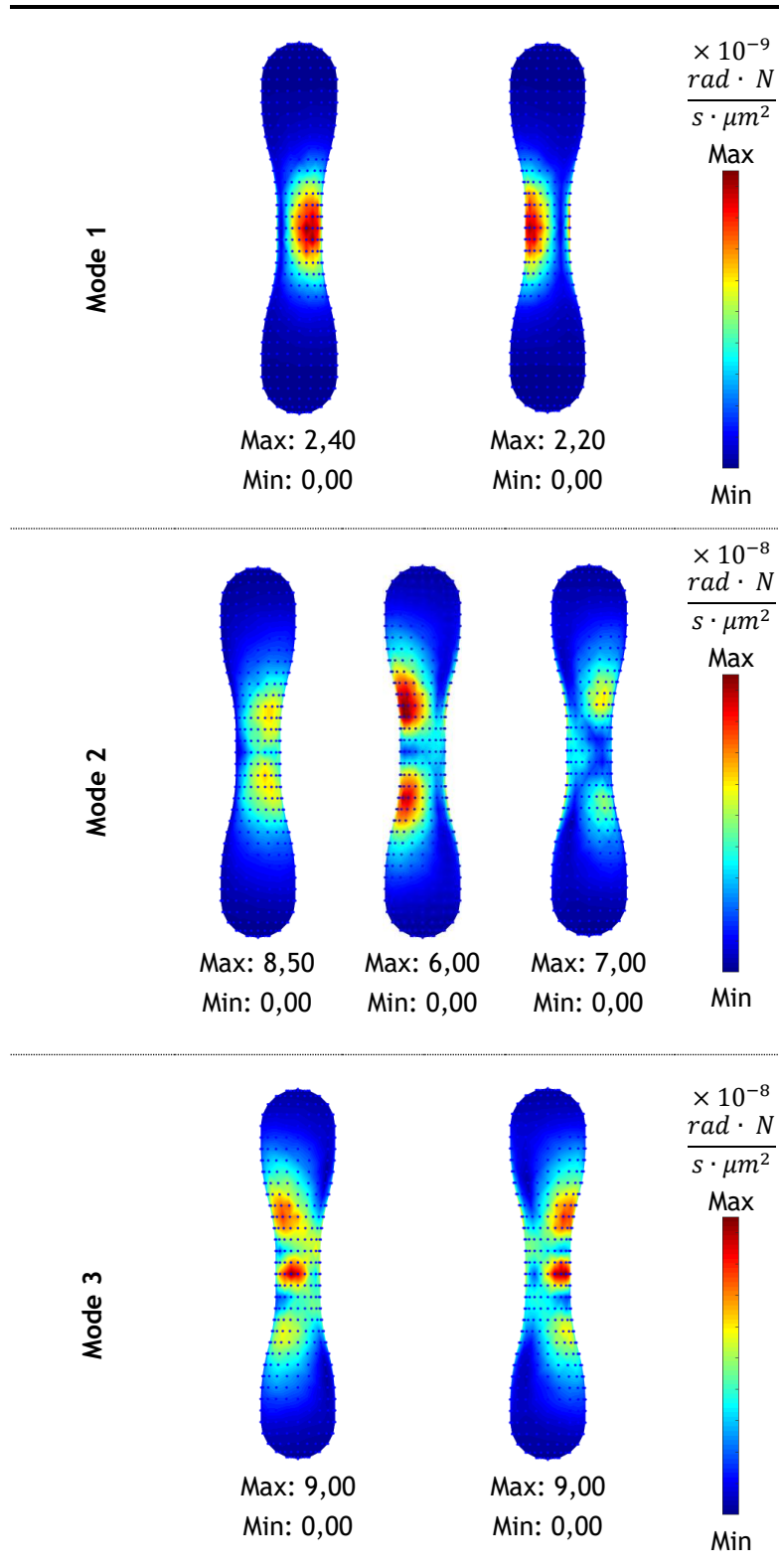


Table 6.38 - Parameterized equivalent effective strain field of natural vibrational modes 1-3 usig RPIM: 3D model

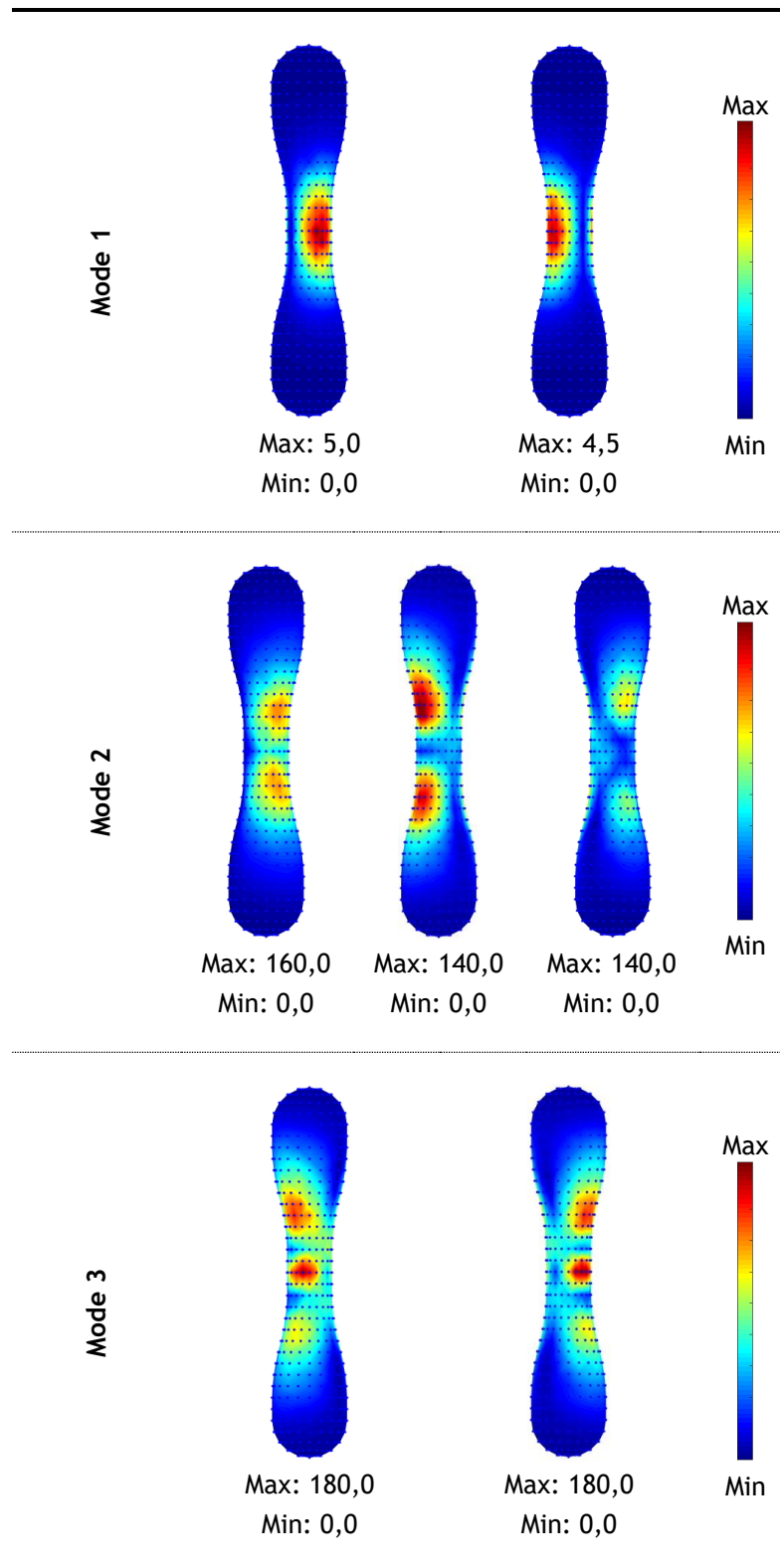


Table 6.39 - Parameterized displacement field of natural vibrational modes 1-3 usig NNRPIM: 3D model

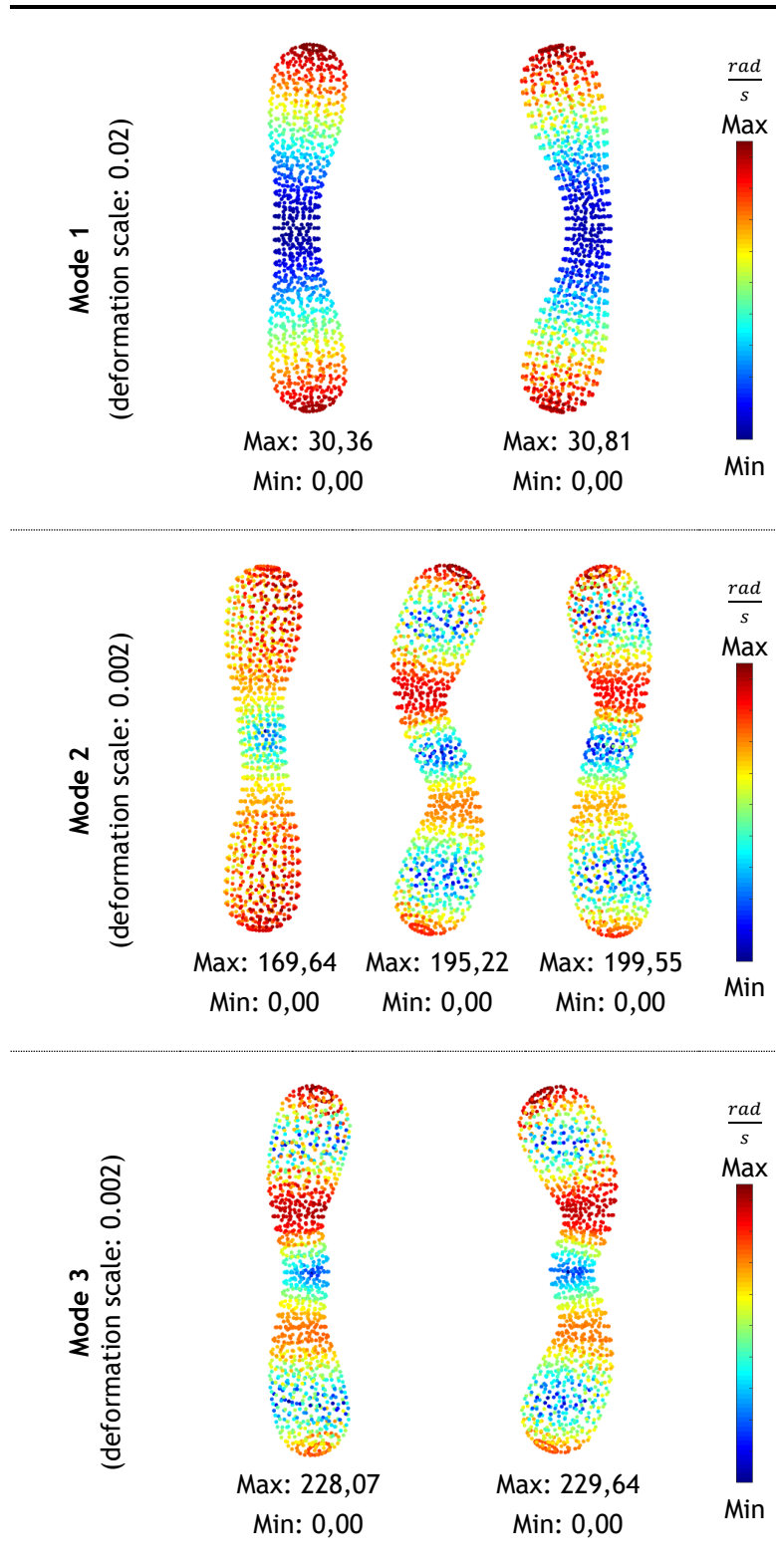


Table 6.40 - Parameterized von Mises effective stress field of natural vibrational modes 1-3 usig NNRPIM: 3D model

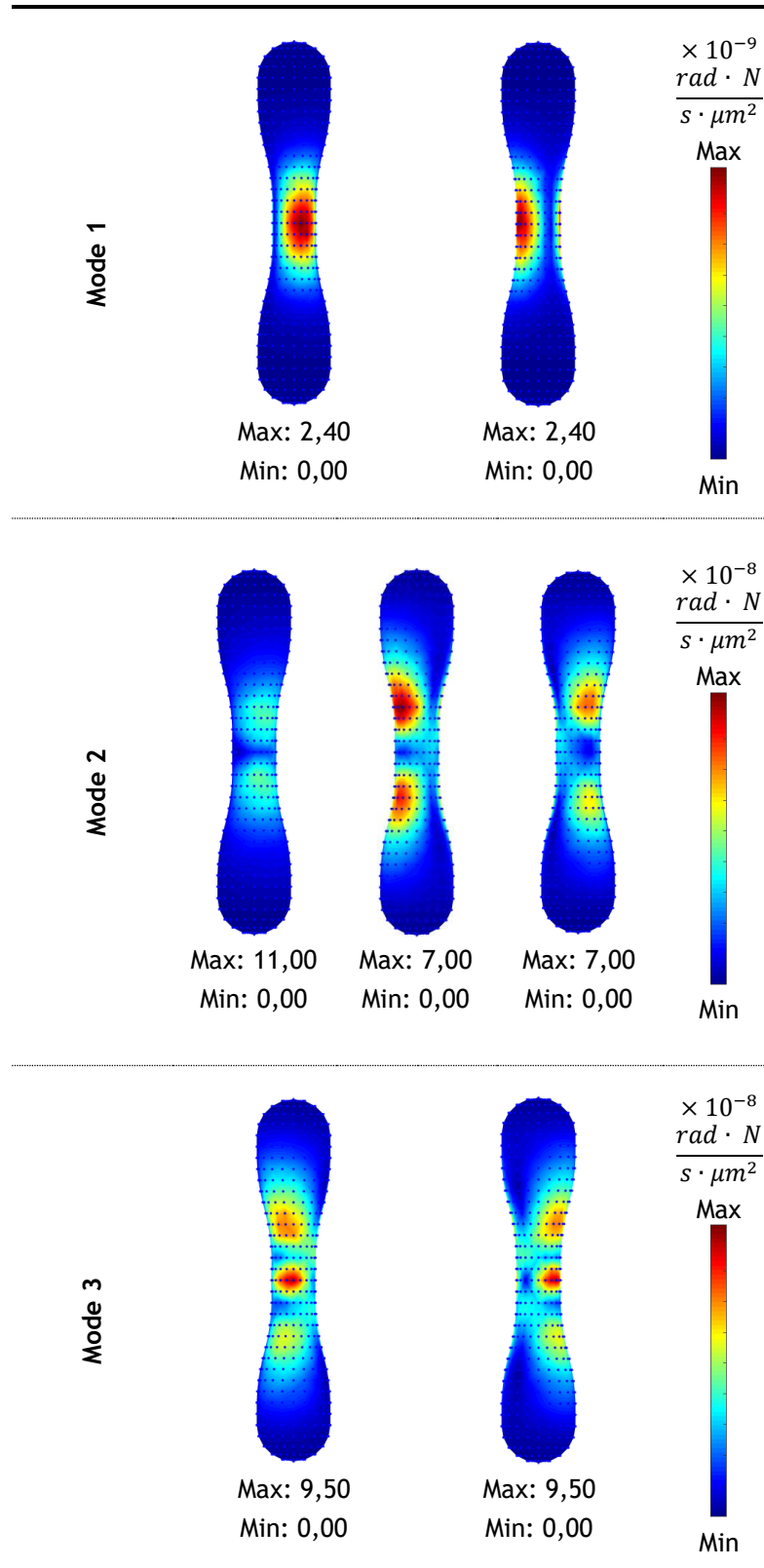
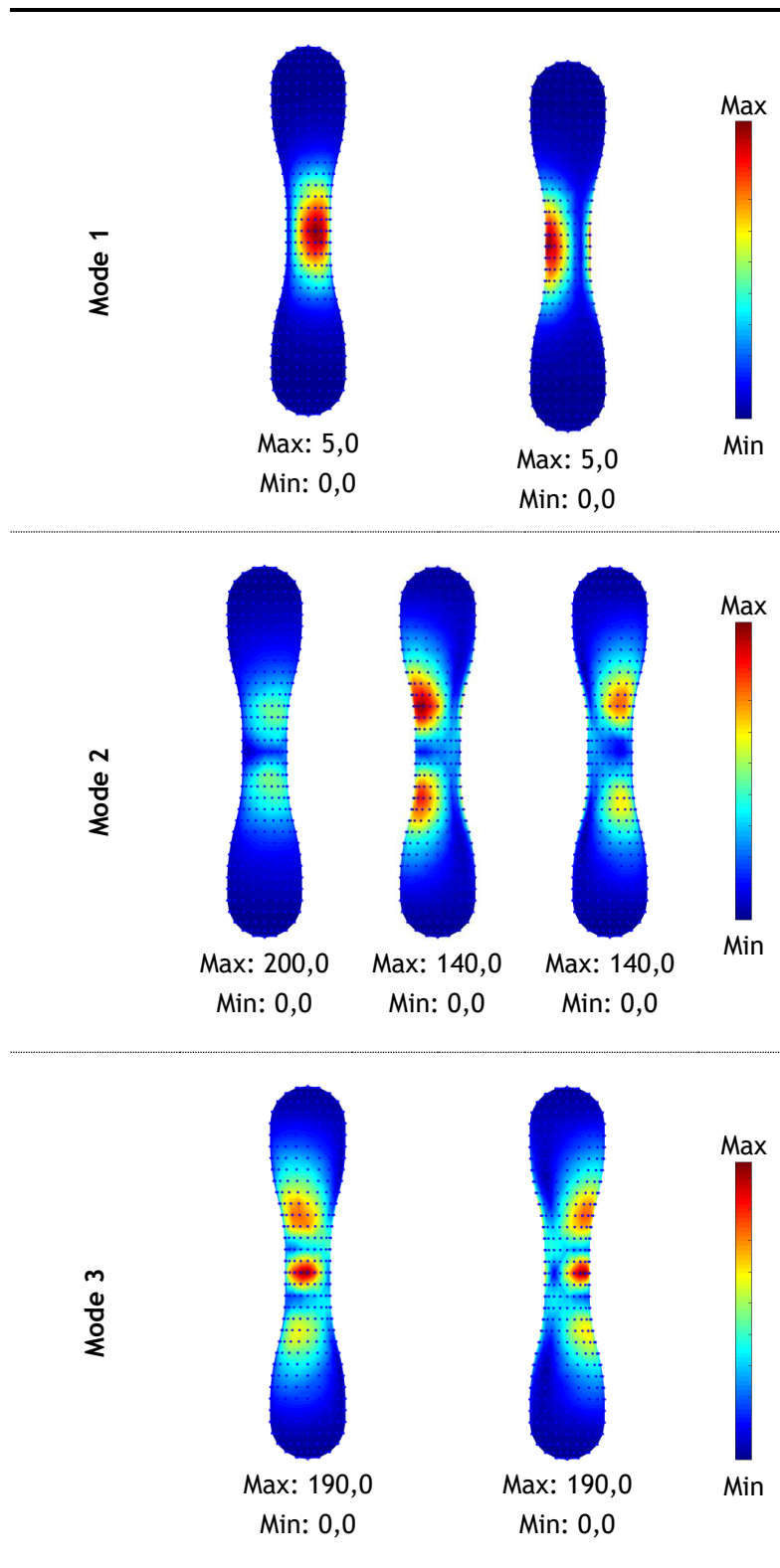


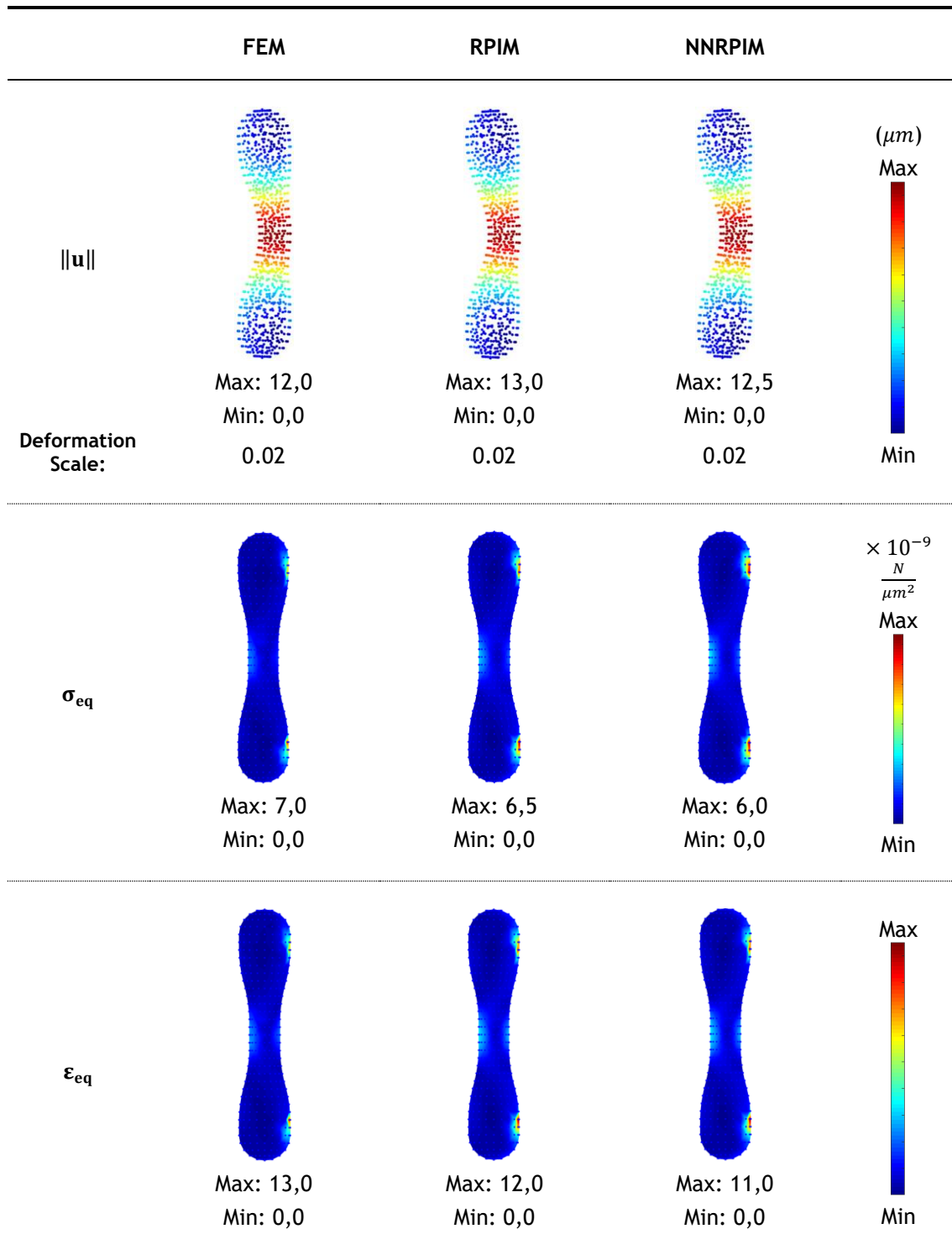
Table 6.41 - Parameterized equivalent effective strain field of natural vibrational modes 1-3 usig NNRPIM: 3D model



6.4.3 - Bending Test

In Table 6.42 are presented the displacement, von Mises effective strain and equivalent effective strain fields which were obtained using FEM and the meshless methods RPIM and NNRPIM for bending assay of the tridimensional model.

Table 6.42 - 3D “artificial” chromosome bending test



Chapter 7

Human Chromosomes

After the convergence studies, two-dimensional and three-dimensional models of three different human chromosomes, chromosomes 2, 10 and 12, were constructed in order to evaluate their free vibration modes. The construction of the models was carried out in accordance with the principles set out in Sec. 5.1 - and the nodal distribution of each of the models is described in Table 7.1.

In the Table 7.2 are synthesized all the results for all the chromosomes tested, for the 2D and 3D approaches using the different numerical methods. The parameterized displacement, von Mises effective stress and equivalent effective strain fields for 2D cases are presented from Table 7.3 to Table 7.11 and for 3D cases from Table 7.12 to Table 7.20.

Attending in Table 7.2 and comparing 2D and 3D approaches very similar values were obtained and the greatest difference of results was obtained for chromosome number 2 in the third mode of vibration.

Comparing the numerical methods used it is possible to conclude that (in percentage terms) the higher differences occur for the first mode of vibration, however, in terms of absolute difference, it increases to higher frequencies. The results are also closer between the meshless methods than each of them and the FEM. In spite of the variability of results between methods and the sometimes considerable difference between frequencies of the same vibration mode, it is possible to use the results of different methods to establish for the chromosome an approximate value for the first, second and third natural frequency. This analysis to define the frequency ranges of each of the modes and for each chromosome was performed using only the results for the three-dimensional models and can be found in Figure 7.1, where are also defined the mean values and respective standard deviations.

By organizing the results in this way, Figure 7.1, and without distinction of the numerical method used to obtain them, it is evident the greater dispersion of results for the third mode of vibration of chromosome 2 and also for mode 2 of chromosomes 10 and 12. Despite this dispersion and the frequency ranges, defined through this organization of the data, between different modes and chromosomes, it is still possible to identify characteristic traits of each of the chromosomes. Thus, it is possible to define narrower ranges of frequencies (specially the first natural frequency) and/or to select certain modes of vibration that only identify a particular chromosome.

Table 7.1 - 2D and 3D human chromosomes number 2, 10 and 12 models with nodal distribution.

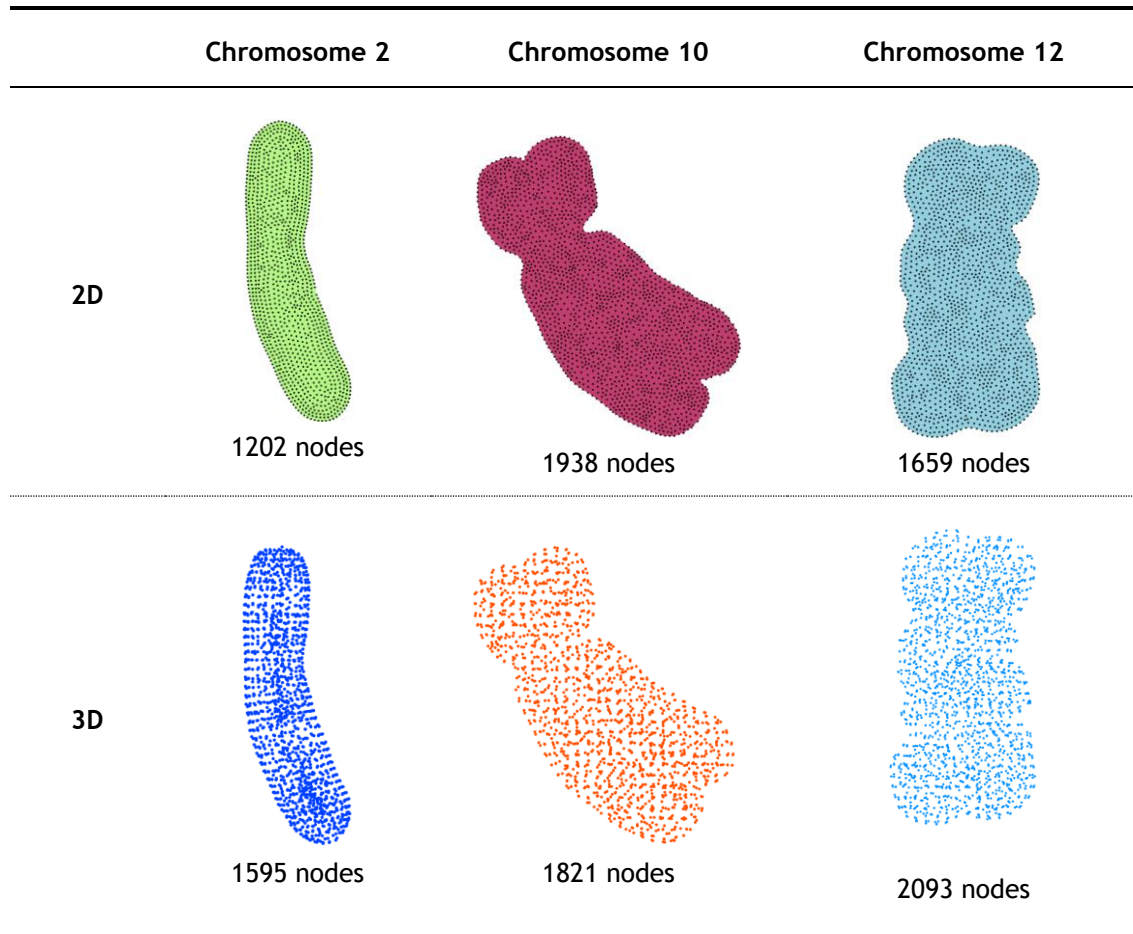


Table 7.2 - Natural frequencies of modes 1-3 for chromosomes number 2, 10 and 12

| | | FEM (rad/s) | | | RPIM (rad/s) | | | NNRPIM (rad/s) | | |
|----|----|-------------|--------|--------|--------------|--------|--------|----------------|--------|--------|
| | | Mode1 | Mode2 | Mode3 | Mode1 | Mode2 | Mode3 | Mode1 | Mode2 | Mode3 |
| 2D | 2 | 70,62 | 266,84 | 313,43 | 70,03 | 262,97 | 310,24 | 70,68 | 263,18 | 309,92 |
| | 10 | 105,37 | 221,74 | 449,98 | 103,71 | 215,16 | 431,53 | 103,81 | 212,67 | 426,25 |
| | 12 | 194,37 | 534,94 | 654,97 | 188,09 | 520,85 | 649,84 | 191,24 | 524,89 | 650,36 |
| 3D | 2 | 73,09 | 250,38 | 569,90 | 128,59 | 265,97 | 457,19 | 88,20 | 265,55 | 445,83 |
| | | 83,08 | 259,12 | 583,65 | 135,05 | 272,15 | 476,79 | 100,21 | 272,26 | 474,54 |
| | 10 | 62,72 | 152,38 | 426,59 | 54,32 | 137,22 | 389,42 | 55,56 | 137,20 | 394,28 |
| | | 102,77 | 205,64 | 457,42 | 96,44 | 191,44 | 418,07 | 97,33 | 185,45 | 425,73 |
| | 12 | 124,56 | 421,35 | 613,29 | 115,00 | 378,14 | 570,83 | 114,25 | 374,86 | 577,94 |
| | | 159,76 | 496,22 | 619,25 | 137,80 | 457,48 | 592,27 | 126,49 | 450,76 | 597,52 |

These results point out that it is possible to identify different chromosomes through the first natural vibration frequencies, however, more research is required. The identification of the modes of vibration has not always been easy and its visual distinction is sometimes difficult, and the variation of the frequencies that characterize each mode may have been greater because of this fact, which should be evaluated in greater depth.

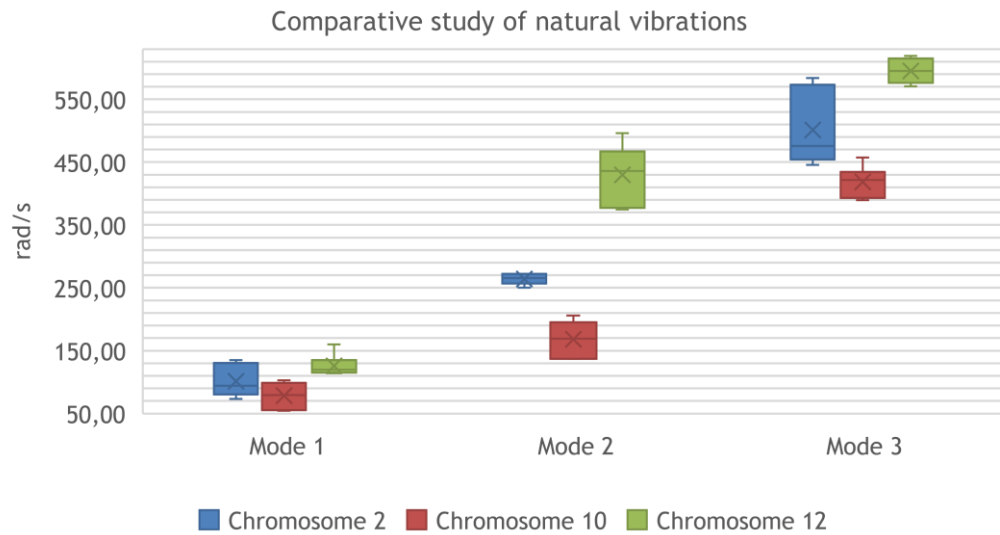


Figure 7.1 - Comparative study of the first 3 natural frequencies of chromosomes 3D models

Table 7.3 - Parameterized displacement field of natural vibrational modes 1-3 using FEM for 3 different 2D human chromosome models.

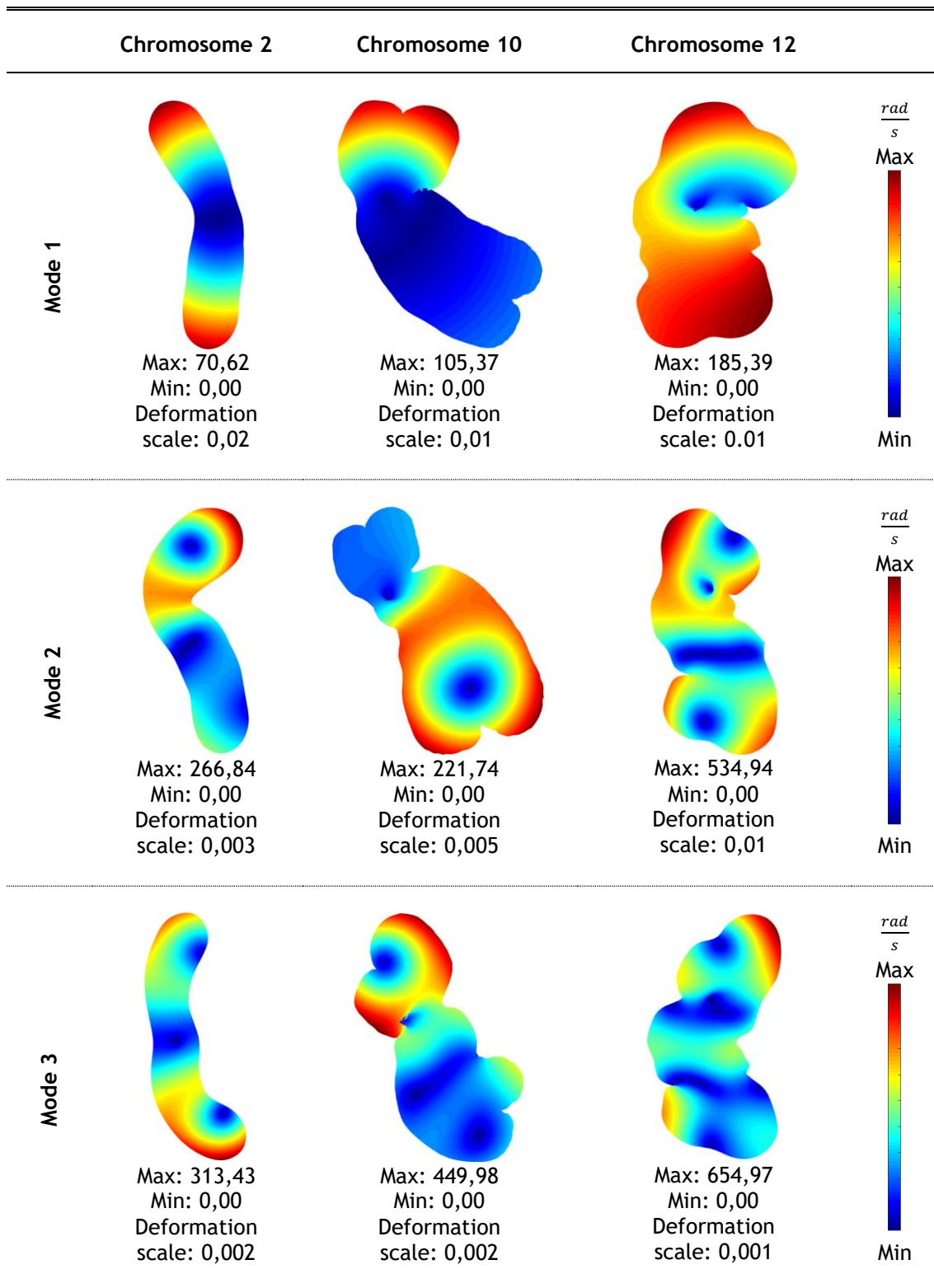


Table 7.4 - Parameterized von Mises effective stress field of natural vibrational modes 1-3 using FEM for 3 different 2D human chromosome models.

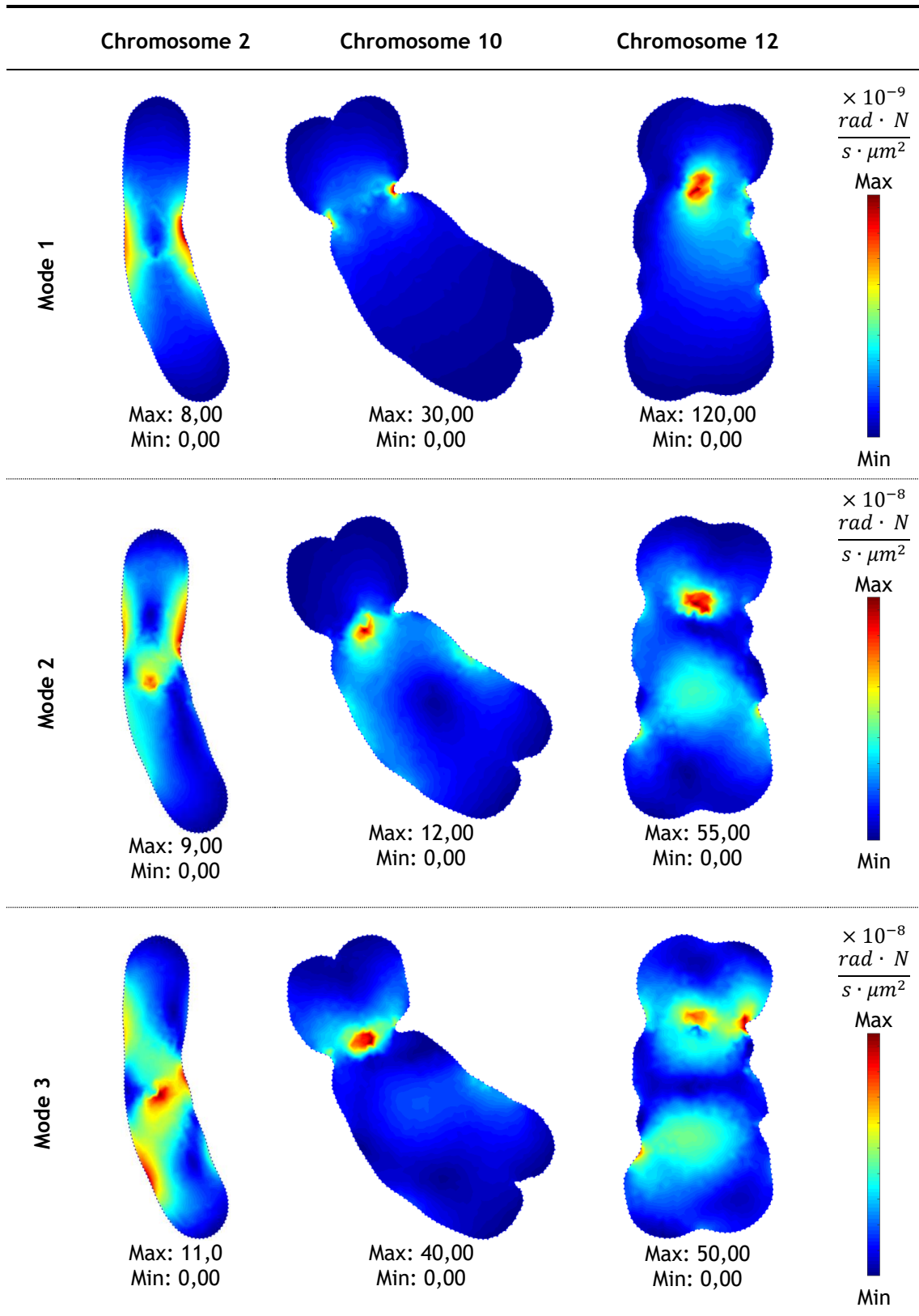


Table 7.5 - Parameterized equivalent effective strain field of natural vibrational modes 1-3 using FEM for 3 different 2D human chromosome models.

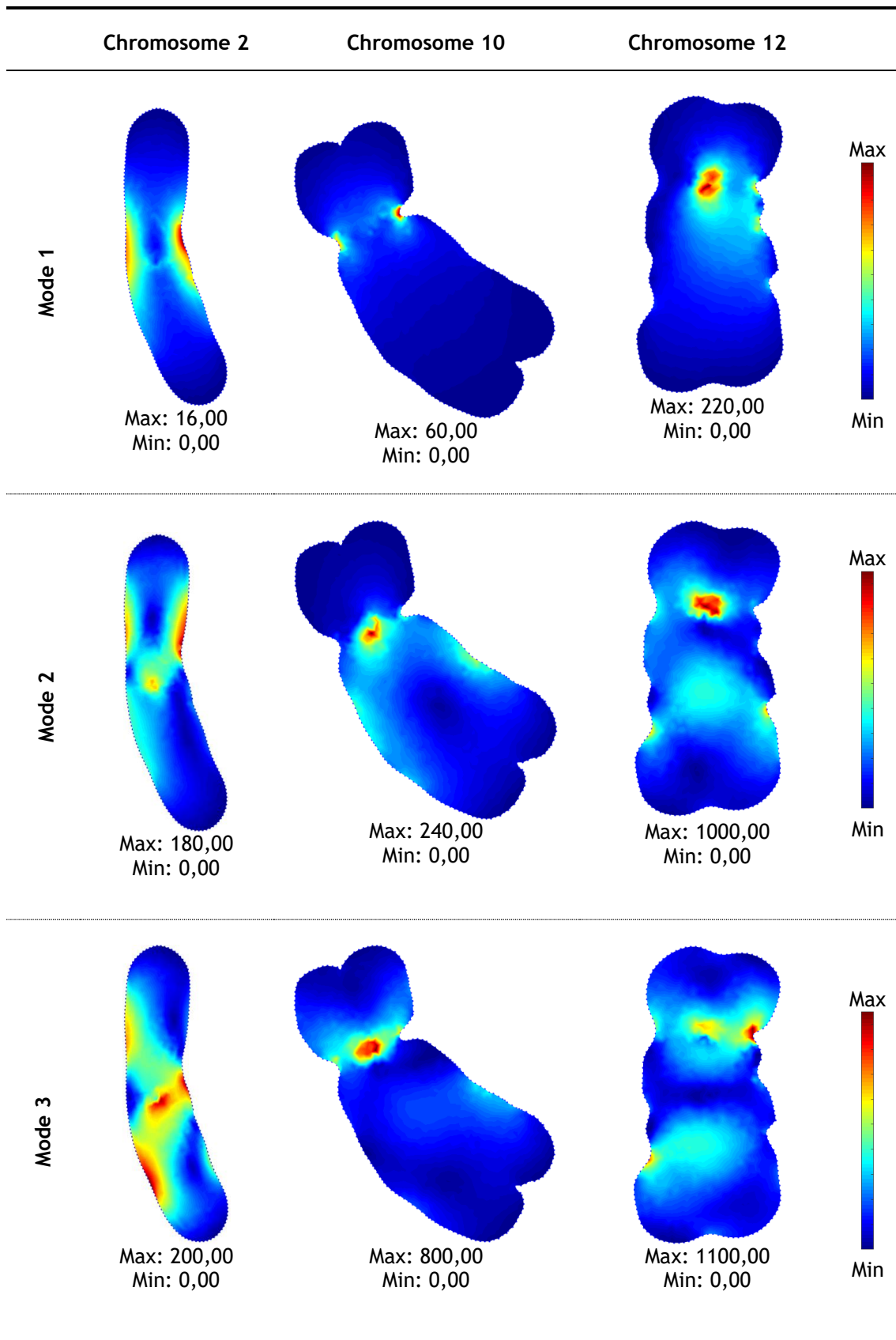


Table 7.6 - Parameterized displacement field of natural vibrational modes 1-3 using RPIM for 3 different 2D human chromosome models.

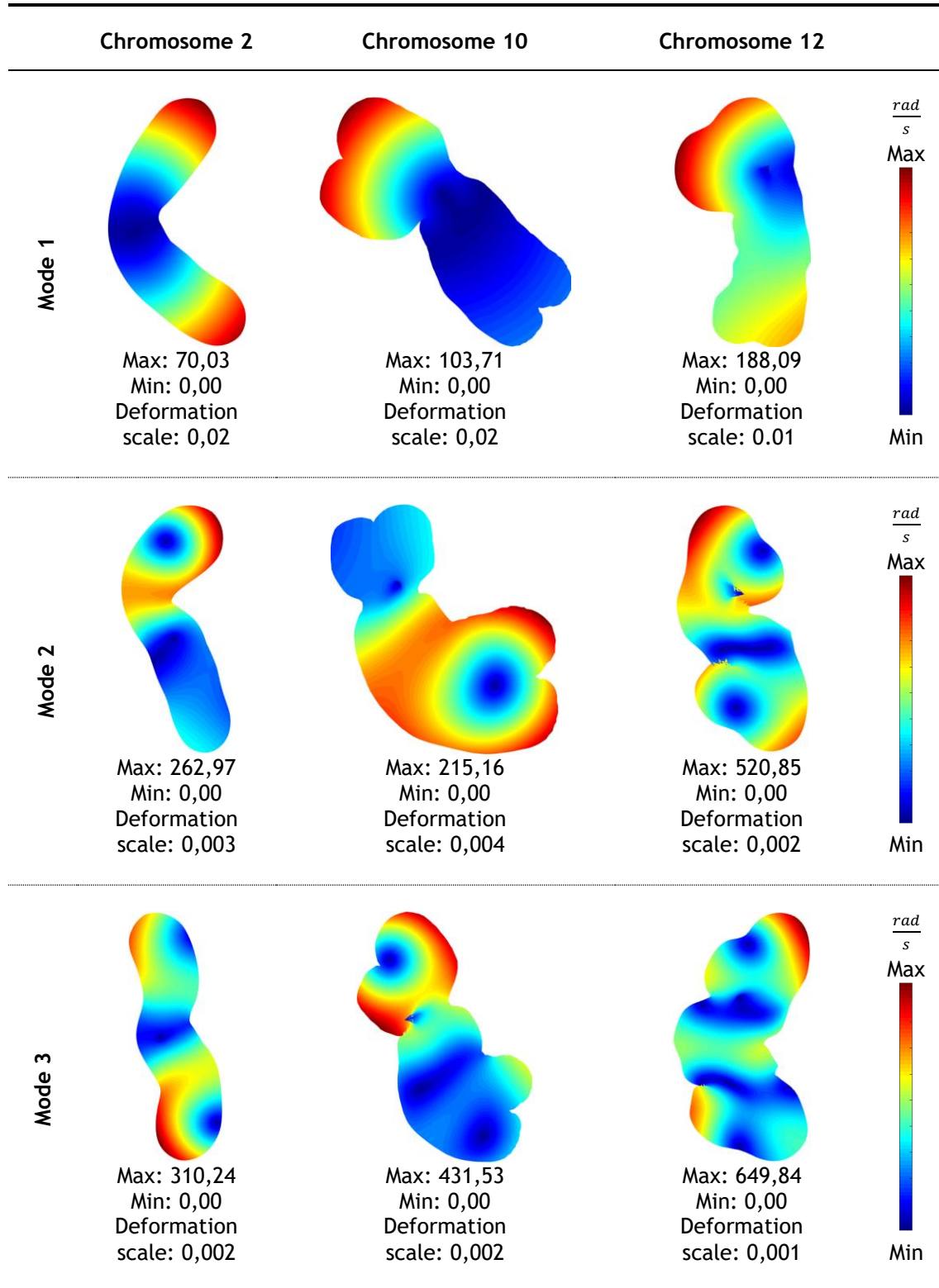


Table 7.7 - Parameterized von Mises effective stress field of natural vibrational modes 1-3 using RPIM for 3 different 2D human chromosome models.

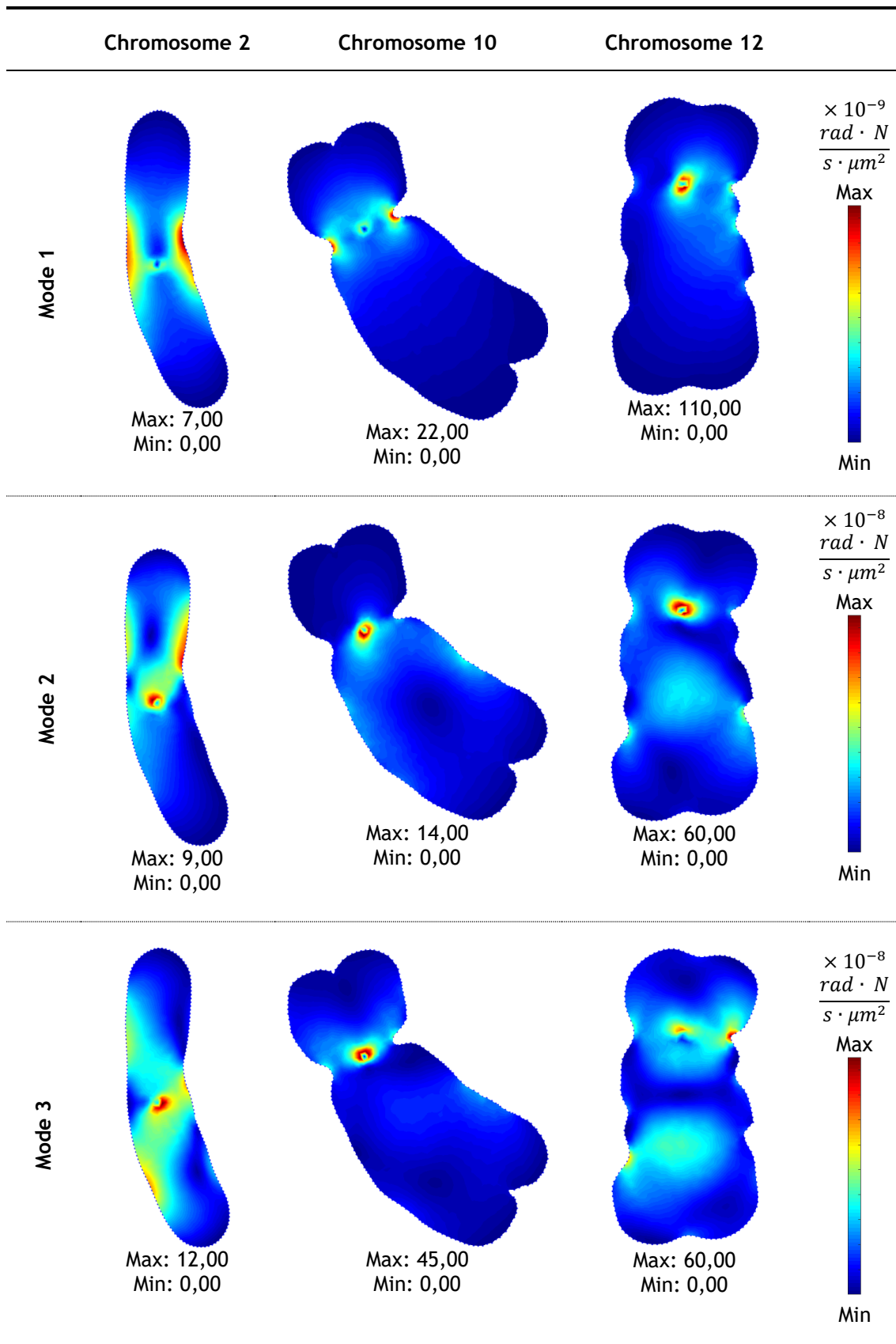


Table 7.8 - Parameterized equivalent effective strain field of natural vibrational modes 1-3 using RPIM for 3 different 2D human chromosome models.

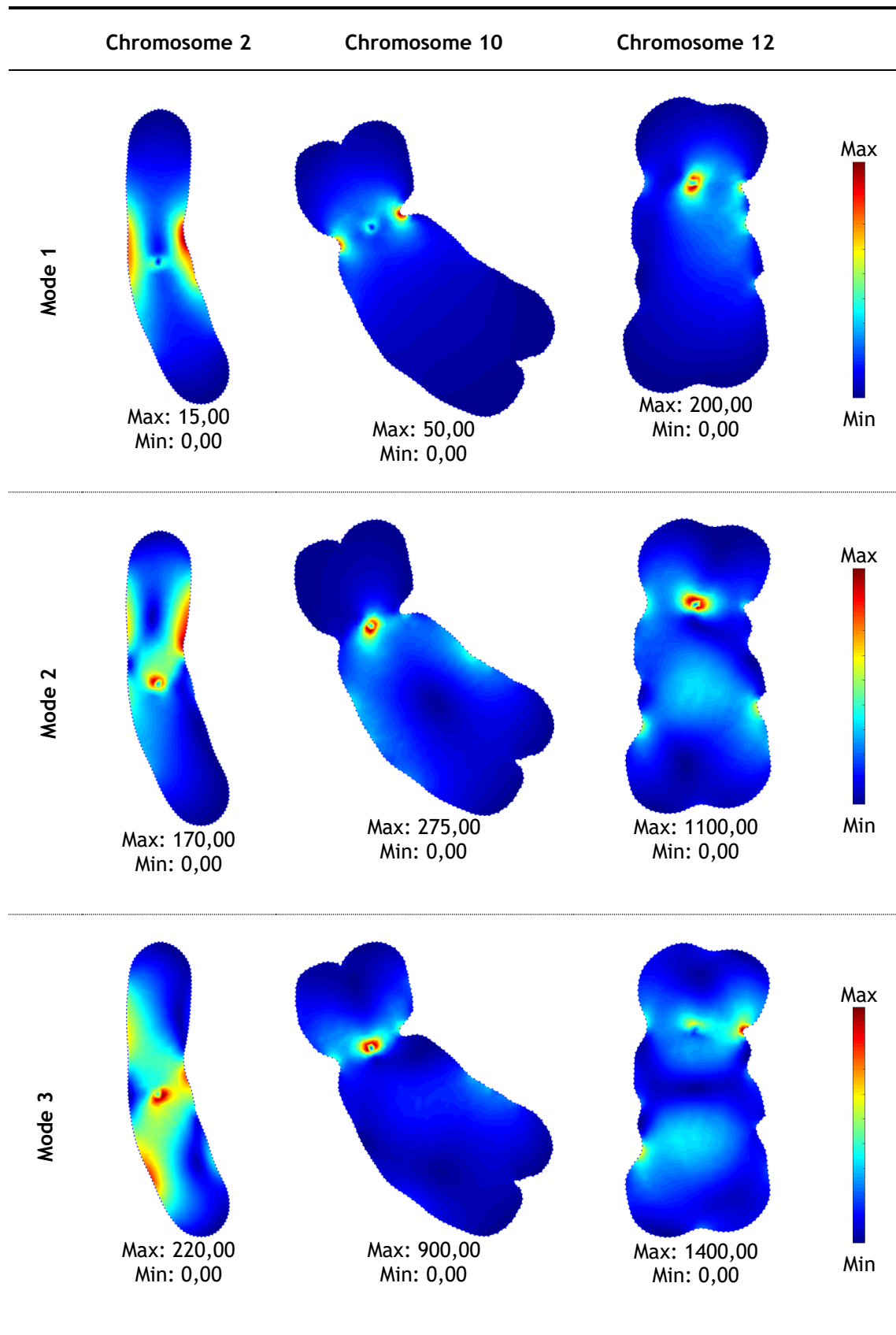


Table 7.9 - Parameterized displacement field of natural vibrational modes 1-3 using NNRPIM for 3 different 2D human chromosome models.

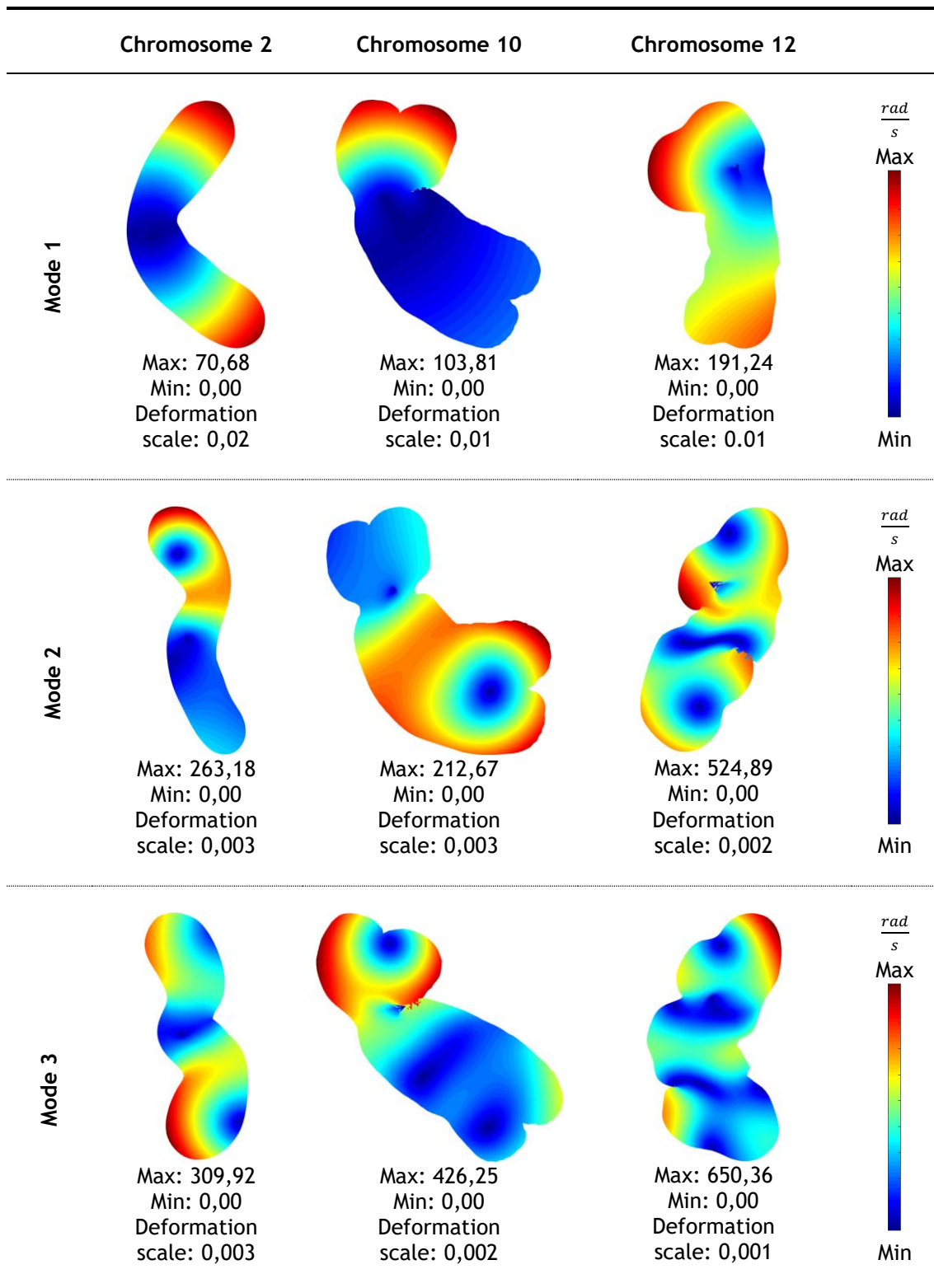


Table 7.10 - Parameterized von Mises effective stress field of natural vibrational modes 1-3 using NNRPIM for 3 different 2D human chromosome models.

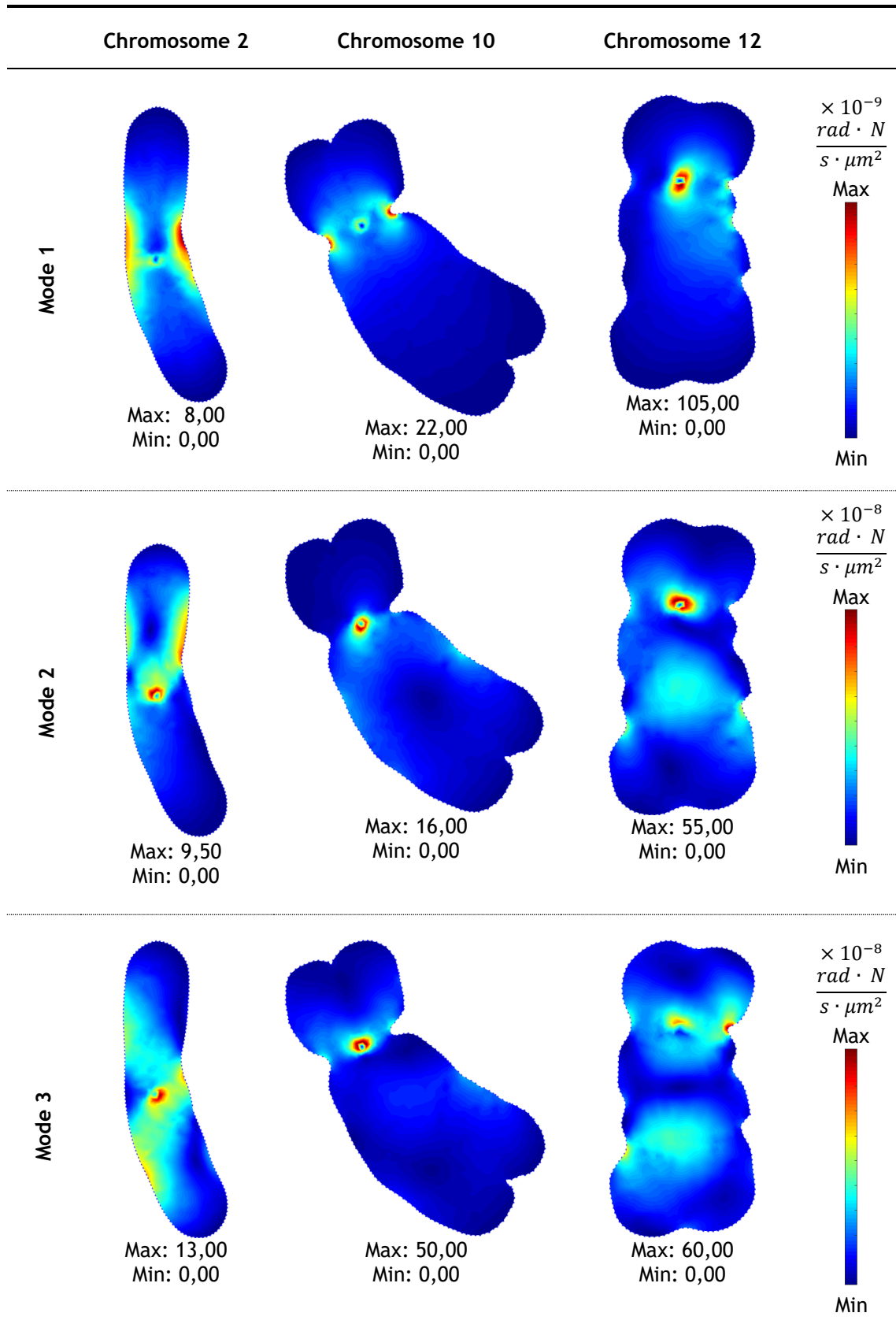


Table 7.11 - Parameterized equivalent effective strain field of natural vibrational modes 1-3 using NNRPIM for 3 different 2D human chromosome models.

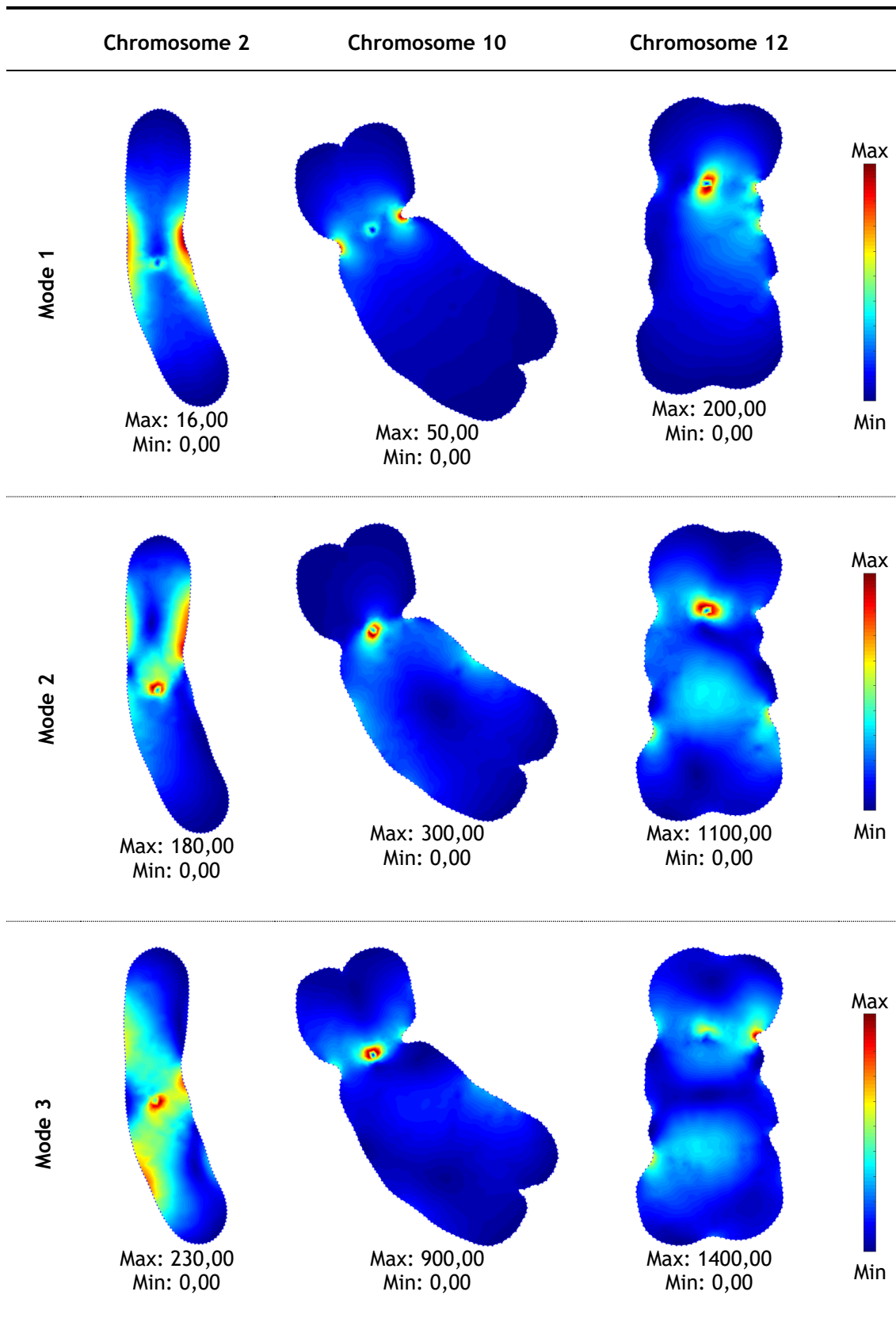


Table 7.12 - Parameterized displacement field of natural vibrational modes 1-3 using FEM for 3 different 3D human chromosome models.

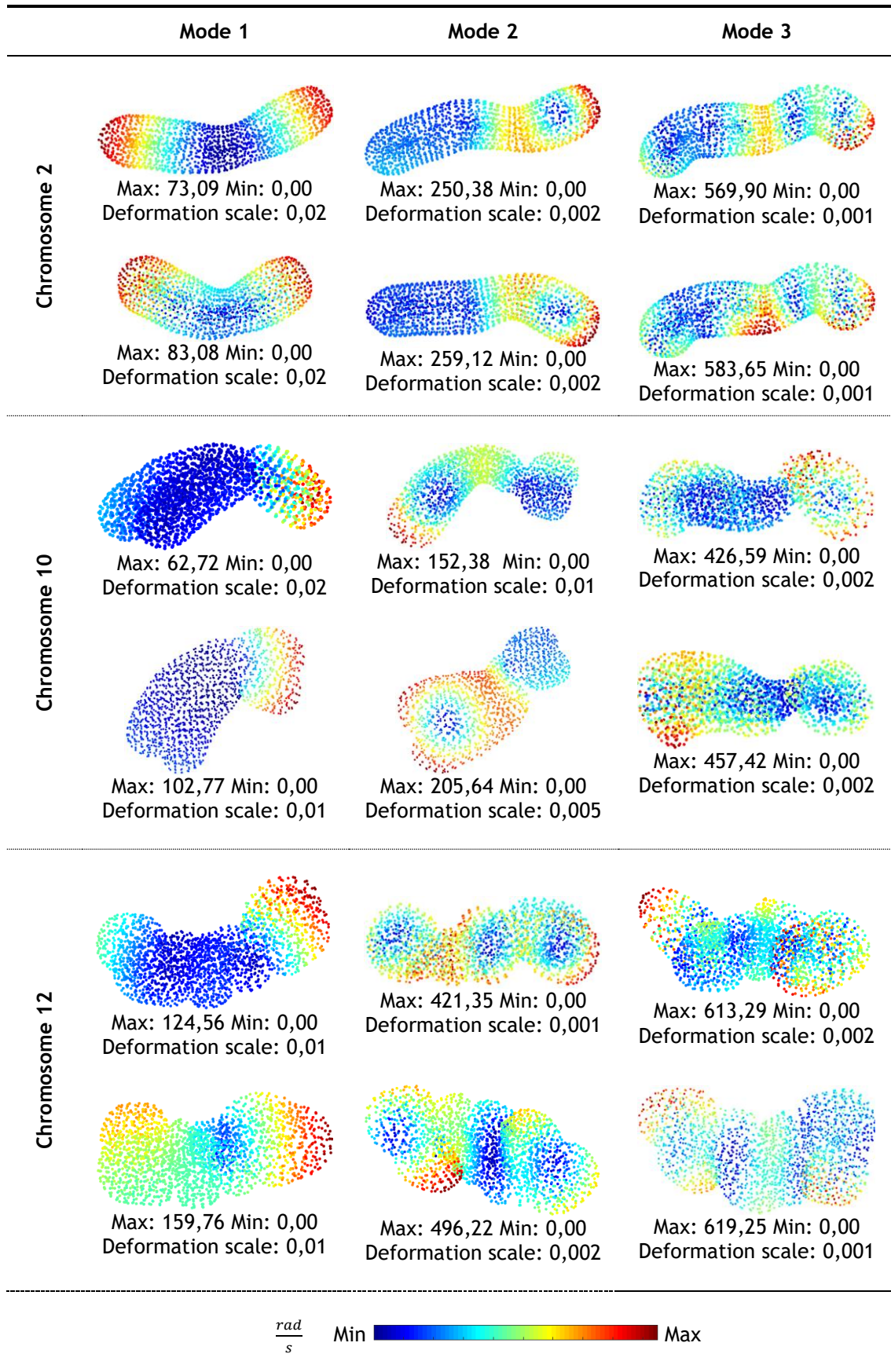


Table 7.13 - Parameterized von Mises effective stress field of natural vibrational modes 1-3 using FEM for 3 different 3D human chromosome models.

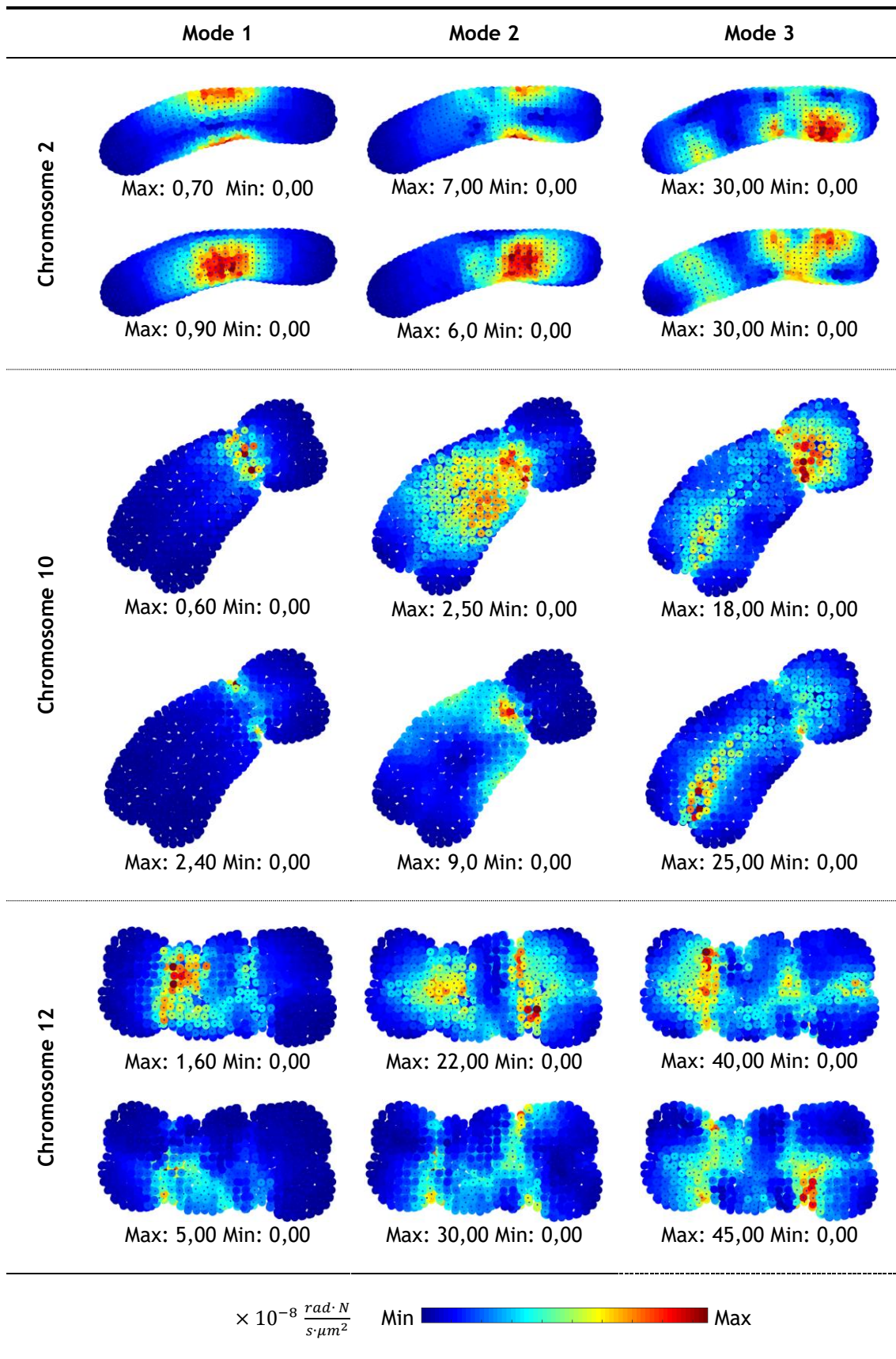


Table 7.14 - Parameterized equivalent effective strain field of natural vibrational modes 1-3 using FEM for 3 different 3D human chromosome models.

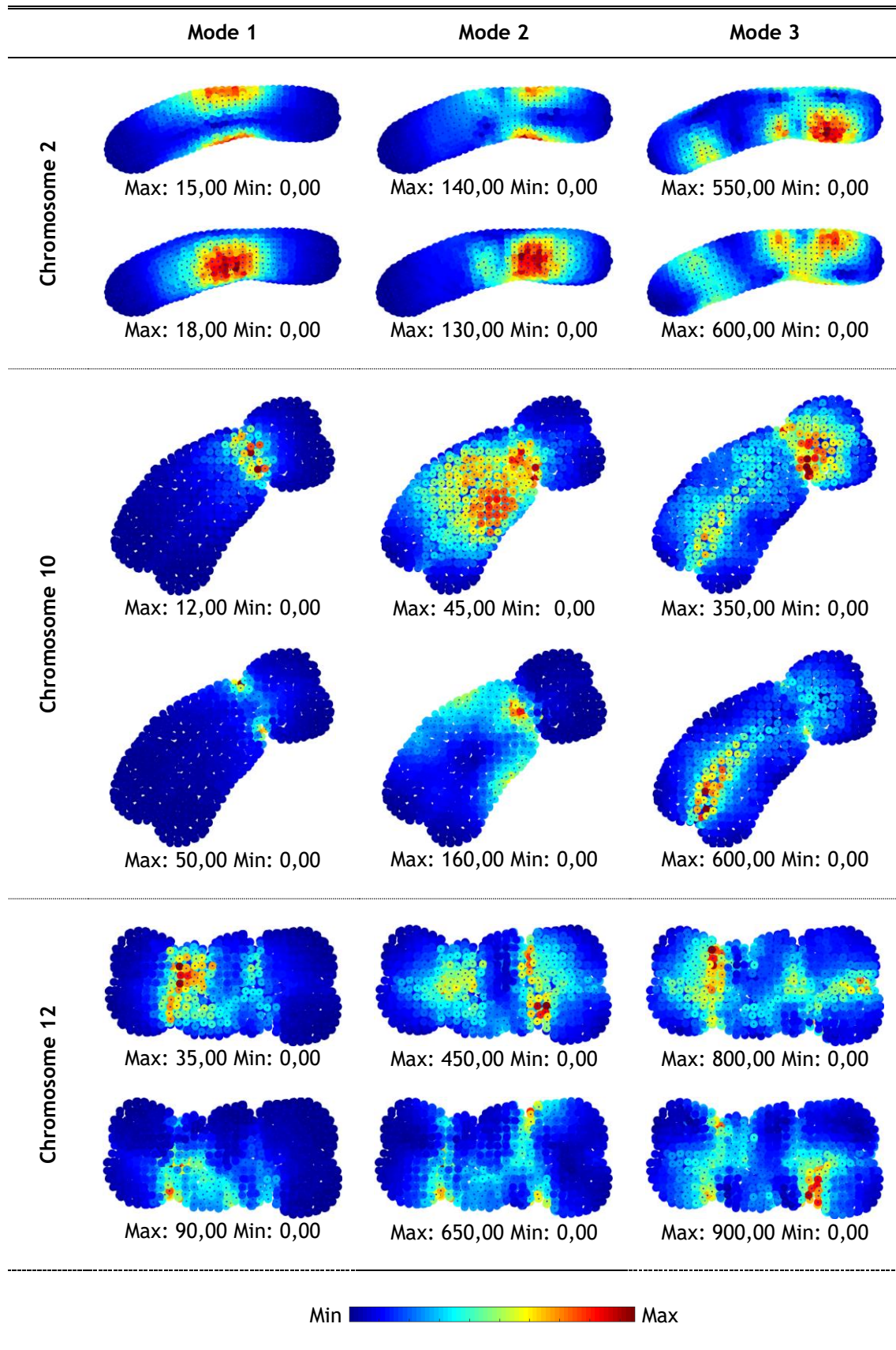


Table 7.15 - Parameterized displacement field of natural vibrational modes 1-3 using RPIM for 3 different 3D human chromosome models.

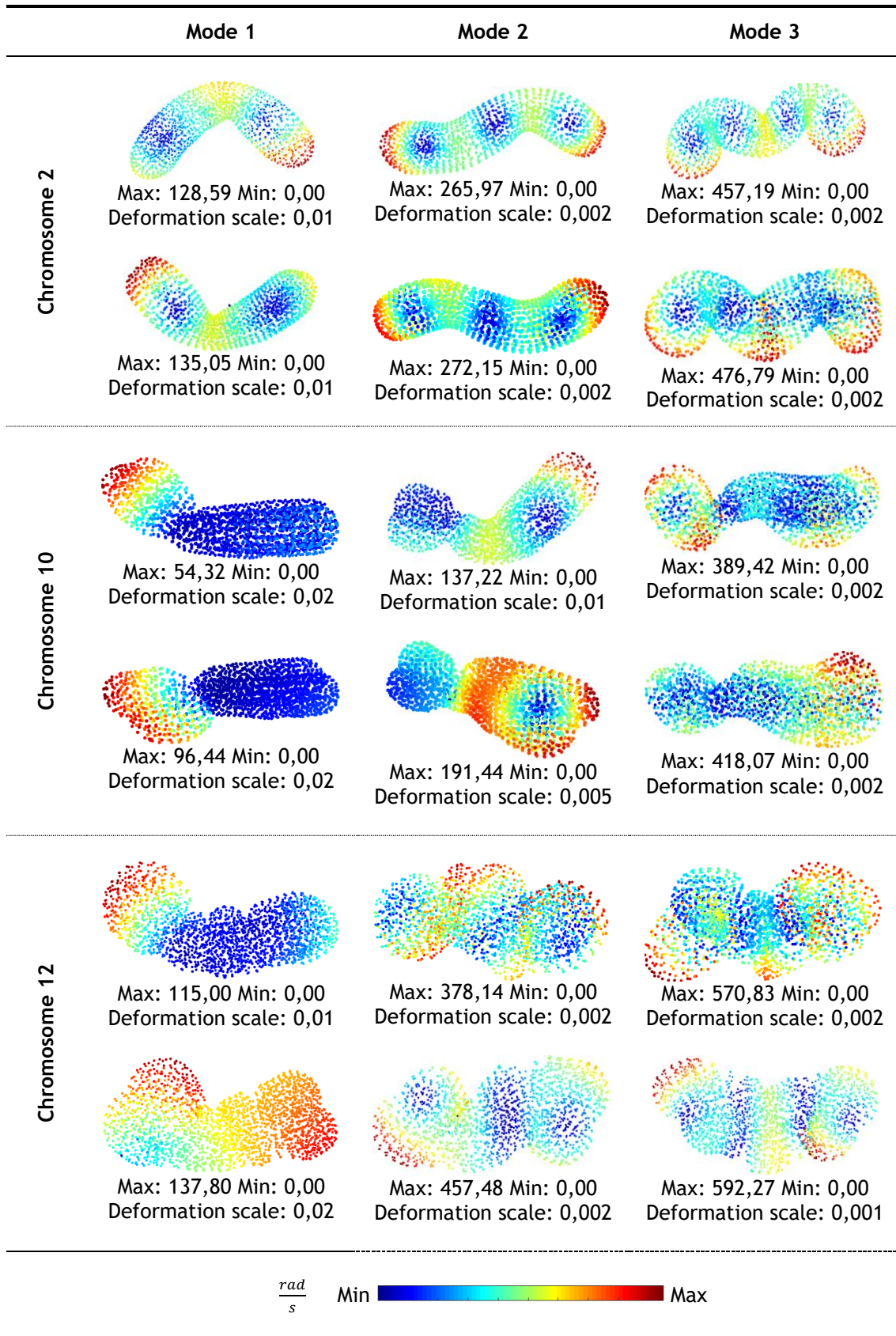


Table 7.16 - Parameterized von Mises effective stress field of natural vibrational modes 1-3 using RPIM for 3 different 3D human chromosome models.

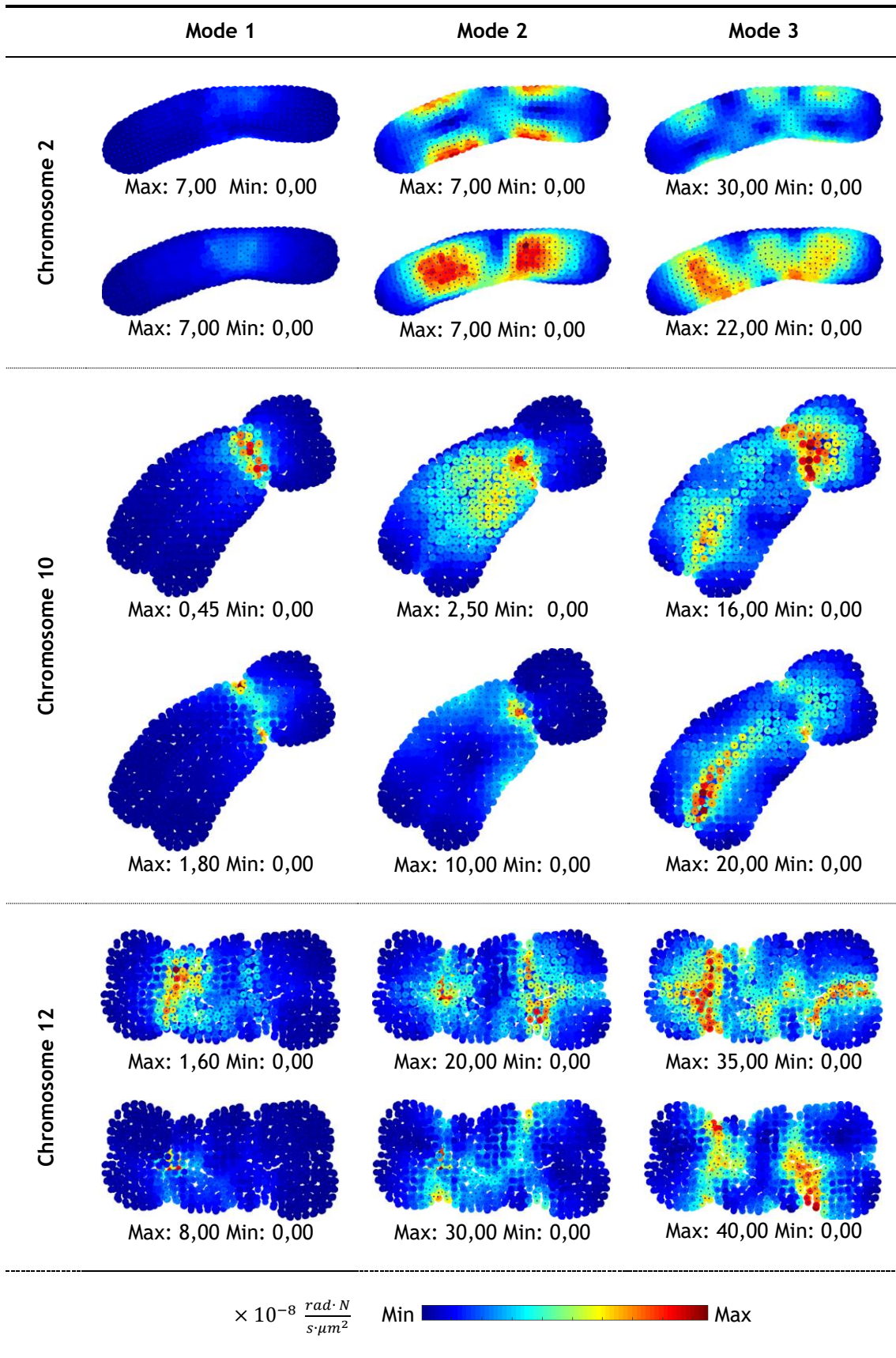


Table 7.17 - Parameterized equivalent effective strain field of natural vibrational modes 1-3 using RPIM for 3 different 3D human chromosome models.

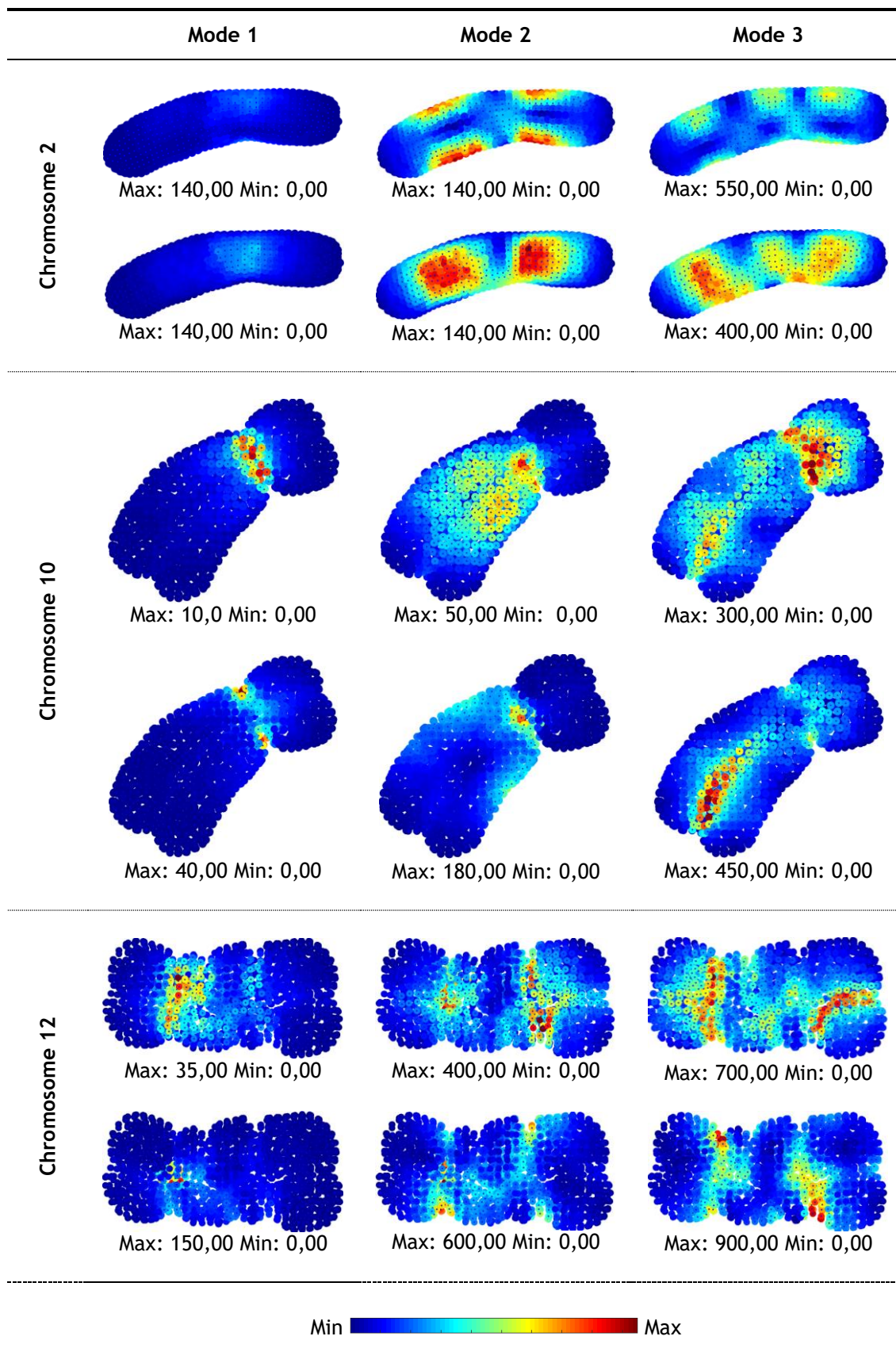


Table 7.18 - Parameterized displacement field of natural vibrational modes 1-3 using NNRPIM for 3 different 3D human chromosome models.

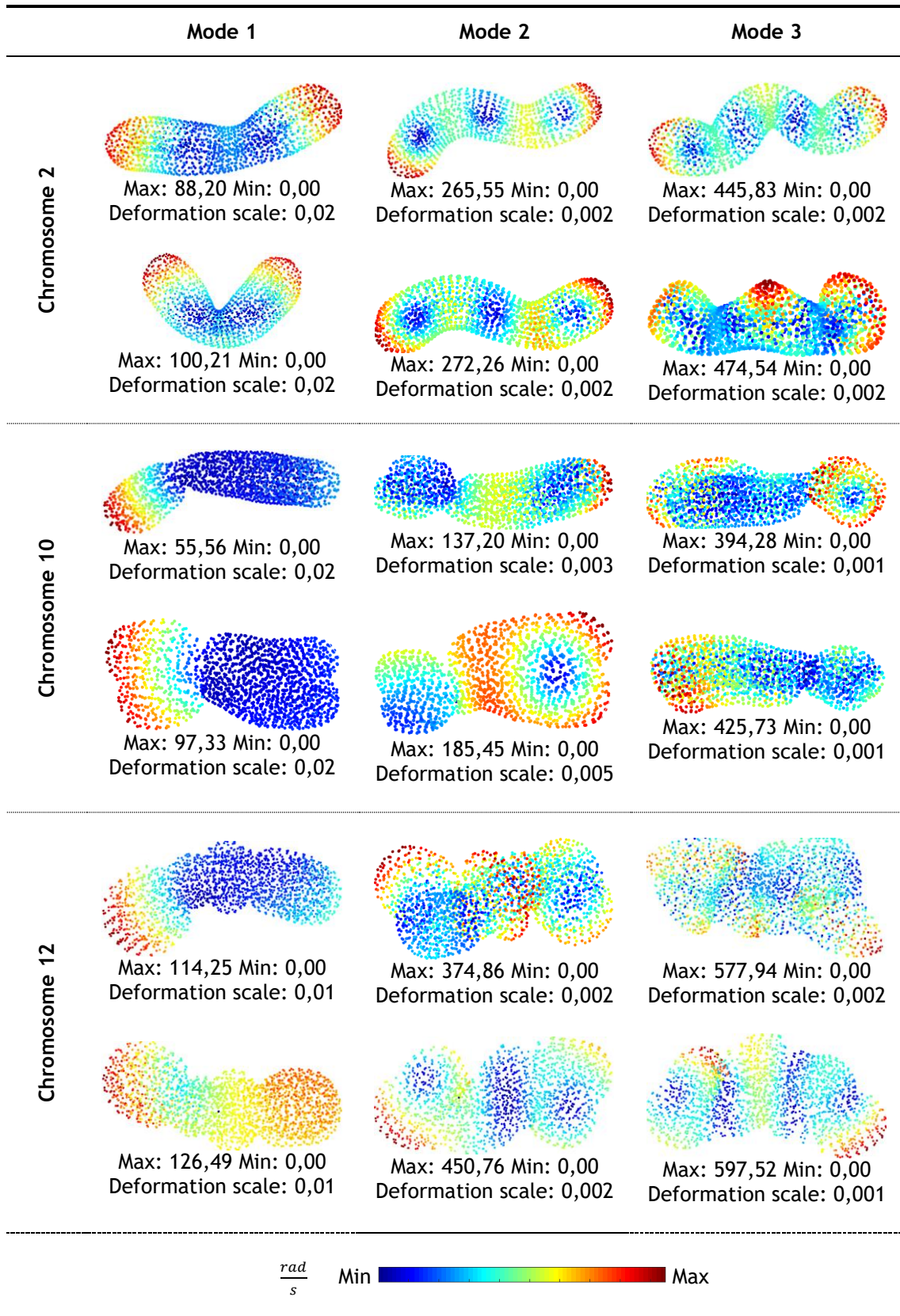


Table 7.19 - Parameterized von Mises effective stress field of natural vibrational modes 1-3 using NNRPIM for 3 different 3D human chromosome models.

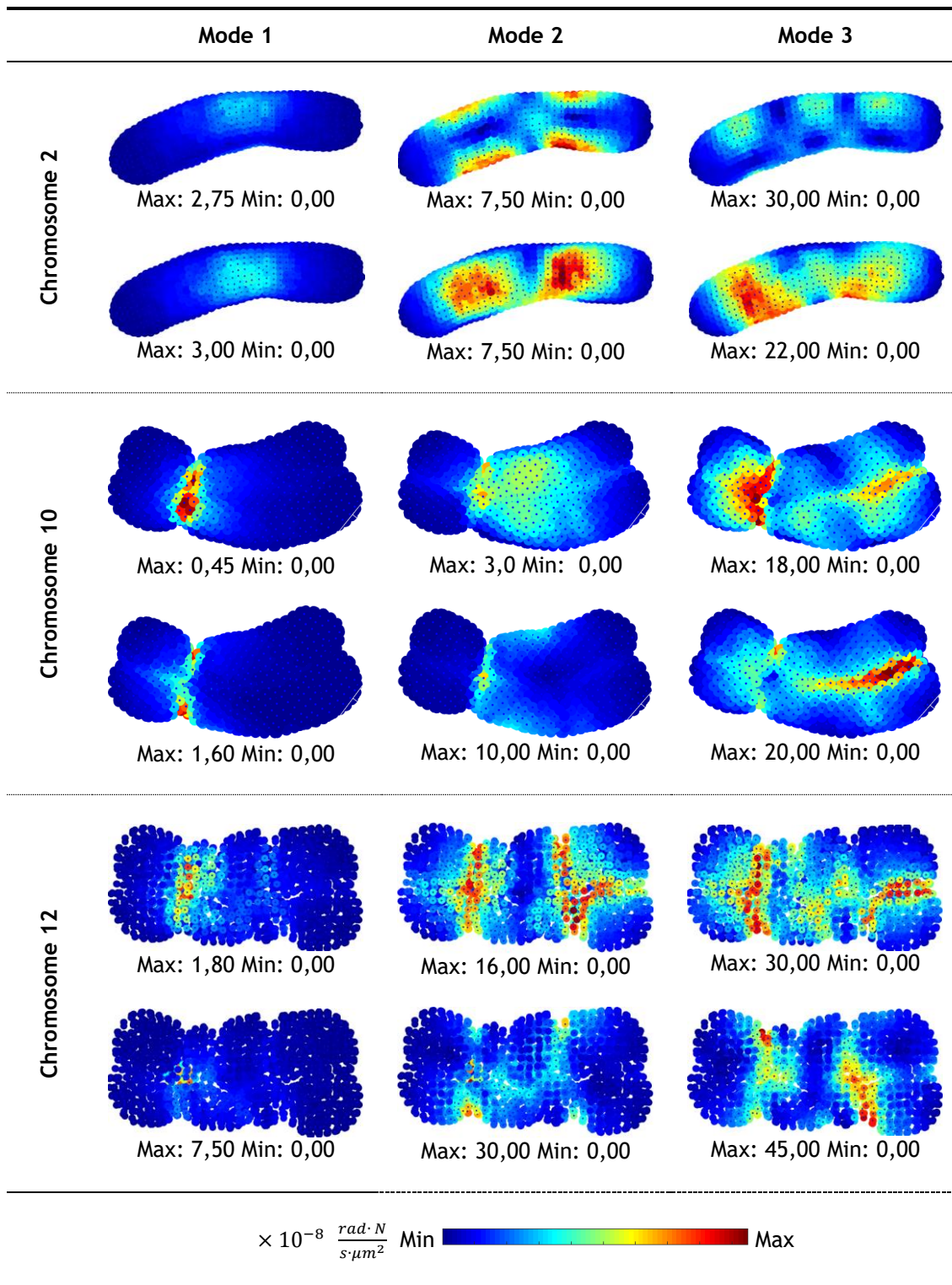
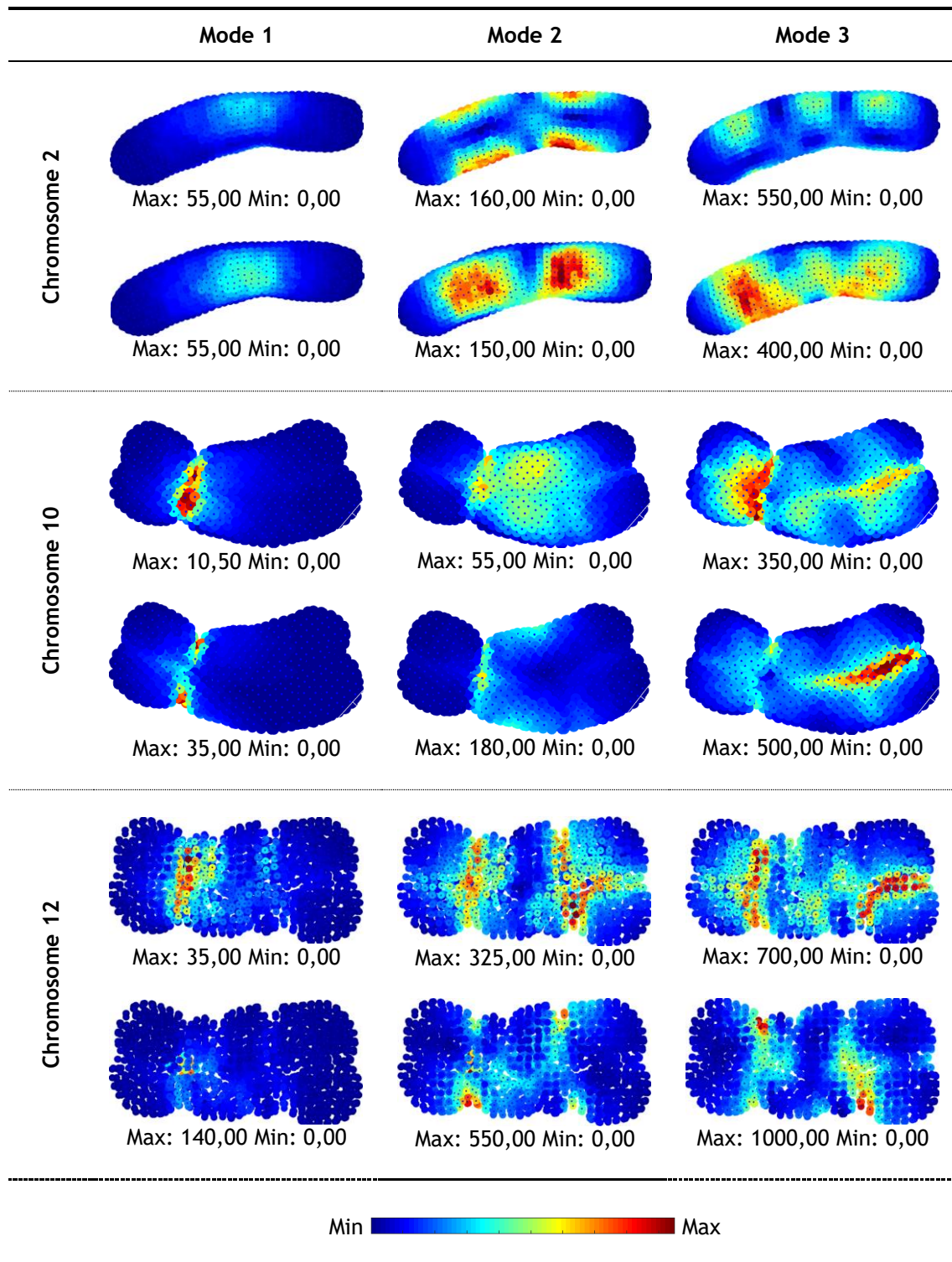


Table 7.20 - Parameterized equivalent effective strain field of natural vibrational modes 1-3 using NNRPIM for 3 different 3D human chromosome models.



Chapter 8

Conclusions and Future Work

One of the main challenges and desires that is part of the deepest instincts of the human species is the desire for increasingly larger lifetime. With the advances of modern society in terms of food, hygiene, medicines, etc., a lot has been achieved, however, it seems that with each new day and new conquer, new barriers are raised. Many of the health problems, such as cancer, are closely related to the basis of the code that regulates the organism, DNA. Very little is yet known about its structure and how its rediscovery can aid in the development of new therapies, such as the destruction of mutated chromosomes through their resonant frequencies.

The main objective of this thesis was to simulate the static and dynamic behavior of human chromosomes at the microscale level using meshless methods and with this, validate the mechanical model and conclude about the possibility of having natural frequencies and modes of vibration characteristic of each chromosome. Besides these two main objectives, it was also aimed to draw from this work further comparisons from FEM and the meshless methods used.

As it was reported in the previous chapter, this analysis was performed as intended, allowing to define ranges of frequencies and/or to select certain modes of vibration that only corresponds to a single chromosome, meaning that it is possible to identify different chromosomes based on its natural vibrations.

The use of meshless methods also proved to be adequate, as it could be seen by significant and recurring overlay of results between this methods and the more widely used FEM. As problems in biomechanics often present a high degree of complexity, either by their geometry or phenomena involved, the reliability of the RPIM and NNRPIM (concluded from the present work), added to the facility that meshless methods show in modelling complex geometries, should make them a primary tool for the study of mechanobiologic problems in biomechanics. It was also possible to conclude that meshless methods converge faster than FEM and considering the same number of nodes, even though meshless methods require a higher computational time, the same solution can be achieved using fewer nodes than FEM, which means that the same accuracy in results can be obtained through a smaller mesh.

While this work reached all of the proposed objectives, it also had some limitations:

- The commercial software used to determine the location of the nodes, even on a simple geometry and with two symmetry axes, causes an irregular arrangement of the nodes, affecting the results immediately;
- The hardware available limited the level of discretion that could be achieved, the numerical analysis had to be limited to around 2000 nodes;
- It was not possible to conclude on the best description of the problem in 2D using several layers due to the simplifications made in the model and for that reason cannot be transcribed for the models of human chromosomes;
- The reduced knowledge about the internal structure of the chromosomes, namely the centromere, and how the chromatin constituting the two arms relates, led us to consider a homogeneous material and to consider the frontier between the sister chromatids as a continuous material with equal properties;
- The type and quality of the microscopy images used as reference for the construction of the models directly influence the final geometry. As well as the researcher's expertise in the manipulation of drawing tools and software since there is no adequate segmentation software;
- In no case was considered the surrounding environment, the cytosol, that could have a great impact on the natural vibrations, as well as on the remaining tests.

In the future, it would be interesting to continue this work, by testing different approaches to the same problem, for instance:

- A multi-scale analysis;
- Consider non-linearity of materials and geometry;
- To evaluate the influence of the surrounding environment on the modes and frequency of natural vibrations;
- Study of a larger number of chromosomes;
- Study chromosomes with gene mutations that determine structural/geometric defects;
- Simulation of the division of chromosomes by daughter cells in the process of cell division.

Bibliography

- [1] Ferlay J, Soerjomataram I, and Ervik M, "GLOBOCAN 2012 v1.0, Cancer Incidence and Mortality Worldwide: IARC Cancer Base No. 11," 2013. [Online]. Available: <http://globocan.iarc.fr>. [Accessed: 10-Dec-2016].
- [2] B. W. Stewart and C. P. Wild, "World cancer report 2014," *World Heal. Organ.*, pp. 1-2, 2014.
- [3] S. Cuthill, "Cellular Epigenetics and the Origin of Cancer," *BioEssays*, vol. 16, no. 6, pp. 393-394, 1994.
- [4] A. R. Kennedy, M. Fox, G. Murphy, J. B. Little, A. N. N. R. Kennedy, and G. Murphy, "Relationship between x-ray exposure and malignant transformation in C3H 10T1/2 Cells," in *Proceedings of the National Academy of Sciences of the United States of America*, 1980, vol. 77, pp. 7262-7266.
- [5] R. E. Shore, "Electromagnetic radiations and cancer. Cause and prevention," *Cancer*, vol. 62, no. 8 Suppl, pp. 1747-1754, 1988.
- [6] D. Medina, "Premalignant and malignant mammary lesions induced by MMTV and chemical carcinogens," *J. Mammary Gland Biol. Neoplasia*, vol. 13, no. 3, pp. 271-277, 2008.
- [7] S. Cooper and S. G. Spiro, "Small cell lung cancer: treatment review.," *Respirology*, vol. 11, no. 3, pp. 241-8, 2006.
- [8] A. Tárnok, "Cytometry of DNA mutation and modification," *Cytom. Part A*, vol. 75, no. 7, pp. 555-556, 2009.
- [9] T. Boehm, "An old paradigm for treating cancer and other diseases in the 21st century," *Cancer and Metastasis Revivis*, vol. 12, pp. 149-154, 1998.
- [10] H. Singh, E. A. Sekinger, and D. S. Gross, "Chromatin and cancer: causes and consequences," *J Cell Biochem Suppl*, vol. Suppl 35, pp. 61-68, 2000.
- [11] D. Ghosh, C. Saha, M. Hossain, S. K. Dey, and G. S. Kumar, "Biophysical studies of mutated K562 DNA (erythroleukemic cells) binding to adriamycin and daunomycin reveal that mutations induce structural changes influencing binding behavior," *J. Biomol. Struct. Dyn.*, vol. 31, no. 3, pp. 331-341, 2012.
- [12] G. D. Balkwill, H. E. L. Williams, and M. S. Searle, "Structure and folding dynamics of a DNA hairpin with a stabilising d(GNA) trinucleotide loop: influence of base pair mismatches and point mutations on conformational equilibria.," *Org. Biomol. Chem.*, vol. 5, no. 5, pp. 832-9, 2007.
- [13] R. P. Ghosh, R. A. Horowitz-Scherer, T. Nikitina, L. M. Gierasch, and C. L. Woodcock, "Rett syndrome-causing mutations in human MeCP2 result in diverse structural changes that impact folding and DNA interactions," *J. Biol. Chem.*, vol. 283, no. 29, pp. 20523-20534, 2008.
- [14] M. P. Norton and D. G. Karczub, *Fundamentals of Noise and Vibration Analysis for Engineers*. Cambridge University Press, 2013.
- [15] S. L. Lai, D. R. Wu, and Y. R. Lao, "Scientific principles and rigorous processes should be followed in developing clinical guidelines for therapeutic interventions of integrative medicine," *Chin. J. Integr. Med.*, vol. 14, no. 1, pp. 3-5, 2008.
- [16] J. M. Hoebert, L. van Dijk, and A. K. Mantel-Teeuwisse, "National medicines policies - a review of the evolution and development processes," *J. Pharm. Policy Pract.*, vol. 6, no. 1, p. 5, 2013.

- [17] R. Hooke, *Micrographia: Some Physiological Descriptions of Minute Bodies Made by Magnifying Glasses with Observations and Inquiries Thereupon*. Courier Dover Publications, 1665.
- [18] C. S. Ball, "The Early History of the Compound Microscope," *Bios*, vol. 37, no. 2, pp. 51-60, 1966.
- [19] P. Mazzeo, "A unifying concept: the history of cell theory.," *Nat. Cell Biol.*, vol. 1, no. 1, pp. E13--5, 1999.
- [20] J. Watson and F. Crick, "Molecular Structure of Nucleic Acids," *Nature*, vol. 224, pp. 488-490, 1969.
- [21] F. Crick, "Central dogma of molecular biology.," *Nature*, vol. 227, no. 5258, pp. 561-3, 1970.
- [22] H. Lodish, A. Berk, L. Zipursky, P. Matsudaira, D. Baltimore, and J. E. Darnell, *Molecular Cell Biology*. W. H. Freeman and Company, 2000.
- [23] F. Barré-sinoussi, "Cell and Molecular Biology Concepts and Experiments," *Mol. Biol.*, 2010.
- [24] B. Ramezani, I. Haan, A. Osterhaus, and E. Claassen, "Vector-based genetically modified vaccines: Exploiting Jenner's legacy," *Vaccine*, vol. 34, no. 50, pp. 6436-6448, 2016.
- [25] N. Preeda, T. Yanagi, K. Sone, S. Taketa, and N. Okuda, "Chromosome observation method at metaphase and pro-metaphase stages in diploid and octoploid strawberries," *Sci. Hortic. (Amsterdam)*, vol. 114, no. 2, pp. 133-137, 2007.
- [26] Human Chromosomes Study Group (University of Colorado Medical Center), "A proposed standard system of nomenclature of human mitotic chromosomes (Denver, Colorado)," *Ann. Hum. Genet.*, vol. 24, no. 4, pp. 319-326, 1960.
- [27] A. S. Belmont, "Mitotic chromosome structure and condensation," *Curr. Opin. Cell Biol.*, vol. 18, no. 6, pp. 632-638, 2006.
- [28] R. McElligott and R. J. Wellinger, "The terminal DNA structure of mammalian chromosomes," *EMBO J.*, vol. 16, no. 12, pp. 3705-3714, 1997.
- [29] K. W. Adolph, "Isolation and structural organization of human mitotic chromosomes.," *Chromosoma*, vol. 76, pp. 23-33, 1980.
- [30] N. Kleckner, D. Zickler, G. H. Jones, J. Dekker, R. Padmore, J. Henle, and J. Hutchinson, "A mechanical basis for chromosome function.," *Proc. Natl. Acad. Sci. U. S. A.*, vol. 101, no. 34, pp. 12592-12597, 2004.
- [31] J. F. Marko, "Micromechanical studies of mitotic chromosomes," *Chromosom. Res.*, vol. 16, no. 3, pp. 469-497, 2008.
- [32] B. Houchmandzadeh and S. Dimitrov, "Elasticity measurements show the existence of thin rigid cores inside mitotic chromosomes," *J. Cell Biol.*, vol. 145, no. 2, pp. 215-223, 2000.
- [33] E. Chargaff, "Chemical specificity of nucleic acids and mechanism of their enzymatic degradation," *Experientia*, vol. 6, no. 6, pp. 201-209, 1950.
- [34] P. A. Levene and F. B. La Forge, "On Chondrosamine," vol. 1, no. 4, pp. 190-191, 1915.
- [35] F. Crick, "The double helix: a personal view," *Nature*, vol. 248, pp. 766-769, 1974.
- [36] A. Klug, "The discovery of the DNA double helix," *J. Mol. Biol.*, vol. 335, no. 1, pp. 3-26, 2004.
- [37] M. H. Wilkins, "Molecular configuration of nucleic acids.," *Science*, vol. 140, pp. 941-950, 1963.
- [38] J. D. Rowley, "Theodore T. Puck (September 24, 1916 - November 6, 2005)," no. 46, pp. 365-366, 2006.
- [39] H. CHROMOSOMES, "A Proposed Standard of Nomenclature of Human Mitotic Chromosomes," *Dev. Med. Child Neurol.*, vol. 2, no. 3, pp. 1-5, 1960.
- [40] A. LEVAN, K. FREDGA, and A. A. SANDBERG, "Nomenclature for Centromeric Position on Chromosomes," *Hereditas*, vol. 52, no. 2, pp. 201-220, 1964.
- [41] C. A. Naranjo, L. Poggio, and P. E. Brandham, "A practical method of chromosome classification on the basis of centromere position," *Genetica*, vol. 62, no. 1, pp. 51-53, 1983.
- [42] M. Sun, R. Kawamura, and J. F. Marko, "Micromechanics of human mitotic chromosomes," *Phys. Biol.*, vol. 8, 2011.
- [43] J. M. R. Delgado, "Physical Techniques in Biological Research: Electrophysiological

- Methods, Part A," *Phys. Tech. Biol. Res.*, vol. V, pp. 89-139, 1964.
- [44] B. Houchmandzadeh, J. F. Marko, D. Chatenay, and A. Libchaber, "Elasticity and structure of eukaryote chromosomes studied by micromanipulation and micropipette aspiration," *J. Cell Biol.*, vol. 139, no. 1, pp. 1-12, 1997.
- [45] M. G. Poirier, S. Eroglu, and J. F. Marko, "The bending rigidity of mitotic chromosomes," *Mol. Biol. Cell*, vol. 13, no. 6, pp. 2170-2179, 2002.
- [46] Y. Zhang and D. W. Heermann, "Loops determine the mechanical properties of mitotic chromosomes," *PLoS One*, vol. 6, no. 12, 2011.
- [47] M. G. Poirier and J. F. Marko, "Micromechanical studies of mitotic chromosomes," *Chromosom. Res.*, vol. 23, pp. 409-431, 2002.
- [48] R. B. Nicklas, "Measurements of the force produced by the mitotic spindle in anaphase," *J. Cell Biol.*, vol. 97, no. 2, pp. 542-548, 1983.
- [49] M. Poirier, S. Eroglu, D. Chatenay, and J. F. Marko, "Reversible and irreversible unfolding of mitotic newt chromosomes by applied force," *Mol. Biol. Cell*, vol. 11, no. 1, pp. 269-276, 2000.
- [50] F. Erdel, M. Baum, and K. Rippe, "The viscoelastic properties of chromatin and the nucleoplasm revealed by scale-dependent protein mobility," *J. Phys. Condens. Matter*, vol. 27, no. 6, p. 64115, 2015.
- [51] T. G. Mason and D. A. Weitz, "Optical measurements of frequency-dependent linear viscoelastic moduli of complex fluids," *Phys. Rev. Lett.*, vol. 74, no. 7, pp. 1250-1253, 1995.
- [52] G. Guigas, C. Kalla, and M. Weiss, "Probing the nanoscale viscoelasticity of intracellular fluids in living cells," *Biophys. J.*, vol. 93, no. 1, pp. 316-23, 2007.
- [53] A. B. Fulton, "How crowded is the cytoplasm?," *Cell*, vol. 30, no. 2, pp. 345-347, 1982.
- [54] P. S. Heckbert, "Introduction to Finite Element Methods," *Most*, pp. 1-10, 1993.
- [55] E. Süli, *Lecture Notes on Finite Element Methods for Partial Differential Equations*, no. December. University of Oxford, 2012.
- [56] T. Y. Chao, W. K. Chow, and H. Kong, "A review on the applications of finite element method to heat transfer and fluid flow," *Int. J. Archit. Sci.*, vol. 3, no. 1, pp. 1-19, 2002.
- [57] C. Zhao and G. P. Steven, "Asymptotic solutions for predicted natural frequencies of two-dimensional elastic solid vibration problems in finite element analysis," *Int. J. Numer. Methods Eng.*, vol. 39, no. 16, pp. 2821-2835, 1996.
- [58] O. C. Zienkiewicz, R. L. Taylor, and J. Z. Zhu, *The Finite Element Method*, 6th ed. Elsevier Butterworth-Heinemann, 2005.
- [59] K.-J. Bathe, *Finite element procedures. Second edition*. 2006.
- [60] G. Strang and G. Fix, "An analysis of the finite element method." 1997.
- [61] E. B. Becker, G. F. Carey, and J. T. Oden, "Finite Elements, An Introduction: Volume I." Prentice-Hall, Inc., Englewood Cliffs, 1981.
- [62] J. C. Zhao, Q. Li, and X. Y. Shen, "Finite element analysis and structure optimization for improving the fatigue life of rubber mounts," *J. Macromol. Sci. Part A*, vol. 45, no. 7, pp. 542-547, 2008.
- [63] M. Shojima, M. Oshima, K. Takagi, R. Torii, M. Hayakawa, K. Katada, A. Morita, and T. Kirino, "Magnitude and Role of Wall Shear Stress on Cerebral Aneurysm: Computational Fluid Dynamic Study of 20 Middle Cerebral Artery Aneurysms," *Stroke*, vol. 35, no. 11, pp. 2500-2505, 2004.
- [64] G. Meriç, E. Erkmen, A. Kurt, Y. Tunç, and A. Eser, "Influence of prosthesis type and material on the stress distribution in bone around implants: A 3-dimensional finite element analysis," *J. Dent. Sci.*, vol. 6, no. 1, pp. 25-32, 2011.
- [65] G. Meriç, E. Erkmen, A. Kurt, A. Eser, and G. Çelik, "Biomechanical evaluation of a fiber-reinforced composite prosthesis supported by implants with and without a microthread collar design," *J. Dent. Sci.*, vol. 5, no. 4, pp. 201-208, 2010.
- [66] T. Wu, W. Liao, N. Dai, and C. Tang, "Design of a custom angled abutment for dental implants using computer-aided design and nonlinear finite element analysis," *J. Biomech.*, vol. 43, no. 10, pp. 1941-1946, 2010.
- [67] J. Lepage, C. Jayyosi, P. Lecomte-Grosbras, M. Brieu, C. Duriez, M. Cosson, and C. Rubod, "Biomechanical pregnant pelvic system model and numerical simulation of childbirth: impact of delivery on the uterosacral ligaments, preliminary results," *Int.*

- Urogynecol. J. Pelvic Floor Dysfunct.*, vol. 26, no. 4, pp. 497-504, 2015.
- [68] K. M. Liew, X. Zhao, and A. J. M. Ferreira, "A review of meshless methods for laminated and functionally graded plates and shells," *Compos. Struct.*, vol. 93, no. 8, pp. 2031-2041, 2011.
- [69] V. P. Nguyen, T. Rabczuk, S. Bordas, and M. Duflot, "Meshless methods: A review and computer implementation aspects," *Math. Comput. Simul.*, vol. 79, no. 3, pp. 763-813, 2008.
- [70] G. R. Liu and Y. T. Gu, "A point interpolation method for two-dimensional solids," *Int. J. Numer. Methods Eng.*, vol. 50, no. 4, pp. 937-951, 2001.
- [71] T. Belytschko, Y. Krongauz, D. Organ, M. Fleming, and P. Krysl, "Meshless methods: An overview and recent developments," *Comput. Methods Appl. Mech. Eng.*, vol. 139, no. 1, pp. 3-47, 1996.
- [72] Y. T. Gu, "Meshfree Methods and Their Comparisons," *Int. J. Comput. Methods*, vol. 2, no. 4, pp. 477-515, 2005.
- [73] J. Belinha, R. M. Natal Jorge, and L. M. J. S. Dinis, "Bone tissue remodelling analysis considering a radial point interpolator meshless method," *Eng. Anal. Bound. Elem.*, vol. 36, no. 11, pp. 1660-1670, 2012.
- [74] J. Belinha, *Meshless Methods in Biomechanics: Bone Tissue Remodelling Analysis*, vol. 2. 2014.
- [75] H. Liu, D. Zou, and J. Liu, "Particle Shape Effect on Macro-and Micro Behaviours of Monodisperse Ellipsoids," *Int. J. Numer. Anal. Methods Geomech.*, vol. 32, no. March 2007, pp. 189-213, 2008.
- [76] B. Nayroles, G. Touzot, and P. Villon, "Generalizing the finite element method: Diffuse approximation and diffuse elements," *Comput. Mech.*, vol. 10, no. 5, pp. 307-318, 1992.
- [77] T. Belytschko, L. Gu, and Y. Y. Lu, "Fracture and crack growth by element free Galerkin methods," *Model. Simul. Mater. Sci. Eng.*, vol. 2, no. 3A, pp. 519-534, 1999.
- [78] J. G. Wang and G. R. Liu, "A point interpolation meshless method based on radial basis functions," *Int. J. Numer. Methods Eng.*, vol. 54, no. 11, pp. 1623-1648, 2002.
- [79] J. G. Wang and G. R. Liu, "On the optimal shape parameters of radial basis functions used for 2-D meshless methods," *Comput. Methods Appl. Mech. Eng.*, vol. 191, no. 23-24, pp. 2611-2630, 2002.
- [80] N. Sukumar, B. Moran, A. Y. Semenov, and V. V. Belikov, "Natural neighbour Galerkin methods," *Int. J. Numer. Methods Eng.*, vol. 50, no. 1, pp. 1-27, 2000.
- [81] J. Braun and M. Sambridge, "A numerical method for solving partial differential equations on highly irregular evolving grids," *Nature*, vol. 376, no. 6542, pp. 655-660, 1995.
- [82] N. Sukumar and T. Belytschko, "The natural element method in solid mechanics," *Int. J. Numer. Methods Eng.*, vol. 43, no. 5, pp. 839-887, 1998.
- [83] L. M. J. S. Dinis, R. M. Natal Jorge, and J. Belinha, "Analysis of 3D solids using the natural neighbour radial point interpolation method," *Comput. Methods Appl. Mech. Eng.*, vol. 196, no. 13-16, pp. 2009-2028, 2007.
- [84] P. Filipe and D. O. Lopes, "Atherosclerosis Biomechanical Simulation," 2016.
- [85] W. Liu, S. Jun, and Y. Zhang, "Reproducing kernel particle methods," *Int. J. Numer. methods fluids*, vol. 20, no. 8-9, pp. 1081-1106, 1995.
- [86] S. N. Atluri and T. Zhu, "A new Meshless Local Petrov-Galerkin (MLPG) approach in computational mechanics," *Comput. Mech.*, vol. 22, no. 2, pp. 117-127, 1998.
- [87] J. Belinha, L. M. J. S. Dinis, and R. M. Natal Jorge, "The analysis of the bone remodelling around femoral stems: A meshless approach," *Math. Comput. Simul.*, vol. 121, pp. 64-94, 2016.
- [88] R. Sibson, "A vector identity for the Dirichlet tessellation," *Math. Proc. Cambridge Philos. Soc.*, vol. 87, no. 1, p. 151, 1980.
- [89] R. L. Hardy, "Theory and applications of the multiquadric-biharmonic method," *Comput. Math. Applic.*, vol. 19, no. 8/9, pp. 163-208, 1990.
- [90] L. M. J. S. Dinis, R. M. Natal Jorge, and J. Belinha, "Analysis of plates and laminates using the natural neighbour radial point interpolation method," *Eng. Anal. Bound. Elem.*, vol. 32, no. 3, pp. 267-279, 2008.
- [91] M. a. Golberg, C. S. Chen, and H. Bowman, "Some recent results and proposals for the use of radial basis functions in the BEM," *Eng. Anal. Bound. Elem.*, vol. 23, no. 4, pp.

- 285-296, 1999.
- [92] L. I. Sedov and P. G. Hodge, "Introduction to the Mechanics of a Continuous Medium," *J. Appl. Mech.*, vol. 33, no. 1, p. 238, 1966.
- [93] Z. Sawacha and B. Schrefler, "Finite Element Modelling in Musculoskeletal Biomechanics," *Model. Methodol. Physiol. Med. Second Ed.*, pp. 527-544, 2013.
- [94] J. A. Cottrell, T. J. R. Hughes, and Bazilevs, "Isogeometric analysis: toward integration of CAD and FEA," *Bautechnik*, vol. 88, p. 423, 2011.
- [95] T. J. R. Hughes, A. Reali, and G. Sangalli, "Efficient quadrature for NURBS-based isogeometric analysis," *Comput. Methods Appl. Mech. Eng.*, vol. 199, no. 5-8, pp. 301-313, 2010.
- [96] R. Lewis and B. Schrefler, *Finite Element Method in the Deformation and Consolidation of Porous Media*. 1998.
- [97] M. Schenke and W. Ehlers, "On the Analysis of Soils using an Abaqus-PANDAS Interface," *Pamm*, vol. 11, no. 1, pp. 431-432, 2011.
- [98] O. C. Zienkiewicz and J. Z. Zhu, "The superconvergent patch recovery (SPR) and adaptive finite element refinement," *Comput. Methods Appl. Mech. Eng.*, vol. 101, no. 1-3, pp. 207-224, 1992.
- [99] J. Belinha, "Manual for FEMAS - M-15.1 - Construction and elasto-static analysis of a 2D Mode," pp. 1-83, 2016.
- [100] P. Kang, M. Liao, M. R. Wester, J. S. Leeder, and R. E. Pearce, "NIH Public Access," *Ratio*, vol. 36, no. 3, pp. 490-499, 2010.
- [101] M. Ghazizadeh and R. Ghazizadeh, "Application of a novel technique for observing internal ultrastructure of human chromosomes with known karyotype," pp. 3-10, 2010.
- [102] C. Harrison, T. Allen, M. Britch, and R. Harris, "High-resolution scanning electron microscopy of human metaphase chromosomes," *J. Cell Sci.*, vol. 56, no. 1, pp. 409-422, 1982.
- [103] W. A. Wall, L. Wiechert, A. Comerford, and S. Rausch, "Towards a comprehensive computational model for the respiratory system," *Int. j. numer. method. biomed. eng.*, vol. 26, no. 1, pp. 807-827, 2010.
- [104] U. Tremel, F. Deister, O. Hassan, and N. P. Weatherill, "Automatic unstructured surface mesh generation for complex configurations," *Int. J. Numer. Methods Fluids*, vol. 45, no. 4, pp. 341-364, 2004.
- [105] D. Wang, O. Hassan, K. Morgan, and N. Weatherill, "EQSM: An efficient high quality surface grid generation method based on remeshing," *Comput. Methods Appl. Mech. Eng.*, vol. 195, no. 41-43, pp. 5621-5633, 2006.

